REVISION 1

Geochemistry, petrologic evolution, and ore deposits of the Miocene Bodie Hills Volcanic Field, California and Nevada

By Edward A. du Bray[1], David A. John[2], Brian L. Cousens[3], Leslie A. Hayden[4], and Peter G. Vikre[5]

[1] U.S. Geological Survey, MS 973; Box 25046, DFC; Lakewood, CO 80225
[2] U.S. Geological Survey, MS 901; 345 Middlefield Rd., Menlo Park, CA 94025
[3] Department of Earth Sciences; Carleton University; 1125 Colonel By Drive; Ottawa, ON. K1S5B6 Canada
[4] U.S. Geological Survey, MS 910; 345 Middlefield Rd., Menlo Park, CA 94025
[5] U.S. Geological Survey, Reno Office; Mackay School of Earth Sciences and Engineering; University of Nevada, Reno; Reno, NV 89557-0047

Abstract

The southern segment of the ancestral Cascades magmatic arc includes numerous volcanic fields; among these, the Bodie Hills volcanic field (BHVF), astride the California-Nevada border north of Mono Lake, is one of the largest (>700 km^2) and most well studied. Episodic magmatism in the BHVF spanned about 9 million years between about 15 and 6 Ma; magmatic output was greatest between ca. 15.0 to 12.6 Ma and ca. 9.9 to 8.0 Ma.

About two dozen contiguous and coalescing eruptive centers above middle- to shallow-crustal-level reservoirs generated several trachyandesite stratovolcanoes and numerous silicic trachyandesite to rhyolite flow dome complexes whose compositional variations are consistent with fractionation of observed phenocryst phases. BHVF rocks have high-potassium calc-alkaline compositions consistent with generation of subduction-related continental margin arc magmas beneath thick continental crust. Radiogenic isotope ratios in BHVF rocks vary considerably but suggest somewhat enriched, crustal sources; isotopic ratios for some of the more primitive units are consistent with more depleted, mantle sources. Neither age nor whole-rock compositions of BHVF rocks are well correlated with isotopic variations. Textures and compositions of phenocrysts in BHVF rocks are in accord with the associated magma reservoirs evolving via open-system behavior. Reservoir recharge and subsequent incomplete homogenization are evidenced by the broad compositional diversity characteristic of many BHVF eruptive units. Significant compositional diversity among the products of coeval eruptive centers further suggests that centers responsible for BHVF magmatism were underlain by small, discrete, compositionally distinct, and closely spaced reservoirs.

Volcanic rocks of the BHVF host quartz-adularia and quartz-alunite epithermal gold-silver deposits, from which about 3.4 Moz. of gold and 28 Moz. of silver have been produced. The volcanic rocks and contained deposits are broadly coeval, which suggests that the associated magmas are the sources of heat, fluids, and metals involved in deposit genesis. Characteristics of the quartz-adularia deposits are consistent with derivation from near-neutral pH fluids at ≤250°C, whereas those of the quartz-alunite systems require more acidic, oxidized, and sulfur-rich fluids at temperatures <250°C. Economically viable precious metal accumulations are in fault-hosted vein deposits in the Bodie and Aurora districts. Circulation of hydrothermal fluids through permeable pyroclastic deposits but lacking prominent structural conduits resulted in large areas of altered but unmineralized rock.

Keywords: arc magmatism, geochemistry, petrogenesis, mineral deposits, tectonic setting

Introduction

The middle to late Miocene Bodie Hills volcanic field (BHVF) in the Bodie Hills north of Mono Lake, in western Nevada and eastern California, represents a large (>700 km^2), long-lived (≈9 m.y.), but episodic field in the southern segment of the ancestral Cascades arc (John et al., 2012; du Bray et al., 2014) (Fig. 1). In the BHVF, erupted volumes, duration of magmatism, compositional diversity, and degree of eruptive center preservation are unusual relative to other southern segment, ancestral Cascades arc volcanic fields (John et al., 2012; du Bray et al., 2014). The geochemical evolution of the BHVF is documented by compositional data for 21 major and 10 minor (eruptive units with map areas of less than 2 km^2; John et al., 2015) centers. The large dataset synthesized as part of this study provides a unique opportunity to evaluate the processes that contributed to the evolution of subduction-related magmatism and related precious metal mineral deposit formation in the southern segment of the ancestral Cascades arc. The goal of this paper is to assess overall compositional-temporal variation within the BHVF, compositional evolution within its individual eruptive centers, and relations between magmatism and mineralizing processes.

FIGURE 1 NEAR HERE

Previous studies

Geologic studies of the Bodie Hills have focused on mineral deposits in the Bodie, Aurora, and Masonic mining districts (e.g., Hill, 1915; Chesterman et al., 1986; Herrera et al., 1991, 1993; Osborne, 1991; Silberman and Chesterman, 1991; Breit, 2000; Vikre and Henry, 2011; Vikre et al., 2015), volcanic stratigraphy in the Bodie 15′ quadrangle (Chesterman, 1968; Chesterman and Gray, 1975), late Cenozoic development of the Mono Basin (Gilbert et al., 1968; Al-Rawi, 1969), geology of the Bodie Hills volcanic field (John et al., 2012), and evolution of the post-subduction Pliocene-Pleistocene Aurora volcanic field (Lange et al., 1993; Lange and Carmichael, 1996). John et al. (2015) compiled a new geologic map of the Bodie Hills from existing data and refined geologic relations based on extensive new fieldwork and geochronology. Geophysical studies of the BHVF, summarized by John et al. (2012) pertain to region-scale Basin and Range geology and tectonism in the area surrounding the Bodie Hills (e.g., Eaton et al., 1978; Blakely and Jachens, 1991; Saltus and Jachens, 1995) and expressions of gold-silver deposits and large areas of altered rock (e.g., Kleinhampl et al., 1975; Smailbegovic, 2002; Rockwell, 2010).

Geology of the Bodie Hills volcanic field

The wealth of new geochemical, geochronologic, and petrographic data synthesized herein, in concert with geologic map relations summarized by John et al. (2015), distinguish the BHVF as one of the few, well documented large volcanic fields within the ancestral Cascades arc. The Bodie Hills straddle a roughly 40 by 30 km area along the California-Nevada border and rise to an elevation of 3112 m at Potato Peak, about 1100 to 1400 m above Bridgeport and Fletcher Valleys, Mono Valley, and the East Walker River (Fig. 2). The central Sierra Nevada rises nearly 2000 m above Bridgeport Valley and Mono Valley about 8 km west of the Bodie Hills. The volcanic field includes the products of overlapping and coalesced eruptive centers in which stratigraphic relations are poorly developed, requiring geochronologic data to establish relative ages. The BHVF includes at least 31 volcanic map units associated with 21 significant volcanic eruptive centers and several smaller centers (Fig. 2). The eruptive centers include several trachyandesite stratovolcanoes that were emplaced along the margins of the volcanic field and numerous silicic trachyandesite to rhyolite flow dome complexes that were generally localized more centrally (Supplemental Fig. 1). Volcanism in the BHVF was episodic, with two peak periods of eruptive activity, including an early period between ca. 15.0 to 12.6 Ma that formed several large stratovolcanoes and a later period from ca. 9.9 to 8.0 Ma dominated by emplacement of large silicic trachyandesite-dacite lava domes but also including formation of the trachyandesite stratovolcano centered on Mount Biedeman (Fig. 2). Magmatism in the BHVF concluded with formation of dispersed, structurally controlled, small-volume silicic lava domes at about 6 Ma.

FIGURE 2 NEAR HERE

Miocene igneous rocks of the BHVF were erupted onto pre-Tertiary basement, discontinuously exposed throughout the Bodie Hills (John et al., 2015). Pre-Tertiary rocks consist of (1) lower Paleozoic hornfelsed argillite, sandstone, chert, and pebble conglomerate; (2) Triassic(?) metamorphosed sandstone, siltstone, chert, tuff, and pillow basalt; (3) Mesozoic (Jurassic?) meta-andesite, metatuff, and metavolcaniclastic rocks; and (4) Late Cretaceous (98–83 Ma; John et al., 2015) granitic rocks that are part of the Sierra Nevada batholith (Chesterman and Gray, 1975; Stewart et al., 1982; Robinson and Kistler, 1986). The Paleozoic and Mesozoic metasedimentary rocks crop out in the southwestern and northern parts of the Bodie Hills, Mesozoic metavolcanic rocks are exposed in the northern and eastern parts, and the Late Cretaceous granitic rocks crop out around the margins of the area.

The Bodie Hills are in a complex tectonic setting near the west edge of the Walker Lane and the Basin and Range physiographic province and at the northwest limit of the Mina deflection (Fig. 1; Stewart, 1988; Faulds and Henry, 2008; Busby, 2013); associated structures related to these tectonic features might have localized BHVF magmatism. The Walker Lane fault system is a broad, northwest-striking, dextral high-strain zone that accommodates about 20 percent of the right-lateral motion between the Pacific and North American plates (Oldow, 2003; Faulds and Henry, 2008; John et al., 2012; Busby, 2013). The Mina deflection (Fig. 1) is a 60-km right step in the Walker Lane (Stewart, 1988; Oldow, 1992; Faulds and Henry, 2008), in which slip is partitioned across an approximately 80-km-wide, complex array of northwest-striking right-lateral faults, northeast-striking normal faults, and east- to east-northeast-striking left-lateral faults (Oldow, 1992; Wesnousky, 2005). The Bodie Hills are at the northwest corner of the Mina deflection (Fig. 1), where east-striking left-lateral faults transition to northeast-striking normal faults. Slip transfer in the Mina deflection apparently began after approximately 11 Ma (Faulds and Henry, 2008), and may reflect the east-northeast-trending Neoproterozoic continental margin generally considered to correspond to the initial $^{87}Sr/^{86}Sr$ (Sr_i) = 0.706 and/or $^{208}Pb/^{204}Pb$ =38.8 isopleths in Mesozoic granitic plutons (Fig. 1; Kistler and Peterman, 1978; Stewart, 1988; Tosdal et al., 2000). Formation of the BHVF spanned the transition between subduction of the Farallon plate beneath the western margin of North America and the establishment of a transform plate margin at about 9 Ma, when the Mendocino triple junction passed north of the BHVF (Atwater and Stock, 1998). BHVF eruptive centers do not include sheeted-dike systems, which suggest that these centers evolved in a tectonic setting that was not dominated by strong horizontal strain gradients (John et al., 2012, 2015).

Compositions of Bodie Hills volcanic rocks vary from ~50 to 78 wt% SiO_2, although rocks with <55 wt% SiO_2 are rare. Rock compositions form a high-potassium calc-alkaline series with many geochemical features consistent with subduction-related continental margin arc magmatism. However, significant BHVF volcanism persisted to 8 Ma, following the cessation of subduction-related inputs, without magma compositions or eruption styles changing from those characteristic of arc magmatism. Although the oldest eruptive centers have the most mafic compositions, erupted rock compositions oscillated between mafic and intermediate to felsic compositions through time. Most BHVF rocks are porphyritic, commonly containing 15–35 volume percent phenocrysts of plagioclase, pyroxene, and hornblende±biotite.

Regional framework and the underpinnings of the Bodie Hills volcanic field as indicated by geophysical data

The most comprehensive gravity and magnetic investigations of the BHVF geology are described by John et al. (2012). Gravity and aeromagnetic data for the Bodie Hills suggest that the BHVF is within a rhomboid-shaped negative gravity anomaly (Fig. 5 in John et al., 2012). These data are consistent with the BHVF being underlain by relatively low-density crust, interpreted as either Mesozoic granitic rocks related to the Sierra Nevada batholith or Miocene intrusive rocks related to the BHVF. Magnetic anomalies associated with the BHVF have high amplitudes and short wavelengths typical of unaltered volcanic rocks (Supplemental Fig. 2); numerous positive and negative magnetic anomalies are clearly related to individual volcanic edifices, notably Aurora Crater, Aurora Peak, West Brawley Peak, and Potato Peak.

The broad gravity low coincident with BHVF rocks is bounded on the north, south, and east by northeast- and west-northwest–striking, steep gravity gradients (Fig. 5 in John et al., 2012). In addition, the bulk of BHVF magmatism was centrally localized between laterally restricted exposures of pre-Tertiary rocks, also spatially coincident with the broad gravity low (Supplemental Fig. 2). Local gravity highs generally coincide with exposed pre-Tertiary rocks. Large positive gravity anomalies north, south, and east of the BHVF seem to reflect pre-Tertiary basement at or near the present-day topographic surface; the bounding linear gradients probably define contacts between pre-Tertiary basement lithologies beneath the BHVF, especially between relatively low-density igneous rocks and higher-density metamorphic rocks (John et al., 2012). Accordingly, the broad gravity low is a consequence of either low-density BHVF rocks and/or low-density silicic intrusive rocks. The latter interpretation seems more plausible because topographic and gravity anomalies are not spatially correlated. Specifically, the gravity lows are not co-spatial with the high-relief BHVF edifices (Fig. 5 in John et al., 2012). The inferred intrusive rocks are completely concealed beneath the BHVF but constitute either an eastward extension of the Mesozoic Sierra Nevada batholith or late Cenozoic felsic intrusions related to development of the BHVF. Although the two ages of intrusive rock cannot be distinguished from gravity anomalies alone, the spatial association of the broad gravity low with the BHVF and the overall concentration of silicic rocks toward the center of the BHVF (Supplemental Fig. 1) suggest that these anomalies reflect intrusions associated with BHVF magmatism.

Several positive aeromagnetic anomalies suggest the presence of intrusions with elevated magnetic susceptibilities ~2 km below the present topographic surface (John et al., 2012). Aeromagnetic data filtered to emphasize associated source intrusions at these depths include positive aeromagnetic anomalies coincident with volcanic edifices at Potato Peak, Bodie Mountain, and West Brawley Peak. The inferred late Cenozoic felsic intrusions, emplaced either before or during BHVF magmatism, may represent solidified magma reservoirs beneath the shallow intrusions coincident with the positive magnetic anomalies, which in turn are directly associated with some BHVF eruptive centers. Roughly circular aeromagnetic anomalies indicate that magma emplaced within individual eruptive centers was localized in a relatively uniform prevailing horizontal stress field, not in a differential horizontal stress field that would have favored development of elongate magma reservoirs, eruptive centers, and accompanying geophysical signatures (John et al., 2102).

Analytical methods

New chemical and petrographic data were obtained for volcanic rock constituents of the Bodie Hills volcanic field. Representative samples of all units were collected throughout their respective geographic distributions. Whole-rock chemical analyses for 395 unaltered samples were performed by SGS Minerals (under contract to the U.S. Geological Survey). Major oxide abundances were determined by wavelength dispersive X-ray fluorescence spectrometry and were recalculated to 100%, volatile free. Trace element abundances were determined by a combination of inductively coupled plasma–atomic emission and inductively coupled plasma–mass spectrometry. (For analytical methods, see Taggart, 2002; also see http://minerals.cr.usgs.gov/projects/analytical_chem/references.html). Previously published analyses (principally major oxides) of about 48 samples (du Bray et al., 2009) are included in findings reported herein. Whole-rock geochemical data synthesized for this investigation constitute Supplemental Data Table 1[1]. Standard petrographic microscope techniques were employed to identify phenocryst minerals and their relative abundances, as well as other diagnostic petrographic criteria in 523 samples of BHVF rocks; results tabulated in du Bray et al. (2013).

A subset of 45 BHVF samples was selected for Pb, Sr, and Nd isotopic analysis utilizing the Thermo-Finnigan TRITON T1 thermal ionization mass spectrometer at Carleton University (techniques of Cousens, 1996). All Pb mass spectrometer analyses are corrected for fractionation using NIST SRM981; average ratios measured for this standard are $^{206}Pb/^{204}Pb = 16.889 \pm 0.007$, $^{207}Pb/^{204}Pb = 15.426 \pm 0.009$, and $^{208}Pb/^{204}Pb = 36.494 \pm 0.031$, based on 35 runs, May 2008–May 2011. The fractionation correction is +0.13%/amu (based on the values of Todt et al., 1996). Sr isotope ratios are normalized to $^{86}Sr/^{88}Sr=0.11940$. Two Sr standards are run at Carleton University. Measured values for NIST SRM987 are $^{87}Sr/^{86}Sr = 0.710239 \pm 14$, n=20, May 2008–May 2011) and those for Eimer and Amend (E&A) $SrCO_3$ are $^{87}Sr/^{86}Sr = 0.708012 \pm 15$, n=10, September 2007–May 2011. Nd isotope ratios are normalized to $^{146}Nd/^{144}Nd=0.72190$. The average of measured values for a Nd metal standard are $^{143}Nd/^{144}Nd = 0.511823 \pm 12$, corresponding to a La Jolla reference standard value of 0.511852 based on comparative runs

[1] Deposit item AM-XX-YYYYY, Supplemental Data Tables 1–2 and Figures 1-49. Deposit items are stored on the MSA web site and available via the *American Mineralogist* Table of Contents. Find the article in the table of contents at GSW (ammin.geoscienceworld. org) or MSA (www.minsocam.org), and then click on the deposit link.

(May 2008–2011). All quoted uncertainties are 2-sigma standard deviations of the mean. All analyses have been corrected for radiogenic ingrowth using measured parent and daughter element concentrations and $^{40}Ar/^{39}Ar$ age determinations.

Compositions of minerals in representative BHVF samples (Supplemental Data Table 2) were determined using a JEOL 8900 electron microprobe with five wavelength dispersive crystal spectrometers at the U.S. Geological Survey in Menlo Park, CA. Plagioclase, alkali feldspar, amphibole, biotite, ortho- and clinopyroxene, olivine, apatite and titanite in thin-sections of the trachyandesites of Willow Springs, Mount Biedeman, West Brawley Peak, and Masonic and the rhyolite of Bodie Hills were the primary focus of these analyses. Compositions of magnetite and ilmenite were also determined in samples of the trachyandesites of West Brawley Peak, Del Monte, Mount Biedeman, Masonic, Aurora Canyon, the dacite of Silver Hill, and the rhyolite of Bodie Hills. A 1-5 μm spot size, with 15 kV accelerating voltage and 10-30 nA beam current were used to make these analyses. To supplement transmitted light microscopy, analyzed thin sections were also examined using a scanning electron microscope and backscatter electron imaging to observe zoning and textural features.

Volcanologic characteristics of Bodie Hills volcanic field rocks

Volcanic rocks in the Bodie Hills (Table 1) depict a broad array of effusive and explosive eruptive styles as summarized by John et al. (2012, 2015). Each of the BHVF eruptive centers includes variable combinations of lava flows, block-and-ash-flow deposits, debris-flow deposits, and associated shallow intrusive bodies. Exposed intrusive rocks, however, are volumetrically minor and are restricted to domes, small plugs, and exceptionally rare dikes. Several eruptive centers are composite volcanoes (stratovolcanoes), whereas lava domes dominate others. Debris-flow deposits and less voluminous block-and-ash-flow deposits are nearly ubiquitous constituents of individual eruptive centers; however, their abundances among the centers are highly variable. Physical volcanologic characteristics of volcanic rocks exposed in Bodie Hills are consistent with these rocks being products of continental margin, subduction-related arc magmatism.

TABLE 1 NEAR HERE

Time-volume characteristic of Bodie Hills volcanic field eruptive centers

Calculating volumes erupted from each BHVF eruptive center was not possible because accurate thicknesses of individual units, most separated by buttress unconformities, could not be reliably determined. Consequently, we have used area covered by each map unit, as determined from the Bodie Hills geologic map (John et al., 2015), as a proxy for erupted-volume variation through time. Map-unit areas versus age relations (Fig. 3) define four magmatic episodes in the BHVF; these are separated by periods of minimal to no magmatism. Although multiple age determinations (Fleck et al., 2015) available for some BHVF units indicate 0.1 to 1 m.y. age variations among the products of some individual volcanic centers, we calculated an average age, modified in a few circumstances to account for known relative age relations, to define a single, preferred age for each of the BHVF units (Table 1). The first magmatic episode is one of two approximately 1-m.y.-long intervals that each account for more than one fourth of BHVF eruptive volume. This episode (1), from about 15.0 to 13.9 Ma, is dominated by magma erupted from the Masonic stratovolcano but also includes the trachyandesite of Mud Springs Canyon. Slightly younger magmatism included in this episode includes small volume trachydacite of East Canyon lava domes and very small volume trachyandesite of Sinnamon Cut intrusions. The next major episode (2), between 13.5 and 12.5 Ma, is dominated by the trachyandesite of Aurora stratovolcano and trachydacite of Rough Creek lava domes but also includes relatively small volume magmatic activity associated with three less voluminous eruptive centers. An essentially amagmatic hiatus of about 1 m.y. between about 12.9 and 11.7 Ma follows episode 2, although a very small volume of magma was emplaced as hornblende trachyandesite plugs during this interval. The next episode (3) represents essentially continuous eruptive activity between about 11.7 and 8.0 Ma but includes a volumetric lull from about 10.5to 9.5 Ma. This third episode constitutes the longest and most compositionally diverse period of volcanism associated with the BHVF and involves numerous separate eruptive centers located throughout the field. The episode culminated in the second of two high-volume output intervals. This approximately 1-m.y.-long interval includes three major lava dome and flow centers: the dacite of Silver Hill (9.1 Ma), trachydacite of Potato Peak (8.9 Ma), and trachyandesite of Willow Springs (8.2 Ma). After a hiatus of about 2.2 m.y., the final episode (4) of magmatism in the BHVF is expressed by eruption of a series of relatively small-volume, viscous lava flows and intrusions represented by the rhyolite of Big Alkali (5.8 Ma).

FIGURE 3 NEAR HERE

Petrographic characteristics

Most analyzed BHVF rocks are relatively fresh and unaffected by hydrothermal alteration; however, many samples are weakly weathered. The effects of shallow magmatic degassing are largely limited to variable alteration of hornblende and biotite. BHVF rocks proximal to mineralized systems were altered by localized hydrothermal fluid flow to mineral assemblages (described in the "Mining districts and alteration zones in the Bodie Hills volcanic field" section of this paper) characteristic of quartz-adularia and quartz-alunite epithermal systems.

Essentially all BHVF rocks are porphyritic (Fig. 4). Most phenocrysts are fine (<1 mm) to medium grained (1-5 mm); however, the trachyandesite of Willow Springs, trachydacite of Cinnabar Canyon, trachyandesite of Mud Springs Canyon, trachydacite of Bridgeport Canyon, trachyandesite of West Brawley Peak, and andesite of Lakeview Spring contain distinct, coarse (≥5 mm) plagioclase phenocrysts and the trachyandesite of Aurora contains unusually coarse (1-2 cm) hornblende phenocrysts in many places. Average phenocryst abundances are summarized in Table 2; John et al. (2015) further characterize phenocryst characteristics. Euhedral, albite-twinned plagioclase laths are a nearly ubiquitous component of BHVF rocks. Almost all plagioclase phenocrysts are oscillatory zoned, and some, especially those in intermediate-composition lava flows, are variably sieve textured. Many units contain multiple plagioclase populations defined by size and/or distinctive reaction rims, zones that contain mineral and/or glass inclusions, and resorption textures (Fig. 4). Brown to green pleochroic hornblende forms euhedral to subhedral acicular crystals that have distinctive, variably developed amorphous, black opacite reaction rims (Rutherford and Hill, 1993) that likely reflect shallow-level magmatic degassing. Clinopyroxene, common in many BHVF rocks, forms pale tan to pale green subhedral to euhedral crystals. Less common orthopyroxene is colorless to rosy tan and forms euhedral to subhedral crystals. Biotite is subhedral, tan to deep red brown and like hornblende, is completely altered to dark brown to black, amorphous material in samples affected by shallow degassing. Relatively uncommon olivine forms variably altered subhedral phenocrysts in some of the mafic- to intermediate-composition rocks. Quartz is absent in all but the most silicic units; where present, it forms variably resorbed and embayed, rounded anhedral to subhedral phenocrysts. Alkali feldspar is less common than quartz but forms variably and weakly perthitic Carlsbad-twinned, euhedral to subhedral phenocrysts in several of the rhyolite to silicic trachydacite units.

FIGURE 4 NEAR HERE

TABLE 2 NEAR HERE

Small amounts of Fe-Ti oxide minerals, including magnetite and less abundant ilmenite, are ubiquitous. They form subhedral to rounded or resorbed crystals as (1) isolated phenocrysts, (2) small inclusions in mafic silicate and plagioclase phenocrysts, (3) constituents in mafic silicate mineral clots, and (4) finely disseminated groundmass grains. In most BHVF rocks, Fe-Ti oxide crystals are variably exsolved or altered. Many titanomagnetite crystals are partly exsolved to hematite lamellae with a skeletal martite texture. In other samples, titanomagnetite includes ilmenite exsolution lamellae and/or ilmenite rims. Magnetite in more strongly altered samples is irregularly oxidized to hematite along crystal margins and fractures. Most ilmenite crystals are relatively homogeneous.

The groundmass of most BHVF rocks contains variable microphenocryst (typically 0.05 to 0.2 mm long) assemblages, dominated by plagioclase (Fig. 4), but also includes combinations of Fe-Ti oxide minerals, clinopyroxene and, less commonly, hornblende and/or biotite. Metastable volcanic glass, variably hydrated or devitrified (crystallized), constitutes another major groundmass component. Accessory mineral suites include nearly ubiquitous apatite, and in several of the rhyolite units, variable combinations of titanite, zircon, and allanite. Exotic lithic fragments or inclusions are rare but glomerocrysts as much as several millimeters in diameter are present in samples of many BHVF units. Notable xenocrysts, especially inclusion-rich plagioclase in the trachydacite of Rough Creek, are important components of some units.

Whole-rock geochemistry

Major oxide data

Major oxide compositions of BHVF rocks vary from basalt to rhyolite (Table 3, Fig. 5) and compositions of individual units vary considerably. The BHVF rocks have silica contents that range, essentially continuously, from about 50 to 77.5 wt%; rocks with less than about 55 wt% SiO_2 are rare and those with 67 to 71 wt% SiO_2 are somewhat underrepresented. Compositions of the BHVF rocks are transitionally alkaline (principally due to elevated K_2O contents); most compositions cluster between the alkaline-subalkaline nomenclature break (Fig. 5) and the alkaline-subalkaline dividing line of Irvine and Baragar (1971). Relative to standard metrics (in cited sources), the vast majority of the BHVF rocks are metaluminous (Shand, 1951), although several of the rhyolites are weakly peraluminous; calc-alkalic to alkali-calcic (Frost et al., 2001); magnesian (calc-alkaline) to weakly ferroan (tholeiitic) (Frost et al., 2001); and follow the calc-alkaline (Irvine and Baragar, 1971) differentiation trend (Supplemental Figs. 3-6). Concentrations of TiO_2 and P_2O_5 vary considerably at lower SiO_2 abundances but scatter less and decrease to lower values at higher SiO_2 contents. Concentrations of FeO* (total iron expressed as ferrous oxide) and CaO (Fig. 6), as well as MnO (Supplemental Data Table 1), decrease linearly with increasing SiO_2. Like TiO_2 and P_2O_5 abundances, Al_2O_3 abundances vary considerably at lower SiO_2 abundances; Al_2O_3 abundances vary unsystematically in samples with less than about 65 wt% SiO_2, and then decrease significantly and consistently, forming a concave downward data array. Abundances of MgO decrease in a systematic though curvilinear fashion with increasing SiO_2 to produce a slightly concave up data array.

TABLE 3 NEAR HERE

FIGURE 5 NEAR HERE

FIGURE 6 NEAR HERE

Compared to the other major oxides, Na_2O and K_2O abundances in BHVF rocks exhibit much greater relative variation (Fig. 6). At any silica content, Na_2O and K_2O abundances vary by as much as 2 wt%. Na_2O abundances vary widely but are generally lower among samples with less than 70 wt% SiO_2. Abundances of K_2O increase broadly with increasing SiO_2 content, forming a data array coincident with high-K (Gill, 1981) to weakly shoshonitic compositions. As noted above, most BHVF rocks are not hydrothermally altered; consequently, alteration is not responsible for the broad alkali abundance variations characteristic of BHVF rocks; instead, these variations largely record primary magmatic processes.

Compositional variation among rocks of the BHVF is not systematic with respect to time, although most of the eruptive centers active between 15 and 11.7 Ma produced magmas with average SiO_2 contents less than about 62 wt%, whereas most of the younger centers erupted magma having greater than 62 wt% SiO_2 (Fig. 7). Although SiO_2 contents of most BHVF rocks erupted before 11.7 Ma vary within a relatively narrow range, those erupted thereafter have highly variable SiO_2 contents. In particular, among rocks erupted after 11.7 Ma, average SiO_2 contents differ by about 27 wt% among magmas erupted within a span of as little as 0.5 m.y. (Fig. 7). Specifically, magmas erupted between about 11.7 and 9.3 Ma exhibit particularly nonsystematic SiO_2 abundance fluctuations across very brief time intervals. The lack of systematic compositional variation of BHVF rocks with respect to time is mimicked by data for most of the major oxides. Specifically, in most BHVF rocks abundances of TiO_2, Al_2O_3, FeO*, MnO, MgO, CaO, Na_2O, K_2O, and P_2O_5 do not vary systematically with respect to time and, with exceptions described below, their abundances in individual units are not readily distinguishable from those of many other BHVF units (Fig. 8). The ranges of the major oxide abundances in specific units, especially among the voluminous products erupted from the large composite volcanic centers (including the trachyandesites of Masonic, Aurora, Del Monte, and Mount Biedeman, and the basaltic trachyandesite of Rancheria) and the trachyandesite of Aurora Canyon are remarkably diverse. In fact, compositional diversity within many of these units approaches that portrayed by the entire BHVF.

FIGURE 7 NEAR HERE

FIGURE 8 NEAR HERE

Major oxide abundances of several BHVF units, especially the basaltic trachyandesite of Rancheria, the rhyolite of Big Alkali, and the pyroxene rhyolite and high silica rhyolites of the BHVF (including the rhyolites of the Bodie Hills, Bald Peak, Bodie Creek, Rock Springs Canyon, Aurora Creek, and Del Monte Canyon) do have some distinctive features. Abundances of FeO*, MgO, CaO, and P_2O_5 in the basaltic trachyandesite of Rancheria are distinctly higher than those characteristic of most BHVF units. In contrast, the rhyolite of Big Alkali contains abundances of TiO_2, FeO*, and CaO that are generally lower than those characteristic of all but the high silica rhyolites of the BHVF. As a group, the 11 to 9.5 Ma high silica rhyolites are compositionally distinct relative to all other BHVF units. These rocks have low TiO_2, Al_2O_3, FeO*, CaO, and P_2O_5 and, in addition to silica, high K_2O contents, all in accord with their more evolved character.

Trace element data

Rocks of the BHVF have high large-ion lithophile element (LILE) abundances and low high-field-strength element (HFSE) abundances (Supplemental Data Table 1) similar to those of other convergent-margin, broadly calc-alkaline igneous rocks, such as those in the Andean, Kamchatka, and Central American arcs (GEOROC, 2010). Abundances of Cs, Pb, Rb, Ta, Th, and U and $(La/Lu)_N$ increase (Supplemental Figs. 7-13), whereas those of Co, Cr, Ni, Sc, Sr, V, Y, Zn and Eu/Eu*and total rare earth element (REE) content decrease with increasing silica content (Supplemental Figs. 14-23). Ba abundances increase as silica increases up to about 65 wt% SiO_2 and decrease dramatically thereafter (Supplemental Fig. 24). Abundances of Zr vary widely in samples with <65 wt% SiO_2 and decrease somewhat unsystematically thereafter (Supplemental Fig. 25). Abundances of Hf, La, and Nb exhibit no systematic variation with respect to increasing silica content (Supplemental Figs. 26-28).

Trace element abundances of the BHVF rocks, like their major oxide compositions, vary nonsystematically in a temporal context. Specifically, in most BHVF rocks, abundances of Ba, Co, Cr, Cs, Hf, La, Nb, Ni, Pb, Rb, Sc, Sr, Ta, Th, U, V, Y, Zn, and Zr and total REE, Eu/Eu*, and La/Yb vary nonsystematically with respect to time and their abundances in individual units are not readily distinguishable from those of most other BHVF units (Fig. 8). However, some trace element abundances for the basaltic trachyandesite of Rancheria, the rhyolite of Big Alkali, and the pyroxene rhyolite and high silica rhyolites of the BHVF are each distinctive. The basaltic trachyandesite of Rancheria is distinguished by higher Co, Cr, and Ni abundances than all other BHVF units. The rhyolite of Big Alkali has lower Co, La, Nb, V, and Y and total REE abundances and higher Pb abundances than most other BHVF units. As a group, the BHVF high silica rhyolites contain elevated Cs, Rb, and Th abundances and distinctly low abundances of Ba, Co, Sr, V, and Zn, and have low Eu/Eu*.

Average chondrite-normalized REE patterns for rock units of the BHVF form two distinct groups (Fig. 9): one corresponds to units with >69 wt% SiO_2 and the other to units with <69 wt% SiO_2. All of these REE patterns are similar to those characteristic of intermediate composition, calc-alkaline continental margin magmatic arc igneous rocks (e.g., Gill, 1981; Cameron and Cameron, 1985; Wark, 1991; Feeley and Davidson, 1994). Within each of the two groups, REE patterns for the set of samples representative of any particular rock unit broadly overlap sets of patterns for each of the other rock units; consequently, patterns representative of many individual BHVF rock units are essentially indistinguishable. However, average chondrite normalized patterns for rock units that constitute each of the two BHVF compositional groups span relatively restricted REE abundance ranges and have similar REE characteristics (essentially parallel patterns and similar Eu/Eu* and $(La/Yb)_N$). These similarities are noteworthy given the large number of discrete eruptive centers, their considerable age range (ca. 10 m.y.), and especially for the group of units with <69 wt% SiO_2, their diverse major oxide compositions. The felsic group includes all of the BHVF rhyolites (72.3 to 76.8 wt% SiO_2)

except the pyroxene rhyolite (average, 70.4 wt% SiO_2); the larger (intermediate) group includes all remaining BHVF units. Average chondrite-normalized REE patterns for all of the BHVF rocks are negatively sloping ($(La/Yb)_N$ >1) and have minor to moderate negative Eu/Eu* anomalies, more steeply sloped light REE (LREE) segments than heavy REE (HREE) segments, and variably U-shaped middle REE (MREE) to HREE segments (Fig. 9). Although the felsic units have average La abundances similar to those of the intermediate BHVF rocks, their LREE segments are more steeply negatively sloped, negative Eu/Eu* anomalies better developed, and although the MREE to HREE segments of their chondrite-normalized REE patterns are parallel to those of the intermediate BHVF rocks, their MREE and HREE abundances are uniformly considerably lower than those of the intermediate rocks (Fig. 9).

FIGURE 9 NEAR HERE

BHVF REE abundance variations are nonsystematic with respect to extent of magma evolution (SiO_2 content) or age (Table 4), which reflects nonsystematic petrogenetic evolution of the entire BHVF in time and space. Both total REE and La abundances serve as synoptic representations of rock REE abundances among units of the BHVF. Neither total REE nor La abundance unit averages demonstrate any systematic variation with respect to age or SiO_2 content, although most BHVF rhyolite units contain significantly lower total REE contents than the intermediate rocks (Supplemental Figs. 23, 27, 29-30). Average Eu/Eu* varies nonsystematically among all intermediate composition rocks of the BHVF but, predictably, decreases with increasing SiO_2 among the more evolved, silica-rich units (Supplemental Fig. 31), because increasingly silica-rich magmas fractionate feldspar, especially plagioclase, the principal residence of Eu. Similarly, Eu/Eu* varies nonsystematically with respect to age among BHVF rocks of all compositions, although Eu/Eu* is universally lower among the high silica rhyolite units erupted between about 11 and 9.5 Ma (Supplemental Fig. 32). Average $(La/Yb)_N$ for rocks of the BHVF define two populations with respect to SiO_2 content (Supplemental Fig. 33). Most units with less than 61.8 wt% SiO_2 have $(La/Yb)_N$ between about 11 and 14, whereas units with greater than 61.8 wt% SiO_2 have $(La/Yb)_N$ between about 16.5 and 21. Average $(La/Yb)_N$ increases with decreasing age, which principally reflects a small, progressive decrease of Yb abundances from the oldest to youngest units of the BHVF (Supplemental Fig. 34). Finally, subtly U-shaped MREE segments typical of BHVF rocks are best characterized by Ho/Ho* (calculated in a fashion similar to Eu/Eu*, but using Gd and Yb as calculation anchors). Among rocks of the BHVF, average Ho/Ho* broadly decreases with increasing SiO_2 content (Supplemental Fig. 35) and with decreasing unit age (Supplemental Fig. 36) though average values for the trachyandesites of Mt. Biedeman and Mud Springs Canyon, and the hornblende trachyandesite plugs disrupt these trends. In addition, the three BHVF units with anomalously low Ho/Ho* with respect to their age (trachydacite of East Canyon, 0.650; trachyandesite of Mud Springs Canyon, 0.60; and hornblende trachyandesite intrusions, 0.56) and the trachyandesite of Mount Biedeman all contain relatively abundant hornblende.

TABLE 4 NEAR HERE

The extent of within-unit REE abundance variation (chondrite-normalized pattern dispersion) is conveyed by standard deviation values calculated from the REE data for each of the BHVF units. For any given BHVF unit, standard deviations calculated for each of the REE vary within relatively narrow ranges, which suggest that the standard deviation for any particular REE (such as La, which is abundant and easily determined with high precision) depicts REE abundance dispersion for each eruptive unit. The standard deviation of La abundance calculated for each unit was divided by its associated average La abundance to yield a consistent, normalized REE dispersion metric (La STD/AVE) for each BHVF unit (Table 4). Calculated REE dispersion values (which are independent of the numbers of samples available for each of the units) exhibit no systematic variation with respect to either SiO_2 content or age (Supplemental Figs. 37-38).

Most of the BHVF rock units with the lowest REE dispersion values (<0.1) represent minor erupted volumes (trachyandesite of Sinnamon Cut, 0.5 km^2; trachydacite of Bridgeport Canyon, 0.9 km^2; trachydacite of Cinnabar Canyon, 0.3 km^2; andesite of Lakeview Spring, 0.4 km^2; and the pyroxene rhyolite, 0.3 km^2) from seemingly small, well-homogenized reservoirs. Of the remaining units with low REE dispersion values, only the trachyandesites of Willow Springs (61.9 km^2) and Mud Springs Canyon (8.5 km^2) constitute significant erupted volumes. BHVF units with the highest REE dispersion values (>0.3) represent either large volume stratovolcanoes (trachyandesites of Mount Biedeman, Masonic, and West Brawley Peak and basaltic trachyandesite of Rancheria) or small-to moderate-volume rhyolitic centers (rhyolites of East Brawley Peak, Bodie Creek, Bald Peak, and Big Alkali); this group also includes the low-volume eruptive products associated with the hornblende trachyandesite, the trachyandesite of Clark Canyon, and the moderate-volume trachydacite of Rough Creek. BHVF units with

This is a preprint, the final version is subject to change, of the American Mineralogist (MSA)
Cite as Authors (Year) Title. American Mineralogist, in press.
(DOI will not work until issue is live.) DOI: http://dx.doi.org/10.2138/am-2016-5440 11/4

intermediate REE dispersion values represent eruptive centers with a wide array of compositions, ages, volumes, and eruptive styles.

The four most primitive samples of BHVF rocks, samples of the basaltic trachyandesite of Rancheria, contain 49.9–52.0 wt% SiO_2 and are those most likely to reflect BHVF parental magma compositions. These four samples contain LREE abundances that broadly overlap average LREE contents of all intermediate composition BHVF units and consequently progressively diverge from LREE abundances characteristic of felsic BHVF eruptive units. Negative Eu anomalies (Eu/Eu* = 0.84 to 0.93) in these four samples are insignificant and therefore somewhat smaller than those characteristic of the intermediate units and dramatically smaller than those typical of BHVF felsic units. Middle to heavy REE abundances of the four most primitive samples overlap those of the most HREE-enriched BHVF units and thus are somewhat greater than those of some intermediate composition units and significantly greater than those of felsic units within the BHVF.

Average primitive mantle-normalized patterns for rocks of the BHVF are similar to those characteristic of other continental margin, subduction-related magmatic arc rocks (Fig. 10). In particular, these rocks have well-developed negative Nb-Ta anomalies considered characteristic of arc magmas (Wood et al., 1979; Gill, 1981; Pearce et al., 1984). Average primitive mantle-normalized patterns for rocks of the BHVF include distinct positive Pb and variably developed negative P and Ti anomalies. Certain features of these patterns emphasize the differences between the two groups defined by relative REE abundances. Specifically, average primitive mantle-normalized patterns for the felsic rocks include minor positive Th and larger positive K and Pb anomalies and larger negative P and Ti anomalies than those characteristic of intermediate composition BHVF rocks. In addition, these patterns show that felsic rocks of the BHVF contain higher Rb and lower Ba, Sr, Zr, and Hf than their intermediate counterparts. All BHVF rocks have small positive K anomalies, which underscores the fundamentally potassic character of these rocks.

FIGURE 10 NEAR HERE

Radiogenic isotope data

Analyses of individual BHVF rock samples exhibit a wide range of radiogenic isotope ratios (Fig. 11): initial $^{87}Sr/^{86}Sr$ values (Table 5) range from 0.70399 to 0.70602 and ε_{Nd} values (Table 6) from +2.26 to -4.17. $^{206}Pb/^{204}Pb$ values (Table 7) range from 18.895 to 19.087, and

(DOI will not work until issue is live.) DOI: http://dx.doi.org/10.2138/am-2016-5440 11/4

$^{208}Pb/^{204}Pb$ values range from 37.654 to 38.933. Data for the intermediate composition rocks span almost the entire BHVF isotopic compositional range, whereas the BHVF rhyolitic rocks have the highest initial $^{87}Sr/^{86}Sr$ values, the lowest □$_{Nd}$ values, and more variable Pb isotopic compositions. Although Sr and Nd isotope ratios are negatively correlated, neither Sr nor Nd isotope ratios correlate well with Pb isotope ratios. The 12 to 11 Ma trachyandesites in the BHVF exhibit significant isotopic heterogeneity (Fig. 11).

TABLES 5, 6, AND 7 NEAR HERE

FIGURE 11 NEAR HERE

Initial $^{87}Sr/^{86}Sr$ values increase slightly from ~0.705 at 15 Ma to ~0.706 at ca. 6 Ma (Fig. 12), but □$_{Nd}$ and Pb isotope ratios show no well-defined change with time. The age progression from low to high initial Sr isotope ratios is interrupted by numerous ca. 11 Ma samples that have a large range of Sr isotopic compositions; these samples include basaltic trachyandesite, trachyandesite, trachydacite, and rhyolite. The maximum variation in Pb isotope compositions is also coincident with this time. Two of the ca. 11 Ma intermediate-composition units, the hornblende trachyandesite intrusions and the trachyandesite of West Brawley Peak, have the lowest initial $^{87}Sr/^{86}Sr$ values among all BHVF rocks.

FIGURE 12 NEAR HERE

Radiogenic isotope ratios exhibit subtle variations with increasing SiO_2 content (Fig. 13). BHVF samples with 52 to 65 wt% SiO_2 have large initial $^{87}Sr/^{86}Sr$ and initial $^{206}Pb/^{204}Pb$ ranges, whereas rocks with 65 to 77 wt% SiO_2 have more restricted isotopic composition ranges. Samples with initial $^{87}Sr/^{86}Sr$ values >0.7055 span the entire SiO_2 range of BHVF rocks. Among the analyzed samples, □Nd values versus wt% SiO_2 relations are the inverse of initial $^{87}Sr/^{86}Sr$ versus wt% SiO_2 relations.

FIGURE 13 NEAR HERE

Volcanic rocks of the BHVF have Sr (initial $^{87}Sr/^{86}Sr$ >0.7048) and Pb isotope ratios at the high end of the compositional array for volcanic rocks of the ancestral Cascades arc, southern segment, and Nd isotopic characteristics (□$_{Nd}$< 0) similar (Fig. 11) to those of ancestral Cascades arc, southern segment lavas from the Central Sierra Nevada volcanic field (Putirka et al., 2012). Ancestral Cascades arc, southern segment rocks in the Lake Tahoe to Lassen Peak area have a greater range of $\square_{Nd}$ (+4.5 to -4.5) and $^{87}Sr/^{86}Sr$ (0.7033 to 0.7061) than BHVF samples. Thus, both BHVF and nearby Central Sierra Nevada volcanic field rocks have isotopic compositions generally consistent with more enriched sources (i.e., crustal components) compared to ancestral Cascades arc, southern segment rocks from north in the Sierra Nevada, although a few BHVF and Central Sierra Nevada volcanic field rocks have isotopic compositions that require a more depleted ($\square_{Nd}$ >2), presumably mantle, source.

Mineral chemistry and implications for magmatic intensive parameters

Detailed petrographic and mineral chemistry data for the BHVC provide unique insights concerning the genesis, in a continental arc setting, of individual eruptive centers and associated mineral deposits.

Among samples whose mineral compositions were determined by electron microprobe analysis, only the rhyolite of Bodie Hills (00-BA-3 and 08-BA-50) and trachyandesite of West Brawley Peak (11-BA-13) contain alkali feldspar. These phenocrysts are composed of sanidine, with compositions that range from $An_1Ab_{26}Or_{73}$ to $An_2Ab_{35}Or_{63}$ (Supplemental Data Table 2), and have barium-enriched rims (1.7-3 wt% BaO) but are otherwise unzoned. Most plagioclase phenocrysts in volcanic rocks of the BHVF have Ca-enriched cores and exhibit limited major oxide zonation. However, plagioclase phenocrysts in the trachyandesites of West Brawley Peak (rims $An_{55}Ab_{43}Or_3$ and cores $An_{33}Ab_{60}Or_7$) and Masonic (rims $An_{55\text{-}66}Ab_{43\text{-}32}Or_2$ and cores $An_{46\text{-}57}Ab_{52\text{-}39}Or_{2\text{-}4}$) have Ca-enriched rims, whereas the composition of plagioclase in the rhyolite of Bodie Hills rhyolite (sample 00-BA-3) displays broader compositional variation, having $An_{28}Ab_{68}Or_4$ rims and $An_{47}Ab_{51}Or_2$ cores. A magma blob (203381) of trachyandesite of Mount Biedeman contained in rhyolite of Bodie Hills (John et al., 2015) contains plagioclase with three unique compositions: (1) phenocrysts are $An_{50}Ab_{48}Or_2$, whereas smaller grains are either (2) $An_{57}Ab_{41}Or_2$ with high SrO (as in rhyolite of Bodie Hills and trachyandesite of Mount Biedeman samples) or (3) $An_{82}Ab_{18}Or_0$ (bytownite). Plagioclase in the trachyandesites of West Brawley Peak and Willow Springs has distinctly elevated BaO and SrO concentrations (Supplemental Data Table 1).

Many BHVF rocks contain hornblende, though it is frequently partially to completely altered to opacite (Fig. 4d) or symplectite (Rutherford and Hill, 1993) that has pseudomorphously replaced primary phenocrysts. The composition of primary hornblende in these rocks exhibits broad compositional variation (Supplemental Data Table 2). Hornblende in the trachyandesite of Willow Springs (00-BA-1) has high-Al_2O_3 rims (12 wt%) with correspondingly elevated TiO_2 and Na_2O concentrations. Hornblende in the rhyolite of Bodie Hills (00-BA-3) and trachyandesite of Mount Biedeman (09-BA-22) has low Al_2O_3 rims (8 to 10 wt%) and high Al_2O_3 (10 to 12 wt%) cores. In the rhyolite of Bodie Hills, hornblende rims also contain lower CaO and TiO_2 but higher FeO abundances, whereas hornblende in the trachyandesite of Mount Biedeman has low FeO-high MgO rims. Very fine grained, flow-oriented hornblende in the trachyandesite of Mount Biedeman magma blob (203381) has very high Al_2O_3 (~14 wt%) similar to that characteristic of coarser hornblende phenocrysts in the blob (~13 wt%); however, the fine grained hornblende crystals are FeO enriched and CaO and MgO depleted relative to hornblende phenocryst compositions. Hornblende in the trachyandesite of Masonic is relatively unzoned relative to Al_2O_3 abundances but exhibits minor FeO and MgO compositional zonation.

Biotite phenocrysts in many BHVF rocks also exhibit partial to complete alteration or pseudomorphous replacement by amorphous material. Unaltered biotite in the trachyandesite of Masonic is distinctly TiO_2 enriched (Supplemental Data Table 2) relative to biotite in the trachyandesite of Willow Springs and rhyolite of Bodie Hills (5.0-6.1 and 4.0 to 4.8 wt%, respectively). Biotite in the rhyolite of Bodie Hills (08-BA-50) is distinctly FeO- and MnO-enriched and is further characterized by distinctive rim and core compositions; rims are TiO_2 and F enriched relative to cores. In contrast, biotite in the trachyandesite of Masonic is distinctly MgO enriched.

Pyroxene in the trachyandesites of Willow Springs, Mount Biedeman, and Masonic is primarily augite (Supplemental Data Table 2). These clinopyroxene phenocrysts are frequently zoned; both normal- and reverse-zoned crystals were observed as were crystals that preserve either oscillatory bands or a single, sharp compositional boundary. Cores of clinopyroxene in the trachyandesite of Willow Springs contain as much as ~2 wt% Cr_2O_3, but their rims are Cr_2O_3 depleted. Rims of these phenocrysts are also enriched in TiO_2, and to a lesser extent in FeO and Al_2O_3. Clinopyroxene also forms small, unzoned grains in the trachyandesite of Mount Biedeman magma blob (203381) that have high Al_2O_3 (5 wt%) and, where (09-BA-19) clinopyroxene coexists with olivine, is composed of pigeonite. Clinopyroxene in the trachyandesite of Masonic is compositionally homogeneous, having low TiO_2 and Cr_2O_3 abundances and slightly FeO-enriched and MgO-depleted cores. One trachyandesite of Mount

Biedeman sample (09-BA-06) contains compositionally distinct clinopyroxene with significantly lower CaO and higher Al_2O_3, and TiO_2- and MgO-enriched cores (Supplemental Data Table 2).

Some trachyandesite of Masonic samples (10-BA-11 and 11-BA-30) contain coexisting clinopyroxene and orthopyroxene, whereas some samples of the trachyandesite of Mount Biedeman (09-BA-22) and trachyandesite of Masonic (09-BA-13) contain only orthopyroxene. Most orthopyroxene in BHVF rocks is MgO-enriched (Mg-number 70 to 74) and contains ~1 wt% Al_2O_3; phenocryst rims are Al_2O_3-enriched. Orthopyroxene in younger trachyandesite of Masonic flows has lower Mg-number rims than orthopyroxene in its older flows.

Among various BHVF rocks, the coarsest olivine phenocrysts exhibit diffuse zoning and their compositions vary significantly (Supplemental Data Table 2). Some trachyandesite of Mount Biedeman (09-BA-19) and trachyandesite of Masonic (09-BA-6) samples contain coexisting olivine and clinopyroxene. Olivine in trachyandesite of Mount Biedeman samples coexists with pigeonite, is MnO-rich, contains ~34 wt% FeO, and is compositionally similar to olivine that coexists with clinopyroxene in the trachyandesite of Masonic (09-BA-6). Coarse olivine in the trachyandesite of Masonic has FeO-rich rims and MgO-rich cores and is compositionally similar to that in trachyandesite of Mount Biedeman. Olivine phenocrysts in the trachyandesite of Mount Biedeman magma blob (203381) are compositionally homogeneous and unzoned.

Opaque iron-titanium oxides in at least 50 samples were examined by reflected-light microscopy but not analyzed because magnetite in most is exsolved and/or altered. In addition, most analyzed magnetite-ilmenite pairs failed the Mg/Mn partitioning equilibrium test of Bacon and Hirschmann (1988) and were discarded. Some magnetite-ilmenite pairs in the remaining five samples (Supplemental Data Table 2) may preserve equilibrium compositions and were used to estimate crystallization temperature and oxygen fugacity using the Fe-Ti oxide geothermometer of Ghiorso and Evans (2008). Average calculated temperatures range from 960±30°C to 711±21°C (Table 8). Temperatures determined for two trachyandesite lava flows (Masonic and Del Monte) are both >900°C, whereas three intrusive rock samples (dacite of Silver Hill and trachyandesites of West Brawley Peak and Aurora Canyon) yielded temperatures <750°C, which likely represent subsolidus cooling temperatures. Calculated oxygen fugacities relative to the Ni-NiO buffer fall into two groups, +1.5 to +1.2 (Masonic, West Brawley Peak, and Silver Hill) and

+0.2 log units (Del Monte and Aurora Canyons), but do not correspond to intrusive versus extrusive samples (Table 8; Supplemental Data Table 2).

Apatite and titanite are the two most common accessory minerals in BHVF rocks. Apatite, nearly ubiquitous in BHVF rocks, forms crystals that range from equant to elongate and skeletal that are often zoned with respect to trace element and volatile contents. Titanite (associated with chevkenite) grains are up to a few hundred microns long and strongly sector zoned; titanite in the rhyolite of Bodie Hills (00-BA-3) contains ~1.2 wt% Al_2O_3 and ~1.7 wt% FeO (Supplemental Data Table 2).

Al-in-hornblende barometry (Holland and Blundy, 1994) applied to compositions of hornblende in rhyolite of the Bodie Hills yields a pressure estimate of 2.7 (±0.2) kbar at 725°C, which is equivalent to a reservoir depth of ~9.5 km (Table 8). Assuming a pressure of 2.7 kbar, two-feldspar thermometry for samples of the rhyolite of Bodie Hills rhyolite yields temperatures of 798° and 728°C (Eq. 27a of Putirka, 2008). The Zr content of titanite was used with the Zr-in-titanite thermobarometer (Hayden et al., 2008). Assuming $a\mathrm{SiO_2}$ = 1 and $a\mathrm{TiO_2}$ ~0.8 (in the absence of rutile with ilmenite and zircon present) and a pressure of 2.7 kbar, the thermometer yields temperatures of 740°±10°C, which is in accord with temperature ranges predicted by hornblende and feldspar thermometry.

TABLE 8 NEAR HERE

Al-in-hornblende thermobarometry yields a pressure of 4.3 (±0.3) kbar at 800°C for the trachyandesite of Willow Springs. Samples of this unit lack the two pyroxenes necessary to most accurately apply the Mg-in-apatite thermometer of Trail et al. (2012), but do have abundant large, equant, zoned apatite crystals that have high Mg rims that yield temperatures (~820±25°C) comparable with those calculated from hornblende compositions (Table 8). These high Mg rims are consistent with apatite growth in a higher temperature regime than that indicated by lower Mg apatite core compositions, which are consistent with lower temperatures. Consequently, the associated reservoir must have been heated, likely by mixing with newly intruded magma, immediately prior to eruption.

Al-in-hornblende thermobarometry results for the trachyandesite of Mount Biedeman suggest lower pressures (~1±0.1 kbar) that are commensurate with shallower reservoir depths (~3.8 km) at ~870°C (Table 8). Results for the trachyandesite of Mount Biedeman magma blob are more complex. Rims of large hornblende phenocrysts suggest pressures of 3.5 (±0.2) kbar

(~12 km depth) at 850°C, whereas the Al_2O_3 content of coexisting, smaller hornblende crystals yield a pressure of ~2 (±0.2) kbar at 900°C. Hornblende that forms rims on pyroxene crystals yield pressures of 4-5 kbar (13 to 16 km depth) and ~850°C, and hornblende in the magma blob host rock yield pressures of only about 1.2 (±0.1) kbar. Hornblende from the magma blob indicate pressures and therefore depths much greater than of the host trachyandesite, which suggests that the magma blob interacted with magma represented by the rhyolite of Bodie Hills in its deeper-seated reservoir. Higher still pressure estimates derived from hornblende overgrowths on pyroxene crystals contained in the magma blob may record a mixing event involving these pyroxene antecrysts and a still deeper reservoir.

Hornblende from one sample of the trachyandesite of Masonic has Al-in-hornblende compositions consistent with pressures of 1.5 (±0.2) kbar (~5.5 km depth) at ~865°C. Using the two pyroxene thermometer of Brey and Kohler (1990), compositions of clinopyroxene and orthopyroxene in trachyandesite of Masonic samples suggest temperatures of 900 to 910°C (at 1.5 kbar). A few trachyandesite of Masonic samples also contain oxide pairs in equilibrium. Compositions of these crystals suggest equilibration ~960°±30°C at fO_2 = NNO+1.2 (Ghiorso and Evans, 2008).

Volatile contents of magmas represented by diverse volcanic rock units of the BHVF likely varied considerably. Most hornblende and biotite phenocrysts in BHVF rocks have very low Cl contents but somewhat higher F contents (Supplemental Data Table 2). Rims of biotite phenocrysts in the rhyolite of Bodie Hills have particularly high F contents as do the rims of hornblende phenocrysts in one sample (09-BA-22) of the trachyandesite of Mount Biedeman; these rims may represent post-eruption biotite crystallization. Low F and Cl contents of biotite phenocrysts suggest that the magma represented by the trachyandesite of Willow Springs was halogen poor relative to the rhyolite of Bodie Hills and trachyandesite of Masonic magmas. Alternatively, these low halogen contents may reflect post-eruptive volatile loss.

Most apatite crystals, essentially ubiquitous in BHVF rocks, are composed of fluorapatite that has fairly elevated S and moderate Cl contents. Sulfur also forms sulfide mineral inclusions in apatite and in the groundmass (as pyrite, chalcopyrite, and a Mn-sulfide) of the trachyandesite of Mount Biedeman. The rims of abundant large, blocky, euhedral fluorapatite in the trachyandesite of Mount Biedeman are volatile depleted; S contents range from 800 to 1200 parts per million (ppm) and Cl from 4500 to 6000 ppm. These apatite crystals contain fairly low REE contents (~2000 ppm Ce, ~1000 ppm La, Pr, Nd) that are enriched in crystal rims. Apatite in the trachyandesite of Mount Biedeman magma blob has even higher S, >2000 ppm, but lower Cl, and these grains are small, bladed, and some are skeletal. Sulfur is incorporated into apatite via a SO_4^{-3} substitution for PO_4^{-3}, which is favored by elevated magmatic oxidation state (pressure and temperature also minimally impact the extent of this substitution). The high S content of apatite in the trachyandesite of Mount Biedeman magma blob and of apatite (~1500 ppm S) in the trachyandesite of Willow Springs suggest that magmas associated with the BHVF equilibrated at relatively high fO_2. Apatite crystals in the trachyandesite of West Brawley Peak are elongate, skeletal and contain rod-shaped sulfide inclusions. These relations are consistent with sulfide having been incorporated in growing apatite crystals as a liquid, which suggests the potential coexistence of immiscible sulfide and silicate melts. Melt immiscibility relations are consistent with textural and geochemical features that are also in accord with magma represented by the trachyandesite of West Brawley Peak having experienced rapid changes in temperature and melt chemistry.

Mineral chemical and textural features indicative of open-system behavior

Diverse textural and chemical features of BHVF phenocrysts are diagnostic of open-system behavior, including complex crystallization histories, magma reservoir recharge events, mixing/mingling processes, and degassing; these were important contributors to the petrogenesis of the magma reservoirs associated with the BHVF. These relations are especially well characterized by phenocrysts in the trachyandesites of Masonic, Mount Biedeman, Willow Springs, and West Brawley Peak, and the rhyolite of Bodie Hills (Supplemental Figs. 45-48).

Geochronologic data indicate that the trachyandesite of Mount Biedeman and rhyolite of Bodie Hills were, at least in part, coeval (Table 1) and field relations demonstrate that the corresponding magmas locally mixed (Figure 9P in John et al., 2012). The rhyolite of Bodie Hills contains large plagioclase and alkali feldspar phenocrysts that have very high Ba and Sr abundances that reflect inputs derived from mingled trachyandesite of Mount Biedeman magma blobs. Compositions of plagioclase in a trachyandesite of Mount Biedeman magma blob (sample 203381) entrained in rhyolite of Bodie Hills form three distinct populations: (1) coarse phenocrysts have An50:Ab48 compositions and contain ~700 ppm Sr and Ba, whereas small grains distributed throughout the groundmass define two additional, very distinct compositions: (2) An82:Ab18 (bytownite) that contains ~1000 ppm Sr, 500 ppm Ba, and (3) An57:Ab41 that contains ~1500 ppm Sr and 750 ppm Ba. The most calcic plagioclase phenocrysts in the magma blob likely represent those in equilibrium with magma represented by the trachyandesite of Mount Biedeman, whereas the two less calcic plagioclase phenocryst populations suggest magma blob interaction with a more felsic, lower Ca/Na melt. The lack of higher-Fe plagioclase in the magma blob confirms that magma represented by the trachyandesite of Mount Biedeman locally mingled and reacted with hot rhyolitic magma, thereby heating felsic magma already present in the reservoir.

Hornblende textures and compositions also suggest mixing between magma reservoirs represented by the rhyolite of Bodie Hills and trachyandesite of Mount Biedeman. Hornblende in the trachyandesite of Mount Biedeman magma blob preserves primary textural and compositional features, and large phenocrysts and small oriented groundmass grains have similar compositions. In contrast, hornblende in other samples (09-BA-19 and 09-BA-22) of the trachyandesite of Mount Biedeman include large intact grains with breakdown (decompression/dehydration) rims and large grains that are entirely replaced by pseudomorphous opacite. Hornblende breakdown and replacement probably reflects open-system processes such as magma mixing, reservoir recharge, and degassing due to eruption and decompression (Rutherford and Hill, 1993). Hornblende in the rhyolite of Bodie Hills also preserves primary textural and compositional features. Hornblende compositions in these units suggest their associated magma reservoirs formed at similar depths, ca. 10 km in the rhyolite of Bodie Hills and 7-12 km in the trachyandesite of Mount Biedeman magma blob. Finally, the presence of compositionally distinct (higher Al and Fe) hornblende overgrowths on pyroxenes in the magma blob likely also indicates interaction with felsic magma and provide further evidence of mixing.

Compositions and textural features of diverse phenocryst assemblages in the trachyandesites of Masonic, Mount Biedeman, Willow Springs, and West Brawley Peak provide many additional indications consistent with magma mixing. Texturally, hornblende and biotite phenocrysts in some trachyandesite of Willow Springs samples preserve primary textural features, whereas those in other samples include reaction rims, likely reflective of reservoir recharge events, or crystals partially to completely replaced by pseudomorphous opacite produced during eruption and decompression. For comparison, hornblende in the trachyandesite of Masonic preserves primary textural features, whereas that in the trachyandesite of West Brawley Peak preserves varying combinations of primary textures and reaction rims. Reversely zoned clinopyroxene grains from the oldest part of the trachyandesite of Masonic may constitute evidence of mafic recharge. Similarly, plagioclase contained therein is reversely compositionally zoned, with high Anorthite component rims and correspondingly higher Fe content, which probably reflect reservoir recharge by the addition of mafic melt.

Mining districts and alteration zones in the Bodie Hills volcanic field

Precious metals, mercury, and sulfur were concentrated by two types of hydrothermal systems that developed during Miocene magmatism in the Bodie Hills (Vikre et al., 2015). One type of system deposited sinters, veins, and fault-breccia-matrix fill that consist predominantly of quartz, lesser adularia, sericite, and calcite, and, locally, minable deposits of electrum, silver minerals, and cinnabar. These quartz-adularia deposits occur in veins in the Bodie and Aurora mining districts, and in sinter, silicified breccia, and subjacent veins in the Paramount–Bald Peak alteration zone, the Four Corners alteration zone, and near Spring Peak (Spring Peak sinter; Fig. 14). Gold-, silver-, and mercury-mineralized structures and sinters are mostly in (or on) Miocene lavas, lava domes, and volcaniclastic rocks. The second type of system is localized in fault zones in Miocene and Mesozoic rocks, and in large volumes of Miocene volcaniclastic deposits, lavas, and lava domes that have been partially to pervasively replaced by quartz and variable amounts of alunite, kaolinite/dickite, pyrite, pyrophyllite, sericite, and illite-montmorillonite. These quartz-alunite-altered rocks include gold-silver-copper deposits in the Masonic mining district and numerous alteration zones (Fig. 14) that cover several to several tens of square kilometers (the Red Wash-East Walker River, East Brawley Peak, Sawtooth Ridge, Aurora Canyon, Potato Peak, and Cinnabar Canyon US 395 alteration zones). The Potato Peak and Cinnabar Canyon-US 395 alteration zones contain mercury and sulfur deposits.

FIGURE 14 NEAR HERE

Globally, quartz-adularia and quartz-alunite deposits owe their distinctive attributes to formation from magmatically derived hydrothermal fluids that each have intrinsically different characteristics; these distinctions reflect magmatic degassing at different depths and variable mixing with groundwater and wallrock interaction. Quartz-adularia deposits form from H_2S-dominated fluids generated at somewhat greater depths and are less oxidized than those responsible for quartz-alunite deposit formation; these fluids include significant meteoric water inputs, are largely in equilibrium with wallrocks, and have near-neutral pH. In contrast, SO_2-dominated hydrothermal fluids responsible for quartz-alunite deposit formation are dominated by magmatic inputs; these low pH fluids are more oxidized than those responsible for quartz-adularia deposit formation, and are significantly out of equilibrium with enclosing wallrocks. In the BHVF, magmatic-hydrothermal fluid generation at different depths produced fluids with significantly different characteristics, which caused formation of the two distinctly different epithermal mineral deposit types.

Quartz-adularia Au-Ag-Hg sinter-vein deposits

In the Bodie district, ~1.46 Moz. of gold and 7.28 Moz. of silver were produced primarily during the period 1877-1913 from N25°E-trending, mostly steeply dipping veins. Early-mined veins (1877-1881) contained >1 to many ounces of gold per ton. Veins, hosted in ~9.1-8.9 Ma dacite of Silver Hill, range in age from ~8.9 to 8.1 Ma (based on $^{40}Ar/^{39}Ar$ adularia dates; Fleck et al., 2015) and most are <2 m wide. Mineralogy, texture, cross-cutting relationships, element concentrations, wall rock alteration, and age define three vein series: (1) Incline series veins, (2) Burgess series veins, and (3) Silver Hill series veins (Fig. 15). The ~8.3-8.1 Ma Incline series veins, from which most gold and silver were recovered consist of tens to hundreds of millimeter-thick layers of fine-grained quartz, adularia, lesser metallic minerals, and quartz perimorphs of bladed calcite that parallel wall rock contacts. Layers symmetrically filled centimeter- to meter-wide open fractures from vein margins inward. Layers that include metallic minerals, mostly electrum and acanthite, compose no more than several volume percent of ore-grade veins. Elevated concentrations of arsenic, antimony, and manganese in some bulk vein samples suggest the presence of other silver minerals, and former calcite or replaced carbonate minerals. Incline series veins have sharp contacts with the enclosing dacite, proximally altered to quartz, adularia, and lesser illite and pyrite, which retains its primary volcanic texture. Distal alteration minerals include illite, chlorite, montmorillonite, and calcite.

FIGURE 15 NEAR HERE

The ~8.5-8.4 Ma Burgess series veins consist of quartz, and lesser adularia, Mg-Fe-K-Al silicate minerals, metallic minerals, and calcite that are generally coarser grained and less distinctly layered than Incline series veins. Metallic minerals in layers and small aggregates include electrum, acanthite, and minor amounts of sphalerite, galena, and other Ag-Cu-As-Sb-S-Se minerals, and seldom exceed several volume percent. Only a few elements (arsenic and antimony), other than gold and silver, are concentrated in bulk vein samples. Dacitic wall rocks and internal septa in veins are altered to quartz, adularia, illite, and pyrite, which partially obscure primary volcanic rock textures adjacent to veins.

The ~8.9-8.5 Ma Silver Hill series veins contain significantly larger proportions of metallic minerals, relative to electrum and silver minerals, than Incline and Burgess series veins. These veins consist of quartz, lesser adularia, barite, illite, and calcite, and often ≥10 volume percent metallic minerals, including electrum, tetrahedrite, pyrargyrite, acanthite, sphalerite, galena, chalcopyrite, pyrite, hessite, sylvanite, and bornite. These minerals replaced fault breccia clasts and matrices, and filled open spaces between fault breccia clasts. In addition to elevated gold, silver, copper, lead, and zinc concentrations, bulk vein samples commonly contain tens to hundreds of ppm As, Sb, Bi, Cd, Mo, Sn, and Te. Dacite in breccia fragments and adjacent to veins is altered to quartz, illite, kaolinite, montmorillonite, and pyrite; most primary igneous textures are partially obscured.

The Aurora district includes hundreds of en echelon veins and vein segments that are exposed within a ~7.5 km by 1 km, northeast-trending corridor. Approximately 1.8 Moz. of gold and 20.6 Moz. of silver were produced from these veins during the period 1860-1998; ore mined during the initial years of production (1860-1864) reportedly contained >1 oz. per ton gold. The ~10.5 Ma veins (based on $^{40}Ar/^{39}Ar$ adularia dates) strike predominantly N45-70°E, dip shallowly to steeply southeast, are mostly <2 m wide, and are hosted in ~13.1-12.6 Ma trachyandesite of Aurora and ~11.2 rhyolite of Aurora Creek (Fig. 15); all productive veins are trachyandesite hosted. Most veins consist of several to hundreds of millimeter-thick layers of fine-grained quartz, lesser adularia, metallic minerals, sericite, and calcite, and uncommon barite and fluorite, which symmetrically filled centimeter- to meters-wide open fractures from vein margins inward. These veins strongly resemble Incline series veins in the Bodie district. Other mineralized structures include (1) the north-trending, ≥10-meter-wide Esmeralda vein, a near vertical zone of stock work veins and fault breccias cemented by several generations of quartz, calcite, adularia, and metallic minerals, and (2) vein zones that consist of meters-wide groups of subparallel and structurally contiguous vein segments that were, in part, bulk-mined. Metallic minerals in layered veins and breccia matrices include pyrite, electrum, acanthite, naumannite, sphalerite, galena, chalcopyrite, arsenopyrite, tetrahedrite, and polybasite. In addition to elevated concentrations of elements contained in these minerals, some bulk vein samples also contain elevated concentrations of Mo, Bi, and Te. Trachyandesitic wall rocks and septa in veins and vein zones are altered to quartz, adularia, sericite, illite, montmorillonite, and pyrite, which partially obscure igneous texture. Alteration minerals in wall rocks distal to veins include montmorillonite, sericite, quartz, calcite, chlorite, albite, and pyrite (Osborne, 1991).

At the Paramount mine, small amounts of mercury (tens of flasks) were produced from a metacinnabar-chalcedonic quartz vein in a sequence of silicified Miocene volcaniclastic strata and sinters. Near Spring Peak, cinnabar is contained in sinter terrace deposits that overly Miocene volcaniclastic and Mesozoic granitic and metamorphic. These mercury deposits, and other groups of sinter and silicified breccia deposits in the Paramount–Bald Peak and Four Corners alteration zones (Fig. 14), represent paleosurface and near-surface hydrothermal mineral assemblages of sinter-vein systems, some of which include subjacent, gold- and silver-mineralized quartz±adularia veins. Veins near the Paramount mine and stratigraphically beneath the Spring Peak sinter contain several to tens of ppm gold and silver, tens to hundreds of ppm mercury, and hundreds to thousands of ppm arsenic and antimony (Vikre et al., 2015; http://www.kineticgold.com/s/SpringPeak.asp). The ages of sinters and veins in the Paramount–Bald Peak alteration zone are stratigraphically constrained to ~9.7-9.3 Ma. The Spring Peak sinter-vein system is hosted, in part, in rhyolite that is probably 11.2-9.9 Ma, based on the age (Fleck et al., 2015) of similar rhyolite (rhyolites of Bodie Creek, Del Monte Canyon, Aurora Creek, and East Brawley Peak) in the East Brawley Peak and Sawtooth Ridge alteration zones, and in the Aurora district (Fig. 14) ~3-8 km west and northwest of the Spring Peak sinter terraces.

Quartz-alunite Au-Ag-Cu-Hg-S deposits and alteration zones

In the Masonic district, ~0.060 Moz. of gold, 0.040 Moz. of silver, and small amounts of copper were recovered from high-angle fault zones and stratiform deposits in ~15-14.1 Ma trachyandesite of Masonic and pre-Tertiary granitic and metamorphic rocks. Fault zones were mostly mineralized at ~13 Ma (Fleck et al., 2015; Vikre et al., 2015), as indicated by $^{40}Ar/^{39}Ar$ dates on alunite (NE Masonic alunite, Fig. 15). Stratiform deposits, hosted by volcaniclastic strata and lava flows, formed at ~13.4-13.3 Ma (SW Masonic alunite, Fig. 15; Fleck et al., 2015; Vikre et al., 2015). Hydrothermal minerals in both deposit types include quartz, alunite, kaolinite, pyrite, barite, enargite, and numerous Cu-As-Sb-Fe-Bi-Au-Ag-S-Se-Te minerals in very fine-grained aggregates and as inclusions primarily in enargite. Bulk altered rock samples with visible metallic minerals contain tens to hundreds of ppm Au, Ag, Hg, Se, Sn, and W, and hundreds to thousands of ppm Cu, As, Bi, Pb, Sb, and Te. Wall rocks adjacent to fault zones and fault zone breccia fragments are altered to quartz, alunite, kaolinite, and pyrite that are paragenetically earlier than copper and other metallic minerals. Within meters of faults, these proximal assemblages grade into distal assemblages that include sericite, illite-montmorillonite, and pyrite. Alteration mineral assemblages, dominantly quartz, alunite, kaolinite, and pyrite, associated with the stratiform deposits are co-spatial with, and in part paragenetically earlier than, metallic minerals. Some enargite was deposited with quartz (or initially a fine-grained silica phase) as chemical sediments within bedded sequences of variably sorted volcaniclastic detritus (Vikre et al., 2015).

Other, variably sized (ca. 1 to ca. 30 km^2) quartz-alunite alteration zones (Fig. 14) are hosted in Miocene volcaniclastic rocks and lava flows that have been partially to completely replaced by quartz, alunite, kaolinite/dickite, pyrophyllite, pyrite, and other hydrothermal minerals (Red Wash-East Walker River, Aurora Canyon, Potato Peak, Cinnabar Canyon-US 395, Sawtooth Ridge, and East Brawley Peak alteration zones). $^{40}Ar/^{39}Ar$ dates of ~13.6-8.2 Ma on alunite (Fleck et al., 2015; Vikre et al., 2015) indicate episodic alteration that was simultaneous with local magmatism (Fig. 15). The extent of alteration zones, as reflected by areas of altered rocks, is broadly commensurate with the distribution of volcaniclastic strata, which constitute major parts of most of the eruptive centers, where they are proximal to younger intrusions. The large Red Wash–East Walker River and Cinnabar Canyon–US 395 alteration zones, which cover tens of square kilometers (Fig. 14), reflect high-fluid-permeability debris flow and other volcaniclastic deposits interbedded with lava flows. The smaller Aurora Canyon and Potato Peak alteration zones (Fig. 14) are mostly hosted within less permeable and reactive lava flows, where pervasive alteration is largely confined to small-volume clastic strata and brecciated flows.

Many quartz-alunite alteration zones do not contain economically significant ore metal concentrations, but several contain small to significant mercury and sulfur deposits. Several tens of flasks of mercury were recovered from brecciated, clay-altered, and silicified volcaniclastic strata and flows in the Cinnabar Canyon–US 395 and Potato Peak alteration zones (Fig. 14). A concealed sulfur deposit (16.1 Mt @ 17.9 weight percent S; Ward, 1992) is hosted in a sequence of volcaniclastic strata and lava flows beneath the mercury deposit in the Cinnabar Canyon–US 395 alteration zone. $^{40}Ar/^{39}Ar$ dates on alunite (Fleck et al., 2015; Vikre et al., 2015) indicate that the mercury deposit in the Potato Peak alteration zone formed at ~10.8 Ma, whereas the mercury and sulfur deposits in the Cinnabar Canyon–US 395 alteration zone formed between ~8.8 and 8.2 Ma (Fig. 15).

Time-space relationships of hydrothermal systems and magmatism

In most mining districts and alteration zones associated with the BHVF, $^{40}Ar/^{39}Ar$ dates of hydrothermal and igneous minerals (Fig. 15) and stratigraphic relations demonstrate that both types of hydrothermal systems and their host volcanic rocks are broadly coeval. These temporal relations, and the thermochemistry of hydrothermal mineral assemblages (Fig. 16), indicate that magmas supplied the thermal energy that powered the hydrothermal systems. However, volcanic rocks that host mined veins in the Bodie and Aurora districts (9.07 Ma dacite of Silver Hill and 12.89 Ma trachyandesite of Aurora, respectively), are as much as ~0.8 to 2.1 m.y. older than some of the hydrothermal minerals in these districts. The temporal discrepancy suggests that magmas other than those represented by host rocks provided heat for the hydrothermal systems that deposited Incline and Burgess series veins at Bodie, as well as veins at Aurora (Fig. 14). However, volcanic rocks younger than the dacite of Silver Hill have not been identified in or around the Bodie district. The nearest eruptive rocks similar in age to Incline and Burgess series veins (~8.6-8 Ma trachyandesite of Willow Springs) are ~7 km west of the district in the Cinnabar Canyon–US 395 alteration zone (Figs. 14 and 15). Alternatively, evidence of open-system behavior preserved in many BHVF rocks, including the dacite of Silver Hill, is consistent with the presence of a solidified magma reservoir, younger than and beneath the dacite of Silver Hill, that may be the progenitor of the ore deposits in the Bodie district. Magma(s) responsible for hydrothermal mineralization in the Aurora district may be represented by ~11-10 Ma volcanic rocks exposed ~4-5 km northwest and west of mined veins (trachyandesite of Del Monte and rhyolite of Bodie Creek; Fleck et al., 2015; John et al., 2015).

FIGURE 16 NEAR HERE

Thermochemical distinctions between hydrothermal systems

Comparison of hydrothermal mineral assemblages produced by quartz-adularia and quartz-alunite hydrothermal systems associated with the BHVF to experimentally determined mineral equilibria at elevated temperatures indicates thermochemical conditions responsible for the two types of system were distinct. Coexisting pyrite, acanthite (argentite at temperatures greater than ~177°C), adularia, sericite, and quartz in the quartz-adularia veins at Bodie and Aurora are indicative of near-neutral pH fluids at 250°C, the approximate maximum fluid temperature indicated by fluid inclusion microthermometry (Osborne, 1985; 1991; Romberger, 1991b; Knudsen and Prenn, 2002;). Hypogene kaolinite associated with Silver Hill series veins at Bodie (Vikre et al., 2015) reflects somewhat lower pH fluid during initial vein deposition (Fig. 16a). Alunite±kaolinite+pyrite in Au-Ag-Cu-mineralized fault zones and stratiform deposits at Masonic, and in quartz-alunite alteration zones, reflect deposition by more acidic, oxidized (expressed by fO_2), and sulfur-rich fluids; S isotope fractionation indicates fluid temperatures <250°C (Vikre and Henry, 2011; Fig. 16a). Concentrations of silver in electrum (expressed as X_{Ag}) and iron in sphalerite (expressed as X_{FeS}), where constrained by coexisting silver (acanthite) and iron (pyrite) minerals, respectively, further distinguish quartz-adularia veins at Bodie and Aurora from quartz-alunite-altered fault zones and stratiform deposits at Masonic. X_{Ag} in electrum and X_{FeS} in sphalerite are higher in Bodie and Aurora veins than in Masonic deposits, which reflects different sulfur activities (expressed as fS_2; Fig. 16b) during precipitation of these minerals. In addition, Silver Hill series veins at Bodie and veins in the Aurora district contain tetrahedrite, whereas enargite is common in all Masonic deposits; these occurrences are consistent with other mineral equilibria (Fig. 16b).

Petrologic and tectonic evolution of the Bodie Hills volcanic field

Major oxide compositions of volcanic rocks in the southern segment of the ancestral Cascades magmatic arc (du Bray et al., 2014), and similarly those of BHVF rocks, are consistent with petrogenesis in a subduction-related, continental magmatic arc setting. Specifically, most of these rocks are subalkaline and have intermediate compositions similar to those (1) characteristic of modern Cascades arc magmatism (Supplemental Fig. 6) and (2) associated with melting, assimilation, storage, and homogenization (MASH, Hildreth and Moorbath, 1988) processes that govern continental arc magmatism. Major oxide abundance variations for the BHVF as a whole are consistent with crystallization and fractionation involving the observed phenocryst phases. Among rocks of the BHVF, the onset of sodic plagioclase crystallization and its fractionation is denoted by decreasing Al_2O_3 and Na_2O abundances (Fig. 6), which pertains only to magmas with ≥65 wt% SiO_2. Small magnitude of Eu/Eu* anomalies among intermediate composition rocks of the BHVF also imply limited plagioclase fractionation. Systematic decreases in the abundances of TiO_2, FeO*, MgO, and CaO with increasing SiO_2 content (Fig. 6) are all consistent with clinopyroxene, hornblende, biotite, and lesser Fe-Ti oxide and olivine crystallization and fractionation. Among rocks of the BHVF, significant and systematic increases in K_2O

abundances with increasing SiO_2 indicate its concentration in fractionated, residual magmas. The potassic character of BHVF eruptive products may reflect lithospheric delamination and subsequent partial melting of a K_2O-enriched lower-crust or upper-mantle source (Feldstein and Lange, 1999; Farmer et al., 2002). Alternatively, elevated K_2O abundances may result from low-degree partial mantle melting and subsequent fractional crystallization (Putirka and Busby, 2007). Highly variable P_2O_5 abundances in samples with less than about 65 wt% SiO_2 may reflect source inhomogeneity with regard to P_2O_5. In contrast, more systematic P_2O_5 abundance decreases among BHVF rocks with more than about 60 wt% SiO_2 probably signal the onset of apatite fractionation. Progressively larger magnitude negative P and Ti anomalies (Fig. 10) are also diagnostic of apatite and Fe-Ti oxide mineral crystallization and fractionation among increasingly felsic rhyolite units of the BHVF.

Mantle components

Combined major, trace element, and isotopic data constrain the composition of potential mantle sources and extent to which BHVF magmas were contaminated by crustal components. The most mafic volcanic rocks, the trachyandesite of Masonic and the basaltic trachyandesite of Rancheria have initial $^{87}Sr/^{86}Sr$ as high as 0.70579 and have among the lowest Pb isotope ratios of BHVF rocks (Fig. 10). Given their mildly alkaline compositions (Fig. 5) and low SiO_2 contents, the associated magmas were probably little contaminated by crustal assimilants and therefore indicate derivation of BHVF magmas from an enriched mantle source with $^{87}Sr/^{86}Sr$ ~0.7055 and εNd ~-3. Mantle sources with these characteristics are common beneath the ancestral Cascades arc, southern segment, and the Western Great Basin (Ormerod et al., 1991; Cousens et al., 2008). However, two samples of ca. 11 Ma BHVF trachyandesite have low initial $^{87}Sr/^{86}Sr$ and $^{206}Pb/^{204}Pb$ compared to all other BHVF rocks (Fig. 12). A more depleted mantle source, with $^{87}Sr/^{86}Sr$ as low as 0.7040, must be involved in the petrogenesis of these rocks, because initial $^{87}Sr/^{86}Sr$ values are generally not lowered by crustal contamination. This depleted mantle source is only evident in ca. 11 Ma BHVF rocks, and the overall higher initial $^{87}Sr/^{86}Sr$ values characteristic of <11 Ma BHVF rocks suggests that the proposed depleted source did not thereafter contribute to BHVF magmatism. Cousens et al. (2008) proposed that lavas of the ancestral Cascades arc, southern segment in the Lake Tahoe area were derived from two sources, the mantle wedge (low initial $^{87}Sr/^{86}Sr$) and metasomatized sub-continental lithospheric mantle (high initial $^{87}Sr/^{86}Sr$). The flare-up of magmatic activity in the BHVF at ca. 11 Ma, combined with the subsequent termination of magmatism bearing the isotopic signature of a depleted source (slab-modified mantle wedge?), may reflect passage of the south edge of the Farallon plate beneath the BHVF area at about this time. Northward passage of the Farallon plate edge may have contributed to increased magmatism coincident with a potentially leaky plate margin passing through the BHVF region. Similarly, the end of magmatism bearing depleted mantle wedge source signatures reflects this potential source passing northward, away from the locus of BHVF magmatism, and being supplanted by mantle having different isotopic signatures.

Crustal influences

Trace element abundance variations among the BHVF rocks appear to be principally controlled by MASH zone processes (Hildreth and Moorbath, 1988) and the superimposed effects of crystallization and fractionation; abundance variations of several key trace elements constrain the nature and extent of these petrogenetic processes. Abundances of Zr vary considerably and unsystematically among rocks of the BHVF with less than about 70 wt% SiO_2 (Supplemental Fig. 25). These variations suggest source region inhomogeneity with respect to Zr abundances and inconsistent attainment of zircon saturation, likely related to host magma composition and temperature (Watson, 1979). The more systematic decrease of Zr abundances among rocks with more than 70 wt% SiO_2 probably represents the onset of Zr saturation followed by zircon crystallization and fractionation. Sr abundances of the BHVF rocks (Supplemental Fig. 18) are generally significantly greater than those of the modern High Cascades arc (du Bray et al., 2014) and are considerably elevated relative to those characteristic of the Andean arc (Hildreth and Moorbath, 1988). Sr-enriched arc magmas are likely generated beneath thick continental crust at elevated pressures under plagioclase-unstable conditions (Green, 1982; Hildreth and Moorbath, 1988). Consequently, elevated Sr abundances suggest that magmas represented by the BHVF rocks reflect partial melting in the mantle beneath thick continental crust at pressures greater than about 20 kb (70 km depth). Most BHVF rocks have relative abundances of Rb and Y + Nb that are also consistent with a genesis in a volcanic arc setting (Fig. 17). Negative Nb-Ta anomalies (Fig. 10) are similarly in accord with genesis of all BHVF magmas in a continental magmatic arc setting; the nature and extent of these anomalies differ minimally among the intermediate versus felsic eruptive products.

FIGURE 17 NEAR HERE

Most continental magmatic arc rocks have Ba/Nb >15 (Gill, 1981). For rocks of the BHVF, minimum Ba/Nb values are about 30 and range upward to almost 400; values from 100 to 200 are most common (Supplemental Fig. 49). BHVF rock Ba/Nb values do not vary systematically with respect to either age or composition, although values generally decrease among BHVF rocks with greater than 70 wt% SiO_2, probably as a consequence of feldspar and biotite crystallization and fractionation. Elevated Ba/Nb has been associated with derivation of subducted slab components from mantle wedge magmas generated by slab dehydration and fluid-flux-induced partial melting (Hawkesworth et al., 1995; Pearce and Peate, 1995; Cousens et al., 2008; Schmidt et al., 2008). Highly elevated Ba/Nb ratios, prominent negative Nb-Ta anomalies, and significant LILE enrichments all suggest the presence of a slab-derived fluid component in magmas represented by the BHVF rocks.

Petrogenetic processes that influenced compositional characteristics of the BHVF rocks are further constrained by REE systematics. Moderately steep negatively sloped chondrite-normalized REE patterns with LREE versus HREE enrichment are principal features of these rocks (Fig. 9). Hildreth and Moorbath (1988) observed that modern Andean magmatic arc rocks are also preferentially LREE enriched, which they attribute to partial melting in a high-pressure, garnet-stable regime. Garnet is a HREE and Y reservoir; its retention in the partial melt residuum causes HREE and Y depletion from derived magmas. High Sr/Y characteristic of BHVF rocks (Supplemental Fig. 50) is also diagnostic of high pressure, garnet stable–plagioclase unstable partial melting. Although these adakitic compositions have been considered diagnostic of volatile-fluxed subducted slab melting, Richards and Kerrich (2007) have demonstrated that ordinary subduction-related processes that do not require melted subducted slab inputs can generate magmas with these distinctive compositions. MREE to HREE depletion, as indicated by somewhat U-shaped MREE to HREE pattern segments (Fig. 9), is another primary feature of the BHVF rocks. REE mineral/melt partition coefficients for amphibole are greatest for the MREE, especially Dy (Davidson et al., 2007). Consequently, BHVF-rock MREE depletion is consistent with amphibole fractionation; continuously decreasing Y abundances with increasing SiO_2 (Supplemental Fig. 20) are also consistent with hornblende fractionation (Sisson, 1994). Weakly developed negative Eu anomalies characteristic of the intermediate composition BHVF rocks (Table 4) are consistent with source-region plagioclase instability and consequent Eu partitioning into partial melts rather than residuum retention. These small-magnitude anomalies suggest the relative unimportance of plagioclase fractionation relative to the petrogenesis of intermediate composition BHVF rocks but hornblende and zircon fractionation and attendant MREE and HREE depletion may have suppressed the magnitude of negative Eu anomalies formed in BHVF rocks as a result of plagioclase fractionation. High Sr contents of the most primitive BHVF rocks (basaltic trachyandesite of Rancheria) are also consistent with plagioclase instability in the melting zone.

The two distinct groups of average chondrite-normalized REE patterns for the BHVF units provide additional insights concerning the petrogenesis of these rocks (Fig. 9). Within each of the two groups, patterns are quite similar, especially considering the compositional and age diversity of the associated rock units. Patterns for the intermediate composition group have similar slopes (equivalent $(La/Yb)_N$) and small, negative Eu anomalies of similar magnitude; slight overall REE abundance variations among group members are the sole feature that distinguish patterns within this group. Essentially invariant Eu/Eu* among these rocks indicates small, equivalent amounts of plagioclase fractionation among magmas represented by all of these rock units. Among the average REE patterns for the felsic BHVF rock unit group, LREE abundances define a narrow range, the magnitude of negative Eu anomalies is somewhat variable, and MREE to HREE abundances vary over a relatively broad range. These variable magnitude negative Eu anomalies indicate a significant role for plagioclase and apatite fractionation in the petrogenesis of these rocks and that the extent of plagioclase fractionation varied considerably among the magmas represented by the felsic BHVF rock unit group. Although MREE to HREE abundances for the felsic units of the BHVF are lower than those for the intermediate-composition groups, their REE abundances are not characterized by lower Ho/Ho* values (Table 4), which precludes hornblende fractionation as the cause of lower MREE and HREE abundances among these rocks. More likely, overall MREE to HREE depletion among these felsic rocks reflects the effects of MREE- to HREE-enriched titanite and HREE-enriched zircon crystallization and fractionation from the associated magmas. Alternatively, the REE characteristics of the felsic BHVF rocks that distinguish them from those of BHVF intermediate composition rocks may reflect subtle compositional differences in the sources and/or contaminants that contributed to the petrogenesis of these two groups of rocks. For both groups of REE patterns, the absence of REE pattern rotation among rock unit-average patterns precludes REE-enriched accessory minerals having a dominant role in the petrogenetic evolution

(DOI will not work until issue is live.) DOI: http://dx.doi.org/10.2138/am-2016-5440

of the associated magmas. Small overall REE depletions among the intermediate composition rock units constrain REE bulk distribution coefficients for fractionated mineral assemblies to values only slightly greater than one, for each of the REE.

Combined trace element and isotope ratios distinguish crustal contamination trends among magmatic suites (Fig. 18). Among BHVF rocks, Pb/Ce increases from ~0.1 to ~0.6 in mafic- through intermediate-composition rocks, and then increases to >0.8 in the high-silica dacites and rhyolites (Supplemental Fig. 51). Higher Pb/Ce values likely reflect either (1) an increase in the subducted slab component added to mantle-derived melts during subduction (Cousens et al., 2011) or (2) greater assimilation of Pb-rich crustal rocks during MASH processes (Hildreth and Moorbath, 1988). The observed positive correlation between Pb/Ce values and SiO_2 content probably reflects the more evolved magmas having assimilated larger amounts of crustal components. Initial $^{87}Sr/^{86}Sr$ values for intermediate-composition BHVF rocks largely correlate positively with 1/Sr, Rb/Sr, and Pb/Ce values (Fig. 18), which is consistent with interaction between mantle-derived magmas and Rb- and Pb-rich crustal rocks. Furthermore, trace element-isotope ratio trends indicate that the crustal contaminant had an initial $^{87}Sr/^{86}Sr$ ~0.7060 and $^{206}Pb/^{204}Pb$ ~19.05. Initial $^{87}Sr/^{86}Sr$ values for BHVF rhyolites span a small range and have values overlapping those characteristic of the intermediate rocks (Fig. 18), which indicates that magmatic evolution from andesitic to rhyolitic compositions involved only limited additional interaction with crustal rocks. Pb isotope ratios for BHVF rhyolites are variable and also overlap Pb isotope ratios of nearly all BHVF intermediate rocks (Fig. 18), which suggests that the crust involved in andesite through rhyolite petrogenesis had more heterogeneous Pb than Sr isotopic compositions. Nd isotope ratios in BHVF mafic and intermediate rocks are highly variable over small 1/Nd, Sm/Nd, and Pb/Ce ranges (Fig. 18). Most BHVF rhyolites have $^{143}Nd/^{144}Nd$ <0.5125 (ε_{Nd} <-2) that may also reflect the composition of the crustal contaminant. Again, these values overlap those of the least-radiogenic intermediate-composition BHVF rocks, which is also consistent with minimal additional crustal interaction during BHVF rhyolite petrogenesis.

FIGURE 18 NEAR HERE

Importantly, the isotopic data do not require significant contamination by crustal components because isotopic data for the BHVF mafic- and intermediate-composition rocks largely overlap; assimilation of crust to generate more silicic magmas would result in an associated radiogenic isotopic shift. Even the BHVF rhyolites have isotopic compositions similar to those of some mafic rocks. However, some crustal interaction is required in the petrogenesis of all BHVF rocks to account for observed Pb/Ce versus SiO_2 variations.

Geochemical and petrographic data as well as field relations constrain the volcanological processes that contributed to the petrogenesis of the BHVF rocks. In particular, considerable petrographic evidence, especially plagioclase that is oscillatory zoned, partly resorbed, sieve textured, and includes variable, within-sample size populations, suggest that the associated magma reservoirs evolved by open-system behavior, especially periodic recharge. Multiple size populations of plagioclase and hornblende, each with distinct compositions, are also consistent with open-system behavior. Similarly, the broad compositional ranges characteristic of many BHVF eruptive units, especially the products associated with the large, long-lived stratovolcanoes and lava dome complexes, is consistent with the importance of recharge and incomplete homogenization to evolution of BHVF magma reservoir contents. Large, temporally nonsystematic SiO_2 abundance fluctuations among products erupted from closely spaced BHVF eruptive centers between about 11.7 and 9.3 Ma require essentially coeval magmatism associated with a number of small, discrete, compositionally distinct reservoirs. However, the presence of magma blobs of hornblende-rich trachyandesite of Mount Biedeman in numerous exposures of the rhyolite of Bodie Hills surrounding the center of the Mount Biedeman stratovolcano (Table 1), as well as their overlapping ages, indicate that magma reservoirs represented by these units were coeval, cospatial, and locally mingled.

With passage of the Mendocino triple junction north through the Bodie Hills region about 9 Ma (Atwater and Stock, 1998; Putirka et al., 2012), subduction of the Farallon plate beneath North America in the Bodie Hills area ceased, thereby eliminating subduction-related inputs to ongoing magmatism. However, volcanism continued in the BHVF after 9 Ma, as manifest by significant magma volumes erupted as the trachydacite of Potato Peak, trachyandesite of Willow Springs, and the rhyolite of Big Alkali. These units have geochemical features, including well-developed negative Nb-Ta anomalies, diagnostic of continental arc magmatism. Younger, 3.9 Ma to present-aged rocks in the adjacent Aurora volcanic field (Lange and Carmichael, 1996; Kingdon et al., 2013) erupted in an extensional, continental rifting tectonic setting generally associated with bimodal basalt-rhyolite magmatism (Christiansen and Yeats, 1992; Ludington et al., 1996; John, 2001). However, even these rocks preserve many geochemical signatures characteristic of arc magmatism. These relations suggest that at least 10 m.y. may be required following the cessation of subduction to eliminate the geochemical vestiges of arc-related inputs from ongoing, nonsubduction-related magmatism (Putirka et al., 2012).

Magmatism throughout the southern segment of the ancestral Cascades arc involved significant crustal contamination (Farmer et al., 2002; Cousens et al., 2008; du Bray et al., 2014). Similarly, variable crustal contamination contributed to compositional diversity and evolution characteristic of the BHVF. Primary, mafic magmas that assimilate crustal contaminants predictably evolve to more silicic compositions characterized by progressively lower P_2O_5/K_2O, because crustal materials generally have $P_2O_5/K_2O < 0.1$ (Farmer et al., 2002). Among rocks of the BHVF, P_2O_5/K_2O decreases with increasing SiO_2 content and increases with increasing MgO content (Supplemental Figs. 52-53), which confirms that some of the BHVF magmas evolved to intermediate or silicic compositions by variable contamination of primary mafic partial melts by crustally derived inputs. Similarly, Cousens et al. (2008) suggested that decreasing CaO/Al_2O_3 and increasing La/Sm and Zr/Sm with increasing SiO_2 principally reflect crustal contamination. Among rocks of the BHVF, CaO/Al_2O_3 decreases, whereas La/Sm and Zr/Sm increase with increasing SiO_2 (Supplemental Figs. 54-56), which corroborates the importance of progressive crustal contamination in development of the intermediate and felsic rocks erupted within the BHVF. Subtly elevated Sr_i values among BHVF rocks with the highest SiO_2 contents constitute a compelling radiogenic isotope argument consistent with the petrogenesis of these rocks including significant crustal contamination.

The BHVF, along with the Central Sierra Nevada Volcanic Province (Putirka et al., 2012), are prominent components of the southern segment of the ancestral Cascades arc. Arc magmatism migrated in a southwesterly direction across Nevada through the Eocene and Miocene, and became firmly established in the eastern Sierra Nevada at 15-20 Ma (Cousens et al., 2008; du Bray et al., 2014). Compared to ancestral Cascades arc volcanism in the Lake Tahoe region, BHVF and Central Sierra Nevada volcanic field lavas generally have higher initial $^{87}Sr/^{86}Sr$ values that overlap those of the most radiogenic Lake Tahoe arc rocks (Fig. 19). In contrast, isotopic compositions of post-arc (<3 Ma, post-dating northward passage of the south edge of the Juan de Fuca plate) volcanic rocks from the Lake Tahoe region are more radiogenic and overlap those of both BHVF and Central Sierra Nevada volcanic field lavas. However, none of these rocks have radiogenic isotope compositions as enriched as is common elsewhere in the

(DOI will not work until issue is live.) DOI: http://dx.doi.org/10.2138/am-2016-5440 11/4

western United States (Fig.19). Cousens et al. (2008) demonstrated that arc volcanism in the Lake Tahoe region included magmas derived from two mantle sources: the mantle wedge and sub-Sierran lithospheric mantle. The Lake Tahoe post-arc magmas were derived dominantly from lithospheric mantle (Cousens et al., 2011). Wedge-derived magmas generally have lower $^{87}Sr/^{86}Sr$ than lithospherically derived magmas. Assuming that the isotopic composition of the lithospheric mantle beneath the central eastern Sierra Nevada is relatively homogeneous, the isotopic similarity between the Lake Tahoe post-arc, Central Sierra Nevada volcanic field rocks and BHVF rocks suggests that all were derived primarily by lithospheric mantle melting, possibly including a minor mantle wedge component; the resultant magmas were subsequently contaminated by assimilation of crustal rocks. In the BHVF, rare andesites with low $^{87}Sr/^{86}Sr$ (~0.704) probably reflect major mantle wedge source contributions. One Central Sierra Nevada volcanic field andesite and andesites from the Dry Lake (Tahoe post-arc) field also have low initial $^{87}Sr/^{86}Sr$ compared to other lavas included with those suites.

FIGURE 19 NEAR HERE

Post-BHVF volcanic suites in the eastern Sierra Nevada, including the Long Valley/Mono system immediately south of the Bodie Hills, the Big Pine volcanic field in the Owens Valley, and the Aurora volcanic field in the southeast Bodie Hills, have consistently higher initial $^{87}Sr/^{86}Sr$ than rocks of the BHVF (Metz and Mahood, 1985; Halliday et al., 1989; Kelleher and Cameron, 1990; Ormerod et al., 1991; Christensen and DePaolo, 1993; Beard and Glazner, 1995; Cousens, 1996; Bailey, 2004; Kingdon et al., 2013, 2014). Most studies of these younger volcanic rocks identify lithospheric mantle as the source of associated mafic magmas. For instance, Long Valley mafic magmas are more radiogenic than BHVF mafic rocks (Cousens, 1996; Bailey, 2004). Since only a few million years separate mafic magmatism at the BHVF and Long Valley, it is unlikely that the isotopic distinction is due to radiogenic ingrowth of the lithospheric mantle. Instead, either lithospheric mantle beneath Long Valley has a more enriched composition than that beneath the BHVF, or BHVF mafic rocks include a minor mantle wedge component. Concurrently, felsic BHVF magmas are also less radiogenic than felsic rocks of the Long Valley/Mono Domes system (Fig. 19). If lower or upper crust contributed to felsic magmas in both suites, the crust must be more radiogenic south of the BHVF. Alternatively, or in addition, the relatively radiogenic character of the Long Valley and Owens Valley rocks may reflect contamination by older, more evolved crustal contributions reflective of their position on the continental side of the Sr_I ≥0.706 line.

Implications

The BHVF is a large (>700 km^2) volcanic field within the ancestral Cascades magmatic arc. Magmatic activity in the BHVF began about 15 Ma and continued episodically until about 6 Ma. Two periods, between ca. 15.0 to 12.6 Ma and ca. 9.9 to 8.0 Ma, coincide with maximal effusive output. At least 31 volcanic units were erupted from contiguous and coalesced eruptive centers; these include several trachyandesite stratovolcanoes and numerous silicic trachyandesite to rhyolite flow dome complexes. Most BHVF rocks are moderately porphyritic and contain 15–35 volume percent plagioclase, pyroxene, and hornblende±biotite phenocrysts. Mineral compositions indicate that the reservoirs responsible for BHVF magmatism formed at mid to shallow crustal levels (≤10-15 km) and most equilibrated at temperatures ranging from about 775 to 850°C.

Rocks in the BHVF have high-potassium calc-alkaline compositions, contain ~50 to 78 wt% SiO_2, and have pronounced negative Ti-Nb-Ta anomalies and other trace element characteristics consistent with origins associated with subduction-related continental margin arc magmatism. Importantly, BHVF rock compositions do not vary systematically in a temporal context. These temporally non-systematic compositional variations are consistent with development of many small, discrete, compositionally distinct reservoirs in a subduction-related context that did not yield magmas whose compositions varied systematically with time. Diagnostically, the lava-dome-forming rhyolites have significantly depleted middle to heavy REE abundances, likely a reflection of zircon and lesser titanite fractionation or residual zircon in the source region, relative to intermediate composition volcanic rocks of the BHVF.

BHVF rocks exhibit a wide range of radiogenic isotope ratios, and although most have isotopic compositions indicative of somewhat enriched, crustal components, some have compositions consistent with more depleted, mantle sources. Initial Sr and □Nd isotope values covary somewhat systematically but Pb isotope variations are uncorrelated with either. Similarly, isotopic variations among BHVF rocks are weakly correlated with age and composition.

Geochemical, isotopic, and petrographic data indicate that volcanic activity in the BHVF is a consequence of subduction-related, continental arc magmatism. Isotopic and P_2O_5-K_2O systematics among BHVF rocks indicate that some of the BHVF magmas evolved by crustal contamination of parental mafic melts. Trace element abundances, particularly elevated Sr, indicate that BHVF magmas were derived from partial melts generated beneath thick continental crust at mantle depths greater than about 70 km. Systematic major oxide variations are consistent with fractionation of observed phenocrysts, although moderate-magnitude negative Eu anomalies suggest, with the exception of the rhyolites, somewhat limited plagioclase fractionation. Distinct MREE depletions suggest that hornblende fractionation was important in the petrogenesis of essentially all BHVF rocks. However, lower MREE to HREE abundances diagnostic of the BHVF rhyolites probably reflect fractionation of zircon, not increased hornblende fractionation, because the magnitude of negative MREE anomalies among all rocks of the BHVF is essentially constant. Larger magnitude negative Eu anomalies characteristic of the BHVF rhyolites likely reflect greater plagioclase fractionation during petrogenesis of these rocks.

Textural and compositional features of phenocrysts in the BHVF rocks suggest that the associated reservoirs experienced significant open-system behavior, including complex crystallization histories, reservoir recharge events, mixing/mingling processes, and degassing. Highly variable compositions of many of the BHVF eruptive units also suggest recharge, incomplete reservoir homogenization, and variable crustal contamination. Considerable compositional variation among diverse but temporally equivalent eruptive products suggests that the BHVF evolved by development of numerous small, discrete, and compositionally distinct, reservoirs beneath closely spaced eruptive centers in the BHVF; many of these shallow magma bodies degassed between about 13 and 8 Ma, forming numerous alteration zones in the BHVF.

Quartz-adularia and quartz-alunite epithermal mineral deposits, from which ~3.4 Moz. of gold, ~28 Moz. of silver, and minor amounts of mercury were produced, are associated with BHVF magmatism (Fig. 15; Vikre et al., 2015). Mined quartz-adularia gold-silver vein deposits in the Bodie and Aurora districts consist of quartz, adularia, sericite, calcite, electrum, acanthite, and other sulfide and telluride minerals. Small mercury deposits at the Paramount mine and near Spring Peak occur in sinters and subjacent veins in Miocene volcaniclastic strata; gold-silver veins beneath the Spring Peak sinter are similar to veins in the Aurora district several kilometers to the north. Quartz-alunite gold-silver-copper deposits in the Masonic district, which occur in fault zones and disseminated in volcaniclastic strata, consist of quartz, alunite, kaolinite, pyrite, enargite, and numerous Cu-As-Sb-Fe-Bi-Au-Ag-S-Se-Te minerals. Other small ($\leq$2 km^2) to large (>30 km^2) quartz-alunite alteration zones, in which few economic concentrations of minerals have been found, include volcaniclastic rocks and lava flows that have been extensively replaced by quartz, alunite, and variable amounts of kaolinite, pyrite, pyrophyllite, sericite, and illite-montmorillonite. Small mercury deposits occur in several of these alteration zones, and the concealed Cinnabar Canyon sulfur resource (~16.1 Mt @ 17.9 percent S; Ward, 1992) was identified by drilling adjacent to a mercury mine.

Epithermal gold-silver deposits similar to those in the BHVF are very common in convergent continental margin arcs worldwide; they are especially common in association with lava dome complexes. In the BHVF, most quartz-adularia and quartz-alunite deposits and alteration zones are broadly contemporaneous with their volcanic host rocks, although some are somewhat younger, which suggests that the associated magmas provided heat, fluid, and metals required for deposit genesis. Development of two distinct epithermal deposit types reflects genesis under different thermochemical conditions. The mineral assemblages characteristic of the quartz-adularia systems are consistent with derivation from near-neutral fluids at ≤250 °C, whereas those of the quartz-alunite systems require more acidic, oxidized, sulfur-rich fluids at similar temperatures.

Acknowledgments

This work was funded by the USGS Mineral Resources Program. We gratefully acknowledge the insights and reviews by C.S. Holm-Denoma, W.C. Day, E.H. Christiansen, and C.J. Busby that helped improve this study. We thank Dan Stepner, Lizzy Ann Spencer, and Shuangquan Zhang for assistance in the IGGRC radiogenic isotope lab at Carleton. This is IGGRC contribution number 59. Finally, we thank C.N. Mercer, Associate Editor at American Mineralogist, for handling the review and editorial aspects of this submission so effectively. Any use of trade, product, or firm names is for descriptive purposes only and does not imply endorsement by the U.S. Government.

References cited

Al-Rawi, Y.T. (1969) Cenozoic history of the northern part of Mono Basin, California and Nevada. Berkeley, University of California, Ph.D. thesis, 163 p.

Anders, E., and Ebihara, M. (1982) Solar-system abundances of the elements. Geochimica et Cosmochimica Acta, 46, 2362-2380.

This is a preprint, the final version is subject to change, of the American Mineralogist (MSA)
Cite as Authors (Year) Title. American Mineralogist, in press.
(DOI will not work until issue is live.) DOI: http://dx.doi.org/10.2138/am-2016-5440 11/4

Atwater, T., and Stock, J. (1998) Pacific–North America plate tectonics of the Neogene southwestern United States—An update. International Geology Review, 40, 375-402.

Bacon, C.R., and Hirschmann, M.M. (1988) Mg/Mn partitioning as a test for equilibrium between co-existing Fe-Ti oxides. American Mineralogist, 73, 57-61.

Bailey, R.A. (2004) Eruptive history and chemical evolution of the precaldera and post-caldera basalt-dacite sequences, Long Valley, California: Implications for magma sources, current seismic unrest, and future volcanism. U.S. Geological Survey Professional Paper 1692, 75 p.

Barton, M.D. (1980) The Ag-Au-S system. Economic Geology, 75, 303-316.

Barton, P.B., and Skinner, B.J. (1979) Sulfide mineral stabilities *in*, Barnes, H.L., ed., Geochemistry of Hydrothermal Ore Deposits, second edition, John Wiley and Sons, New York, 278-403.

Beard, B.L., and Glazner, A.F. (1995) Trace element and Sr and Nd isotopic composition of mantle xenoliths from the Big Pine volcanic field, California. Journal of Geophysical Research, 100, 4169-4179.

Blakely, R.J., and Jachens, R.C. (1991) Regional study of mineral resources in Nevada: Insights from three dimensional analysis of gravity and magnetic anomalies. Geological Society of America Bulletin, 103, 795-803., doi: 10.1130/0016-7606(1991)103<0795:RSOMRI>2.3.CO;2.

Breit, F.J., Jr. (2000) Structural and temporal relationships and geochemical characteristics of the East Brawley Peak acid-sulfate prospect and the adjacent Aurora adularia-sericite system. Reno, University of Nevada, M.S. thesis, 215 p.

Brey, G.P., and Kohler, T. (1990) Geothermobarometry in four-phase lherzolites II. New thermobarometers, and practical assessment of existing thermobarometers. Journal of Petrology, 31, 1353-1378.

Busby, C.J. (2013) Birth of a plate boundary at ca. 12 Ma in the Ancestral Cascades arc, Walker Lane belt of California and Nevada. Geosphere, 9, 1147-1160, doi: 10.1130/GES00928.1.

Cameron, K.L., and Cameron, M. (1985) Rare earth element, $^{87}Sr/^{86}Sr$, and $^{143}Nd/^{144}Nd$ compositions of Cenozoic orogenic dacites from Baja California, northwestern Mexico, and adjacent west Texas; evidence for the predominance of a subcrustal component. Contributions to Mineralogy and Petrology, 91, 1-11.

Carlson, C.W., Pluhar, C.J., Glen, J.M.G., and Farner, M.J. (2013) Kinematics of the west-central Walker Lane: Spatially and temporally variable rotations evident in the late Miocene Stanislaus Group. Geosphere, 9, 1530-1551.

Chesterman, C.W. (1968) Volcanic geology of the Bodie Hills, Mono County, California, In R.R. Coats, R.L. Hay, and C.A. Anderson, Eds., Studies in volcanology. Geological Society of America Memoir 116, 45-68.

Chesterman, C.W., Chapman, R.H., and Gray, C.H., Jr. (1986) Geology and ore deposits of the Bodie mining district, Mono County, California. California Division of Mines and Geology Report 206, 36 p.

Chesterman, C.W., and Gray, C.H., Jr. (1975) Geology of the Bodie 15-minute quadrangle, Mono County, California. California Division of Mines and Geology, Map Sheet 21, scale 1:48,000.

Christensen, J.N. and DePaolo, D.J. (1993) Time scales of large volume silicic magma systems: Sr isotopic systematics of phenocrysts and glass from the Bishop Tuff, Long Valley, California. Contributions to Mineralogy and Petrology, 113, 100-114.

Christiansen, R.L., and Yeats, R.S. (1992) Post-Laramide geology of the U.S. Cordillera region, In B.C. Burchfiel, P.W. Lipman, and M.L. Zoback, Eds., The Cordilleran Orogen—Conterminous U.S. Boulder, Colo., Geological Society of America, The Geology of North America, G-3, 261-406.

Cousens B. (1996) Magmatic evolution of Quaternary mafic magmas at Long Valley Caldera and the Devils Postpile, California: effects of crustal contamination on lithospheric mantle-derived magmas. Journal of Geophysical Research, 101, 27673-27689.

Cousens, B.L., Henry, C.D., Harvey, B.J., Brownrigg, T., Prytulak, J. and Allan, J.F. (2011) Secular variations in magmatism during a continental arc to post-arc transition: Plio-Pleistocene volcanism in the Lake Tahoe/Truckee area, Northern Sierra Nevada, California. Lithos, 123, 225-242, doi: 10.1016/j.lithos.2010.09.009.

Cousens, B.L., Prytulak, Julie, Henry, C.D., Alcazar, Al, and Brownrigg, Tim (2008) Geology, geochronology, and geochemistry of the Miocene-Pliocene ancestral Cascades arc, northern Sierra Nevada, California and Nevada—The roles of the upper mantle, subducting slab, and the Sierra Nevada lithosphere. Geosphere, 4, 814-828.

Davidson, J., Turner, S., Handley, H., Macpherson, C., and Dosseto, A. (2007) Amphibole "sponge" in arc crust?. Geology, 35, 787-790.

du Bray, E.A., John, D.A., Box, S.E., Vikre, P.G., Fleck, R.J., and Cousens, B.L. (2013) Petrographic and geochemical data for Cenozoic volcanic rocks of the Bodie Hills, California and Nevada. U.S. Geological Survey Data Series 764, 10 p., http://pubs.usgs.gov/ds/764/.

du Bray, E.A., John, D.A., and Cousens, B.L. (2014) Petrologic, tectonic, and metallogenic evolution of the southern segment of the ancestral Cascades magmatic arc, California and Nevada. Geosphere, 10, 1-39.

du Bray, E.A., John, D.A., Putirka, K., and Cousens, B.L. (2009) Geochemical database for igneous rocks of the ancestral Cascades arc—Southern segment, California and Nevada. U.S. Geological Survey Digital Data Series 439, 1 CD-ROM.

Eaton, G.P., Wahl, R.R., Prostka, H.J., Mabey, D.R., and Kleinkopf, M.D. (1978) Regional gravity and tectonic patterns: Their relation to late Cenozoic epeirogeny and lateral spreading in the western Cordillera, In R.B. Smith, and G.P. Eaton, Eds., Cenozoic tectonics and regional geophysics of the Western Cordillera. Geological Society of America Memoir 152, 51-91.

Ewart, A. (1982) The mineralogy and petrology of Tertiary–Recent orogenic volcanic rocks with special reference to the andesitic-basaltic compositional range, In R.S. Thorpe, Ed., Andesites. New York, John Wiley and Sons, 25-87.

Farmer, G.L., Glazner, A.F., and Manley, C.R. (2002) Did lithospheric delamination trigger late Cenozoic potassic volcanism in the southern Sierra Nevada, California?. Bulletin of the Geological Society of America, 114, 754-768.

Faulds, J.E., and Henry, C.D. (2008) Tectonic influences on the spatial and temporal evolution of the Walker Lane: An incipient transform fault along the evolving Pacific-North American plate boundary, In J.E. Spencer, and S.R. Titley, Eds., Ores and orogenesis: Circum-Pacific tectonics, geologic evolution, and ore deposits. Arizona Geological Society Digest 22, 437-470.

Feeley, T.C., and Davidson, J.P. (1994) Petrology of calcalkaline lavas at Volcán Ollagüe and the origin of compositional diversity at central Andean stratovolcanoes. Journal of Petrology, 35, 1295-1340.

Feldstein, S.N., and Lange, R.A. (1999) Pliocene potassic magma from the Kings River region, Sierra Nevada, California; evidence for melting of a subduction-modified mantle. Journal of Petrology, 40, 1301-1320.

Fleck, R.J., du Bray, E.A., John, D.A., Vikre, P.G., Cosca, M.A., Snee, L.W., and Box, S.E. (2015) Geochronology of Cenozoic rocks in the Bodie Hills, California and Nevada. U.S. Geological Survey Data Series 916, 26 p.

Frost, B.R., Barnes, C.G., Collins, W.J., Arculus, R.J., Ellis, D.J., and Frost, C.D. (2001) A geochemical classification for granitic rocks. Journal of Petrology, 42, 2033-2048.

GEOROC (2010) Geochemistry of rocks of the oceans and continents. Max Plank Institut für Chemie, http://georoc.mpch-mainz.gwdg.de/georoc/.

Ghiorso, M.S., and Evans, B.W (2008) Thermodynamics of rhombohedral oxide solid solutions and a revision of the Fe-Ti two-oxide geothermometer and oxygen-barometer. American Journal of Science, 308, 957-1039.

Gilbert, C.M., Christiansen, M.N., Al-Rawi, Y., and Lajoie, K.R. (1968) Structural and volcanic history of Mono Basin, California-Nevada, In R.R. Coats, R.L. Hay, and C.A. Anderson, Eds., Studies in Volcanology. Geological Society of America Memoir 116, 275-329.

Gill, J. (1981) Orogenic Andesites and Plate Tectonics. New York, Springer-Verlag, 390 p.

Green, T.H. (1982) Anatexis of mafic crust and high pressure crystallization of andesite, In R.S. Thorpe, Ed., Andesites. New York, John Wiley and Sons, 465-487.

Halliday, A.N., Mahood, G.A., Holden, P., Metz, J.M., Dempster, T.J., and Davidson, J.P. (1989) Evidence for long residence times of rhyolitic magma in the Long Valley magmatic system: the isotopic record in precaldera lavas of Glass Mountain. Earth and Planetary Science Letters, 94, 274-290.

Hawkesworth, C., Turner, S., Gallagher, K., Hunter, A., Bradshaw, T., and Rogers, N. (1995) Calc-alkaline magmatism, lithospheric thinning and extension in the Basin and Range. Journal of Geophysical Research, 100, 10,271-10,286.

Hayden, L.A., Watson, E.B, and Wark, D.A. (2008) A thermobarometer for sphene (titanite). Contributions to Mineralogy and Petrology, 155, 529-540.

Herrera, P.A., Closs, L.G., and Silberman, M.L. (1993) Alteration and geochemical zoning in Bodie Bluff, Bodie mining district, California. Journal of Geochemical Exploration, 48, 259-275, doi: 10.1016/0375-6742 (93)90007-9.

Herrera, P.A., Silberman, M.L., and Closs, L.G. (1991) Alteration mineral assemblage and trace element zoning at Bodie Bluff, northern part of the Bodie mining district, Mono County, California, In G.L. Raines, R.F. Lisle, R.W. Schafer, and W.H. Wilkinson, Eds., Geology and ore deposits of the Great Basin. Reno, Geological Society of Nevada Symposium Proceedings, 1189-1193.

Hildreth, W., and Moorbath, S. (1988) Crustal contributions to arc magmatism in the Andes of central Chile. Contributions to Mineralogy and Petrology, 98, 455-489.

Hill, J.M. (1915) Some mining districts in northeastern California and northwestern Nevada. U.S. Geological Survey Bulletin 594, 200 p.

Holland, T., and Blundy, J., 1994, Non-ideal interactions in calcic amphiboles and their bearing on amphibole-plagioclase thermometry: Contributions to Mineralogy and Petrology, 116, 433-447.

Irvine, T.N., and Baragar, W.R.A. (1971) A guide to the chemical classification of the common volcanic rocks. Canadian Journal of Earth Sciences, 8, 523-548.

John, D.A. (2001) Miocene and early Pliocene epithermal gold-silver deposits in the northern Great Basin, Western United States—Characteristics, distribution, and relationship to magmatism. Economic Geology, 96, 1827-1853.

John, D.A., du Bray, E.A., Blakely, R.J., Fleck, R.J., Vikre, P.G., Box, S.E., and Moring, B.C. (2012) Miocene magmatism in the Bodie Hills volcanic field, California and Nevada—A long-lived eruptive center in the southern segment of the ancestral Cascades arc. Geosphere, 8, 44-97.

John, D.A., du Bray, E.A., Box, S.E., Vikre, P.G., Rytuba, J.J., Fleck, R.J., Moring, B.C. (2015) Geologic map of the Bodie Hills, California and Nevada. U.S. Geological Survey Scientific Investigations Map SIM-3318, scale 1:50,000, 64 p.

Kelleher, P.C., and Cameron, K.L. (1990) The geochemistry of the Mono Craters-Mono Lake Islands volcanic complex, eastern California. Journal of Geophysical Research, 95, 17643-17660.

Kinetic Gold website. http://www.kineticgold.com/s/SpringPeak.asp, accessed 1/21/2015

Kingdon, S., Cousens, B., John, D.A., and du Bray, E.A. (2013) Pliocene to late Pleistocene magmatism in the Aurora Volcanic Field, Nevada and California, USA. Eos Transactions AGU V13G-2700.

Kingdon, S.A., Cousens, B.L., John, D.A., and du Bray, E.A (2014) Pliocene to late Pleistocene magmatism in the Aurora Volcanic Field, Basin and Range province, Nevada and California, USA. Geological Association of Canada-Mineralogical Association of Canada Joint Annual Meeting Abstracts, 37, 139-140.

Kistler, R.W. (1990) Two different lithosphere types in the Sierra Nevada, California, In J.L. Anderson, Ed., The nature and origin of Cordilleran metamorphism. Geological Society of America Memoir 174, 271-281.

Kistler, R.W., and Peterman, Z.E. (1978) Reconstruction of crustal blocks of California on the basis of initial strontium isotopic compositions of Mesozoic granite rocks. U.S. Geological Survey Professional Paper 1071, 17 p.

Kleinhampl, F.J., Davis, W.E., Silberman, M.L., Chesterman, C.W., Chapman, R.H., and Gray, C.H., Jr. (1975) Aeromagnetic and limited gravity studies and generalized geology of the Bodie Hills region, Nevada and California. U.S. Geological Survey Bulletin 1384, 38 p.

Knudsen, P., and Prenn, N. (2002) Technical report on the Esmeralda Project, Mineral County, Nevada USA. Mine Development Associates, 121 p., available at http://www.secinfo.com/dVut2.215aw.htm.

Lange, R.A., and Carmichael, I.S.E. (1996) The Aurora volcanic field, California-Nevada: Oxygen fugacity constraints on the development of andesitic magma. Contributions to Mineralogy and Petrology, 125, 167-185.

Lange, R.A., Carmichael, I.S.E., and Renne, P. (1993) Potassic volcanism near Mono Basin, California: Evidence for high water and oxygen fugacities inherited from subduction. Geology, 21, 949-952.

Le Maitre, R.W. (1989) A classification of igneous rocks and glossary of terms. Oxford, UK, Blackwell Scientific, 193 p.

Ludington, Steve, Cox, D.P., Leonard, K.R., and Moring, B.C. (1996) Cenozoic volcanic geology of Nevada. Nevada Bureau of Mines and Geology Open-File Report 96-2, 5-1 to 5-10.

Metz, J.M., and Mahood, G.A. (1985) Precursors to the Bishop Tuff eruption: Glass Mountain, Long Valley, California. Journal of Geophysical Research, 90, 11121-11126.

Oldow, J.S. (1992) Late Cenozoic displacement partitioning in the northwestern Great Basin. Reno, Geological Society of Nevada, Structure, Tectonics and Mineralization of the Walker Lane Symposium, April 24, 1992, Reno, Proceedings, 17-52.

Oldow, J.S. (2003) Active transtensional boundary zone between the western Great Basin and Sierra Nevada block, western U.S. Cordillera, Geology, 31, 1033-1036.

Ormerod, D.S., Rogers, N.W., and Hawkesworth, C.J. (1991) Melting in the lithospheric mantle: inverse modeling of alkali-olivine basalts from the Big Pine Volcanic Field, California. Contributions to Mineralogy and Petrology, 108, 305-317.

Osborne, M.A. (1985) Alteration and mineralization of the northern half of the Aurora mining district, Mineral County, Nevada. Reno, University of Nevada, MS thesis, 93 p.

Osborne, M.A. (1991) Epithermal mineralization at Aurora, Nevada, In G.L. Raines, R.F. Lisle, R.W. Schafer, and W.H. Wilkinson, Eds. Geology and ore deposits of the Great Basin, Geological Society of Nevada, Symposium Proceedings, Reno, Nevada, 1097-1110.

Pearce, J.A., Harris, N.B.W., and Tindle, A.G. (1984) Trace element discrimination diagrams for the tectonic interpretation of granitic rocks. Journal of Petrology, 25, 956-983.

Pearce, J.A., and Peate, D.W. (1995) Tectonic implications of the composition of volcanic arc magmas. Annual Review of Earth and Planetary Sciences, 23, 251-285.

Putirka, K.D. (2008) Thermometers and barometers for volcanic systems. Reviews in Mineralogy and Geochemistry, 69, 61-120.

Putirka, Keith, and Busby, C.J. (2007) The tectonic significance of high-K_2O volcanism in the Sierra Nevada, California. Geology, 35, 923-926.

Putirka, Keith, Jean, Marlon, Cousens, Brian, Sharma, Rohit, Torrez, Gerardo, and Carlson, Chad (2012) Cenozoic volcanism in the Sierra Nevada and Walker Lane, California, and a new model for lithosphere degradation. Geosphere, 8, 265-291.

Richards, J.P., and Kerrich, R., 2007, Adakite-like rocks: their diverse origins and questionable role in metallogenesis: Economic Geology, 102, 537–576.

Robinson, A.C., and Kistler, R.W. (1986) Maps showing isotopic dating in the Walker Lake 1° by 2° quadrangle, California and Nevada. U.S. Geological Survey Miscellaneous Field Studies Map MF-1382-N, scale 1:250,000.

Rockwell, B.W. (2010) Mineral and vegetation maps of the Bodie Hills, Brawley Peaks, Sweetwater Mountains, and Wassuk Range, California/Nevada, generated from ASTER satellite data. U.S. Geological Survey Scientific Investigations Map 3104, scale 1:62,000, 5 p., http://pubs.usgs.gov/sim/3104/.

Romberger, S.B. (1991a) Transport and deposition of precious metals in epithermal deposits, In G.L. Raines, R.E. Lisle, R.W. Schafer, and W.H. Wilkinson, Eds., Geology and ore deposits of the Great Basin Symposium Proceedings. Geological Society of Nevada, 219-232.

Romberger, S.B. (1991b) A model for bonanza gold deposits, In P.A. Sheahan and M.E. Cherry, Eds., Ore Deposit Models volume II. Geoscience Canada, Reprint Series 6, 77-86.

Rutherford, M.J., and Hill, P.M. (1993) Magma ascent rates from amphibole breakdown; an experimental study applied to the 1980-1986 Mount St. Helens eruptions. Journal of Geophysical Research, 98, 19,667-19,685.

Saltus, R.W., and Jachens, R.C. (1995) Gravity and basin depth maps of the Basin and Range province, western United States. U.S. Geological Survey Geophysical Investigations Map GP-1012, 1 sheet.

Schmidt, M.E., Grunder, A.L., and Rowe, M.C. (2008) Segmentation of the Cascade arc as indicated by Sr and Nd isotopic variation among diverse primitive basalts. Earth and Planetary Science Letters, 266, 166-181.

Scott, S.D., and Barnes, H.L. (1971) Sphalerite geothermometry and geobarometry. Economic Geology, 66, 653-669.

Shand, S.J. (1951) Eruptive Rocks. New York, John Wiley, 488 p.

Silberman, M.L., and Chesterman, C.W. (1991) A description of the Bodie Hills and Bodie mining district, Mono county, California with annotated road log from Bridgeport to Bodie, In R.H. Buffa, and A.R. Coyner, Eds., Geology and ore deposits of the Great Basin: Field Trip Guidebook Compendium, Volume 2. Reno, Geological Society of Nevada, 601-618.

Sisson, T.W., 1994, Hornblende-melt trace-element partitioning measured by ion microprobe: Chemical Geology, 117, 331–344.

Smailbegovic, A. (2002) Structural and lithologic constraints to mineralization in Aurora, NV and Bodie, CA mining districts, observed and interpreted with aerospace geophysical data. Reno, University of Nevada, Ph.D. thesis, 261 p.

Stewart, J.H. (1988) Tectonics of the Walker Lane Belt, western Great Basin; Mesozoic and Cenozoic deformation in a zone of shear, In W.G. Ernst, Ed., Metamorphism and crustal evolution of the Western United States. Englewood Cliffs, N.J., Prentice Hall, Rubey Volume VII, 683-713.

Stewart, J.H., Carlson, J.E., and Johannsen, D.C. (1982) Geologic map of the Walker Lake 1° x 2° quadrangle, California and Nevada. U.S. Geological Survey Miscellaneous Field Studies Map MF-1382-A, scale 1:250,000.

Sun, S.-S., and McDonough, W.F. (1989) Chemical and isotopic systematics of oceanic basalts; implications for mantle composition and processes, In A.D. Saunders and M.J. Norry, Eds., Magmatism in the ocean basins. Geological Society of London Special Publication 42, 313-345.

Taggart, J.E., Jr. (2002) Analytical methods for chemical analysis of geologic and other materials. U.S. Geological Survey Open-File Report 02-223, http://pubs.usgs.gov/of/2002/ofr-02-0223/OFR-02-0223.pdf.

Todt, W., Cliff, R.A., Hanser, A., and Hofmann, A.W. (1996) Evaluation of a ^{202}Pb-^{205}Pb double spike for high-precision lead isotope analysis, In A. Basu, and S.R. Hart, Eds., Earth Processes-Reading the Isotopic Code. Geophysical Monograph 95. Washington, DC: American Geophysical Union, 429-437.

Tosdal, R.M., Wooden, J.L., and Kistler, R.W. (2000) Inheritance of Nevadan mineral belts from Neoproterozoic continental breakup, In J.K. Cluer, J.G. Price, E.M. Struhsacker, R.F. Hardyman, and C.L. Morris, Eds., Geology and ore deposits 2000—The Great Basin and beyond. Geological Society of Nevada Symposium Proceedings, May 15–18, 2000, 451-466.

Trail, D., Hayden, L.A., Watson, E.B., and Tailby, N.D. (2012) Major element incorporation into apatite; implications for thermometery. Mineralogical Magazine, 76, 2466.

Vikre, P.G., and Henry, C.D. (2011) Quartz-alunite alteration cells in the ancestral southern Cascade magmatic arc, In R. Steininger, and B. Pennell., Eds., Great Basin evolution and metallogeny. Reno, Geological Society of Nevada, 2010 Symposium proceedings, 701-745.

Vikre, P.G., John, D.A., du Bray, E.A., and Fleck, R.J., 2015, Gold-silver mining districts and alteration zones in the Miocene Bodie Hills volcanic field, California and Nevada. U.S. Geological Survey Scientific Investigations Report SIR-5012, YYY p.

Wark, D.A. (1991) Oligocene ash flow volcanism, northern Sierra Madre Occidental; role of mafic and intermediate-composition magmas in rhyolite genesis. Journal of Geophysical Research, 96, 13,389-13,411.

Ward, J.M. (1992) The Cinnabar Canyon sulfur deposit, In G.R. Wessel and B.H. Wimberly, Eds., Native Sulfur Developments in Geology and Exploration. Society for Mining, Metallurgy, and Exploration, Inc., 159-164.

Watson, E.B. (1979) Zircon saturation in felsic liquids; experimental results and applications to trace element geochemistry. Contributions to Mineralogy and Petrology, 70, 407-419.

Wesnousky, S.G. (2005) Active faulting in the Walker Lane. Tectonics, 24, 35 p., DOI 10.1029/2004TC001645.

Wood, D.A., Joron, J.L., and Treuil, M. (1979) A re-appraisal of the use of trace elements to classify and discriminate between magma series erupted in different tectonic settings. Earth and Planetary Science Letters, 45, 326-336.

Figure 1. Location map showing regional geologic setting of the Bodie Hills and major physiographic features. Mina deflection and outline of the Walker Lane modified from Faulds and Henry (2008), Busby (2013), and Carlson et al. (2013). Red dashed line is the initial $^{87}Sr/^{86}Sr$ = 0.706 isopleth for Mesozoic plutonic rocks in California (Kistler, 1990) and Nevada (Tosdal et al., 2000). Blue dashed line is the $^{208}Pb/^{204}Pb$ = 38.8 isopleth for Mesozoic plutonic rocks in Nevada (Tosdal et al., 2000). Yellow box shows outline of Figure 2.

Figure 2. Simplified geologic map of the Miocene Bodie Hills volcanic field showing the distribution of its eruptive centers (EC) (modified from John et al., 2012 , 2015).

Figure 3. Histogram showing areas (km^2) of Miocene Bodie Hills volcanic field eruptive rocks versus preferred age (Ma). Areas derived from geologic map of the Bodie Hills (John et al., 2015). Ages derived from age data summarized by Fleck et al. (2015).

Figure 4. Photomicrographs showing characteristic features of Miocene Bodie Hills volcanic field rocks. As depicted in these images, all Bodie Hills volcanic field rocks are porphyritic and contain phenocrysts in a variably devitrified groundmass. (A) Oscillatory zoned plagioclase (sample 203178, dacite of Silver Hill), crossed polarizers. (B) Sieve-textured plagioclase (sample 203164, trachyandesite of Mount Biedeman), crossed polarizers. (C) Partly resorbed plagioclase (sample 203245, trachyandesite of West Brawley Peak), plane-polarized light. (D) Moderately well-developed opacite rims on hornblende (sample 203201, trachyandesite of Masonic), plane-polarized light.

Figure 5. Total alkali-silica variation diagram showing compositions of Miocene volcanic rocks of the Bodie Hills volcanic field. Field boundaries from Le Maitre (1989). Alkaline-subalkaline dividing line is from Irvine and Baragar (1971).

Figure 6. Variation diagrams showing abundances of major oxides (wt%) in Miocene volcanic rocks of the Bodie Hills volcanic field. Field boundaries on K_2O versus SiO_2 diagram from Le Maitre (1989); high K-shoshonitic dividing line from Ewart (1982). Red lines indicate possible fractionation trends.

Figure 7. Diagram showing the variation of average SiO_2 content for each of the Miocene volcanic rock units of the Bodie Hills volcanic field relative to unit ages.

Figure 8. Compositional variation within Miocene volcanic rock units of the Bodie Hills volcanic field. Units (vertical axis) are arranged according to age, with data for the units arranged from youngest (top) to oldest (bottom). Unit abbreviations are: BA, rhyolite of Big Alkali; HS, dacite of Hot Springs Canyon; WS, trachyandesite of Willow Springs; CI, trachydacite of Cinnabar Canyon; PP, trachydacite of Potato Peak; SH, dacite of Silver Hill; MB, trachyandesite of Mount Biedeman; BP; rhyolite of Bald Peak; BH, rhyolite of Bodie Hills; BC, rhyolite of Bodie Creek; TA, trachyandesite of Aurora Canyon; RS, rhyolite of Rock Springs Canyon; DM, trachyandesite of Del Monte; BR, trachydacite of Bridgeport Canyon; PR, pyroxene rhyolite; EB, rhyolite of east Brawley; AC, rhyolite of Aurora Creek; DC, rhyolite of Del Monte Canyon; TI, trachydacite intrusion; CC, trachyandesite of Clark Canyon; WB, trachyandesite of West Brawley Peak; RA, basaltic trachyandesite of Rancheria; HT, hornblende trachyandesite; RC, trachydacite of Rough Creek; LS, andesite of Lakeview Spring; AU, trachyandesite of Aurora; MG, trachyandesite of Masonic Gulch; EC, trachydacite of East Canyon; SC, trachyandesite of Sinnamon Cut; MS, trachyandesite of Mud Springs Canyon; and MA, trachyandesite of Masonic. Major oxide data (recalculated to 100 wt%, on a volatile free basis) in wt%; trace element data in parts per million.

Figure 9. Average chondrite-normalized rare earth element diagrams for rock units of the Bodie Hills volcanic field. Chondrite abundances from Anders and Ebihara (1982). Patterns for BHVF rhyolites are in red, whereas those for all intermediate-composition units, which have distinct REE patterns, are in green. Dashed lines represent the four most primitive (49.9 to 52.0 wt% SiO_2) BHVF field rocks; these samples of the basaltic trachyandesite of Rancheria are thought to best define compositions of parental magmas from which magmas erupted as part of the BHVF were derived.

Figure 10. Primitive mantle-normalized (Sun and McDonough, 1989) trace element diagrams for volcanic rock units of the Bodie Hills volcanic field. Patterns for BHVF rhyolites are in red, whereas those for all intermediate-composition units, which have distinctive trace element

abundances, are in green. Dashed lines represent the four most primitive (49.9 to 52.0 wt% SiO_2) BHVF field rocks; these samples of the basaltic trachyandesite of Rancheria are thought to best define compositions of parental magmas from which magmas erupted as part of the BHVF were derived.

Figure 11. Radiogenic isotope diagrams for Bodie Hills volcanic field rocks. All plotted data represent age-corrected initial values for individual samples. Gray squares depict samples from volcanic centers (Lassen Peak to Lake Tahoe region; Cousens et al., 2008; and unpublished data) in the southern segment of the ancestral Cascades arc. (A) ε_{Nd}^{T} versus $^{87}Sr/^{86}Sr_{initial}$. Dashed line delimits the compositional field of samples from the Central Sierra Nevada volcanic field (Putirka et al., 2012) for which Pb data are unavailable. (B) $^{208}Pb/^{204}Pb$ versus $^{206}Pb/^{204}Pb$. (C) $^{87}Sr/^{86}Sr_{initial}$ versus $^{206}Pb/^{204}Pb$.

Figure 12. Initial $^{87}Sr/^{86}Sr$ versus age variation diagram for individual samples of Bodie Hills volcanic field rocks, grouped by composition.

Figure 13. Initial isotopic ratio versus chemical composition diagrams for individual samples of Bodie Hills volcanic field rocks. (A) $^{87}Sr/^{86}Sr$ versus SiO_2. (B) $^{206}Pb/^{204}Pb$ versus SiO_2.

Figure 14. Geologic map of the Bodie Hills volcanic field (John et al., 2012) showing mining districts (line pattern) and alteration zones (crosshatch pattern), with commodity produced or resource in parentheses.

Figure 15. Age ranges of volcanic rocks and hydrothermal minerals in the Masonic (Au, Ag, Cu), Aurora (Au, Ag), and Bodie (Au, Ag) mining districts, and in quartz-alunite alteration zones of the Bodie Hills volcanic field, based on $^{40}Ar/^{39}Ar$ dates of plagioclase, sanidine, hornblende, biotite, alunite, and adularia. Rectangles enclose geographic groups of hydrothermally altered host volcanic rocks and hydrothermal minerals within districts and alteration zones, and include unaltered rocks that are associated in space and time with altered and mineralized rocks. Dash and solid black brackets represent ranges of dates (and analytic errors) of altered and unaltered rocks, respectively; red and blue brackets represent ranges of dates (and analytic errors) of

alunite and adularia, respectively. Volcanic rock names are from John et al. (2012) and mineral dates are from Fleck et al. (2015).

Figure 16. Approximate stability fields of hydrothermal mineral assemblages in Masonic district Au-Ag-Cu deposits and Bodie and Aurora district Au-Ag deposits based on experimentally determined mineral equilibria relative to (A) fluid pH and oxygen fugacity (log f O_2) at 250°C and (B) fluid temperature (°C) and sulfur fugacity (log f S_2). Fields are constrained by observed mineral assemblages, temperatures estimated from fluid inclusion microthermometry and calculated sulfide-sulfate sulfur isotope equilibrium temperatures, and measured electrum and sphalerite compositions (electron microprobe and scanning electron microscope analyses, summarized in Vikre and Henry (2011) and Vikre et al. (2015)). Electrum (X_{Ag}, short dash lines), sphalerite (X_{FeS}, long dash lines) and other mineral equilibria (extrapolated below 300°C) are from Barton and Toulmin (1966), Scott and Barnes (1971), Barton and Skinner (1979), Barton (1980), and Romberger (1991a).

Figure 17. Trace-element, tectonic setting–discrimination variation diagram showing the composition of Bodie Hills volcanic field eruptive products. Tectonic setting-composition boundaries from Pearce et al. (1984).

Figure 18. Initial isotopic ratio versus chemical composition diagrams for individual samples of Bodie Hills volcanic field rocks. (A) $^{206}Pb/^{204}Pb$ versus 1/Pb. (B) $^{206}Pb/^{204}Pb$ versus Pb/Ce. (C) $^{143}Nd/^{144}Nd$ versus 1/Nd. (D) $^{87}Sr/^{86}Sr$ versus 1/Sr. (E) $^{87}Sr/^{86}Sr$ versus Rb/Sr. (F) $^{87}Sr/^{86}Sr$ versus Pb/Ce. Note log scale for 1/Sr and Rb/Sr in (D) and (E).

Figure 19. Initial $^{87}Sr/^{86}Sr$ versus SiO_2 variation diagram showing compositions of Bodie Hills volcanic field rocks relative to those of other Neogene and Quaternary volcanic rocks in the region surrounding the Bodie Hills. Sources of data: ancestral Cascades arc (Tahoe), Cousens et al. (2008); ancestral Cascades arc (Central Sierra Nevada volcanic field), Putirka et al. (2012); Post-arc (Tahoe), Cousens et al. (2011); Glass Mountain, Metz and Mahood (1985), Halliday et al. (1989); Long Valley (mafic), Cousens (1996), Bailey (2004); Mono Domes, Kelleher and Cameron (1990); Black Point, Ormerod et al. (1991), Cousens (1996); Big Pine, Ormerod

(1991), Beard and Glazner (1995); Bodie Hills volcanic field rocks, this paper; Bishop Tuff, Christensen and DePaolo (1993).

Table 1. Characteristic features of eruptive centers and units in the Bodie Hills volcanic field

Eruptive Center/Unit	*Volcanic landform*	*Eruptive products*	*Composition*	*Average SiO_2 content (wt%)*	*Area/dimensions*	*Age range and preferred age (Ma)[1]*	*Notable Features*
Masonic	Stratovolcano	Lava flows, debris-flow deposits, volcaniclastic sedimentary rocks, plugs and domes, minor block-and-ash-flow deposits	Trachyandesite and basaltic trachyandesite; with minor basaltic andesite and dacite	59.7	145 km^2 exposed area; inferred total area >200 km^2; circular, ~16-18 km diameter	15.00 to 14.07 14.70	E-W-trending horst of Mesozoic rocks bifurcates unit; debris-flow deposits and volcaniclastic rocks more abundant near margins of unit's distribution; late domes concentrated on north side of Masonic Mountain and include trachyandesite of Lakeview
Mud Springs Canyon	Domes	Lava domes	Trachyandesite	60.7	8.5 km^2; 1 x 8 km elongated east-west	13.87 13.87	Series of domes and thick lava flows
Sinnamon Cut	Intrusions	Hypabyssal intrusions and lava flows(?)	Trachyandesite	60.6	0.5 km^2; 2 bodies each 0.3 x 0.8 km	13.7 13.7	Hornblende-rich, platy jointed
East Canyon	Domes	Lava domes	Trachydacite and trachyandesite	64.2	3 km^2, largest body ~3 x 1 km	13.78 13.78	Abundantly porphyritic lava domes
Masonic Gulch	Domes	Lava domes	Trachyandesite	61.2	~2.2 km^2; largest dome 0.6-1.2 x 2 km	13.50 to 13.44 13.47	Three domes
Aurora	Stratovolcano(?)	Lava flows, debris-flow and block-and-ash-flow deposits, small shallow intrusions, minor volcaniclastic sedimentary rocks	Trachyandesite with minor andesite	59.8	~20 km^2; 2-4 x 8 km but largely covered by younger rocks	13.05 to 12.58 12.89	Hydrothermally altered in most places
Lakeview Spring	Domes	Lava domes, lava flows	Andesite	60.9	0.35 km^2; largest dome 0.3 x 1 km	12.93 12.93	Domes postdate adjacent hydrothermal alteration in the Masonic mining district
Rough Creek	Domes	Lava domes, carapace breccias, and minor block-and-ash-flow deposits	Trachydacite and trachyandesite	62.8	>20 km^2, largest mass ~4 x 4 km, extensive cover by younger deposits	12.95 to 11.68 12.87	Abundantly and coarsely porphyritic, northwest elongated lava domes; unconformably overlie hydrothermally altered Masonic center rocks

Hornblende trachyandesite intrusions	Intrusions	Small plugs	Trachyandesite	58.5	0.2 km^2; largest plug 0.3 x 0.3 km	11.8 11.8	Hornblende-rich
Rancheria	Unknown	Lava flows, small plug	Basaltic trachyandesite	53.7	~5 km^2; largest exposure about 1.5 x 2.3 km; extensive cover by younger deposits	11.7 to 11.6 11.7	Olivine-rich
West Brawley Peak	Stratovolcano	Central plug, lava flows and breccias	Trachyandesite, andesite, and trachydacite	62.2	~16 km^2 exposed area; semi-circle ~3-4 km in diameter with flow lobe extending 2 km farther south; southwest part covered by younger rocks	11.51 to 11.32 11.42	Outward dipping lava flows and flow breccias on south, west and north sides of plug forming West Brawley Peak; buttress unconformity with hydrothermally altered Aurora center rocks forming East Brawley Peak
Clark Canyon	Intrusions	Small plugs, lava flow	Trachyandesite	61.7	0.4 km^2	11.34 to 11.27 11.31	Series of 7 east-northeast aligned plugs and small volume lava flow
Trachydacite intrusions	Domes	Small plugs and domes	Trachydacite	66.8	0.4 km^2; 5 exposures; 0.5 km in diameter Dome Hill largest body	11.27 to 11.16 11.21	Biotite-rich
Del Monte Canyon	Domes	Lava flows and pyroclastic rocks	Rhyolite	73.5	3 km^2; ~1 x 3 km	11.50 to 11.19 11.16	North-dipping sequence of coarsely porphyritic lava flows and underlying lithic tuffs that flowed down Del Monte Canyon
Aurora Creek	Domes	Lava domes, carapace breccias, lava flows, and lithic-rich tuffs	Rhyolite	75.9	10 km^2; L-shaped, 4 km, north-south, 5 km east-west, ~1 km wide	11.18 11.18	Nearly aphyric, sparse phenocrysts
East Brawley Peak	Domes	Small domes and lava flows	Rhyolite	74.8	0.5 km^2; three masses, largest 0.2-0.5 x 1 km	11.18 11.18	Small domes intrusive into Aurora and West Brawley Peak centers
Pyroxene rhyolite	Domes	Lava domes	Rhyolite	70.4	0.25 km^2; 4 exposures, largest 0.1 x 0.8 km	11.15 11.15	Small lava domes north of Bald Peak

Bridgeport Canyon	Domes	Lava flows and domes	Trachydacite	63.2	0.9 km^2; several lava domes largely covered by younger deposits	11.08 to 11.07 11.08	Small domes and associated lava flows locally erupted onto Paleozoic basement rocks
Del Monte	Unknown	Lava flows, flow breccias, debris-flow deposits, volcaniclastic sedimentary rocks	Basaltic trachyandesite, trachyandesite, and trachydacite	61.2	~26 km^2 exposed in four main masses separated by younger rocks	10.98 to 10.94 10.96	Northern and central masses: lava flows, flow breccias, debris-flow deposits, and possible vent in Rough Creek; southern masses: interbedded lava flows, debris-flow deposits, sedimentary rocks; unit filled paleotopography (ancestral Bodie Creek)
Aurora Canyon	Domes	Lava domes, carapace breccias, and minor block-and-ash-flow deposits	Trachyandesite and trachydacite	62.1	~7 km^2, largest body ~1 x 5 km	10.58 to 10.27 10.42	Abundantly porphyritic lava domes form east-northeast elongate outcrop pattern
Bodie Creek	Domes	Domes and lava flows	Rhyolite	72.3	2.1 km^2; 4 small domes, largest ~1 x 1.5 km	11.34 to 9.89 10.01	Erosional domes largely covered by Pliocene-Pleistocene lava flows
Bodie Hills	Domes	Lava domes and minor pyroclastic rocks	Rhyolite and minor dacite	74.0	~8 km^2; largest body ~2 x 2 km; extensive cover by younger rocks	9.89 to 9.74 9.79	Porphyritic rhyolite domes partly surround Mount Biedeman stratovolcano and extend 15 km to northwest; includes several outcrops of rhyolite with mingled hornblende andesite blobs
Bald Peak-Paramount	Domes	Lava domes and carapace breccia (Bald Peak), lithic-rich tuff and volcaniclastic sedimentary rocks (Paramount basin)	Rhyolite	76.8	Bald Peak: 6.5 km^2; dome ~2.5 x 3 km; Paramount basin: ~20 km^2, 2-3 x 8 km; extensive younger cover	9.69 to 9.65 9.67	North-northeast elongated, nearly aphyric rhyolite domes surrounded by cogenetic lithic tuffs and volcaniclastic sedimentary rocks mostly deposited in shallow northeast-elongated basin to southwest of domes
Mount Biedeman	Stratovolcano	Lava flows, debris-flow deposits, intrusions, and minor block-and-ash-flow deposits	Trachyandesite and basaltic trachyandesite with minor basalt and dacite	59.3	~100 km^2 exposed area; extensive younger cover. circular ~5-6 km diameter volcano, debris-flow deposit aprons extend 3 to 15 km radially	9.95 to 8.90 9.27	Central intrusion forming Mount Biedeman surrounded by outward dipping lava flows and more distal debris-flow deposits and volcaniclastic sedimentary rocks

Silver Hill	Domes	Lava domes, carapace breccias, block-and-ash-flow and debris-flow deposits, volcaniclastic sedimentary rocks	Dacite, trachydacite, andesite, and trachyandesite	64.1	~45 km^2 exposed area with extensive younger cover; circular field ~7-8 km in diameter	9.14 to 8.93 9.07	Host rock for Bodie Au-Ag deposits
Potato Peak	Domes	Lava domes, lava flows and flow breccias, block-and-ash-flow and debris-flow deposits	Trachydacite and trachyandesite	63.0	~80 km^2; 3-8 x 14 km with ~3 x 6 km debris-flow deposit apron on south side	9.06 to 8.74 8.92	Thick sequences of lava flows with rubbly flow tops and fronts forming prominent flow lobes on west, north, and east sides; flow banded intrusions exposed on south side
Cinnabar Canyon	Domes	Lava flows and flow breccias	Trachydacite and rhyolite	68.1	0.3 km^2	8.55 8.55	Three small exposures north of Clearwater Creek beneath debris-flow deposits associated with the Mount Biedeman stratovolcano
Willow Springs	Domes	Lava domes, lava flows, minor flow breccias	Trachydacite and trachyandesite	61.9	~60 km^2 exposed area; ~9 x 12 km with extensive younger cover	8.58 to 8.00 8.17	Coarsely porphyritic lava flows and lava domes
Hot Springs Canyon	Domes	Lava domes	Dacite	65.1	0.5 km^2; largest exposure ~0.5 x 1 km	8.07 8.07	Small intrusions and associated flows emplaced into Willow Springs lavas
Big Alkali	Domes	Lava domes, minor air fall tuff	Rhyolite, dacite, and trachydacite	69.1	~6 km^2; largest body circular ~1 km in diameter	6.20 to 5.48 5.83	North-south-trending series of glassy, spongy, locally flow banded domes
Rock Springs Canyon	Domes	Lava domes	Rhyolite	76.3	7 km^2; two lobes, 1.5 x 2.5 km and 2 x 2 km	<14 and >10.5	Two east-west elongated elliptical lobes of nearly aphryic rhyolite; local zones of black obsidian

[1]K-Ar and $^{40}Ar/^{39}Ar$ ages (Fleck et al., 2015); preferred age is the average calculated from multiple age determinations, modified, as needed, to account for known relative age relations

Table 2. Summary of petrographic characteristics for Bodie Hills volcanic field rock units

Mineral abundances are microscopic estimates relative to total rock. Qz, quartz; Afs, alkali feldspar; Pl, plagioclase; Hbl, hornblende; Bt, biotite; Pyx, pyroxene; Ol, olivine; Opq, opaque Fe-Ti oxides. TR, trace. Capitalized entries in the Cpx/Opx column define whether clinopyroxene or orthopyroxene is the dominant phenocryst. Accessory minerals: Ap, apatite; Ttn, titanite; Zrn, zircon; Aln, allanite. Entries in parentheses following unit names indicate number of samples analyzed

	Relative abundances, percent											Accessory minerals
Map unit	Qz	Afs	Pl	Hbl	Bt	Pyx	Cpx/ Opx	Ol	Opq	Total xtls	Color index	
Trachyandesite of Masonic (95)			19	4	TR	4	C	TR	2	28	9	Ap
Trachyandesite of Mud Springs Canyon (3)			16	7	1	2	C		1	27	11	Ap
Trachyandesite of Sinnamon Cut (4)				9					1	10	9	
Trachydacite of East Canyon (9)			14	4	2	1	C		1	22	8	Ap
Trachyandesite of Masonic Gulch (9)			19	4	1	4	C		2	30	11	Ap
Trachyandesite of Aurora (24)			15	3		TR	C		1	19	4	Ap
Andesite of Lakeview Spring (6)			8	4	TR	4	C	TR	1	17	9	Ap
Trachydacite of Rough Creek (22)	TR		11	6	2	TR	C	TR	1	19	8	Ap, Zrn
Hornblende trachyandesite intrusions (4)			6	5		2	C		1	14	8	Ap
Basaltic trachyandesite of Rancheria (13)			TR	TR		4	C	7	3	13	13	Ap
Trachyandesite of West Brawley Peak (14)	TR		12	5	2	1	C	TR	1	21	9	Ap, Zrn
Trachyandesite of Clark Canyon (5)			18	TR		2	C/o		2	22	4	Ap
Trachydacite intrusions (9)	TR		17	1	3	TR	C		1	21	6	Ap
Rhyolite of Del Monte Canyon (7)	3	1	10	2	2	TR	C		1	18	5	Ap, Ttn
Rhyolite of Aurora Creek (8)	TR	TR	2	TR	TR	1	C		1	4	2	Ap
Rhyolite of East Brawley Peak (4)	3	2	2		1				TR	8	1	
Pyroxene rhyolite (9)			14			2	O/c		1	17	3	Ap
Trachydacite of Bridgeport Canyon (10)			15	TR		3	C		1	20	4	Ap
Trachyandesite of Del Monte (26)			16	3	3	2	C	TR	1	25	8	Ap
Rhyolite of Rock Springs (5)			TR	TR	TR				TR	TR	TR	
Trachyandesite of Aurora Canyon (18)			14	4	1	1	C		1	21	7	Ap
Rhyolite of Bodie Creek (8)	3	2	6	TR	3				1	14	3.4	Ttn, Ap, Aln, Zrn
Rhyolite of Bodie Hills (22)	3	3	7	TR	2				1	15	3	Ap, Ttn, Aln, Zrn
Rhyolite of Bald Peak (12)	1	1	TR		TR				1	3	1	
Trachydacite of Cinnabar Canyon (3)	TR		22	1	5				1	28	7	Ap
Trachyandesite of Mount Biedeman (57)			21	4	3	4	C	TR	2	33	12	Ap
Dacite of Silver Hill (23)	TR		13	6	2				1	23	10	Ap, Zrn
Trachydacite of Potato Peak (41)			12	4	2				1	18	6	Ap
Trachyandesite of Willow Springs (32)			14	5	2	2	C	TR	1	24	10	Ap
Dacite of Hot Springs Canyon (4)			11	3	3	TR	C		1	18	7	Ap
Rhyolite of Big Alkali (17)	TR	TR	14	3	3				1	20	6	Ap

36

Table 3. Average compositions of major volcanic rock units in the Bodie Hills volcanic field

Unit abbreviations: MA, trachyandesite of Masonic; MS, trachyandesite of Mud Springs Canyon; SC, trachyandesite of Sinnamon Cut; MG, trachyandesite of Masonic Gulch; AU, trachyandesite of Aurora; LS, andesite of Lakeview Spring; RC, trachydacite of Rough Creek; HT, hornblende trachyandesite; RA, basaltic trachyandesite of Rancheria; WB, trachyandesite of West Brawley Peak; CC, trachyandesite of Clark Canyon; TI, trachydacite intrusion; DC, rhyolite of Del Monte Canyon; AC, rhyolite of Aurora Creek; EB, rhyolite of east Brawley; PR, pyroxene rhyolite; BR, trachydacite of Bridgeport Canyon; DM, trachyandesite of Del Monte; RS, rhyolite of Rock Springs Canyon; TA, trachyandesite of Aurora Canyon; BC, rhyolite of Bodie Creek; BH, rhyolite of Bodie Hills; BP, rhyolite of Bald Peak; CI, trachydacite of Cinnabar Canyon; MB, trachyandesite of Mount Biedeman; SH, dacite of Silver Hill; PP, trachydacite of Potato Peak; WS, trachyandesite of Willow Springs; HS, dacite of Hot Springs Canyon; BA, rhyolite of Big Alkali

Unit	MA	MS	SC	EC	MG	AU	LS	RC	HT	RA	WB	CC	TI	DC	AC	EB
	(76)	(3)	(4)	(9)	(7)	(11)	(6)	(14)	(3)	(14)	(13)	(5)	(7)	(6)	(7)	(1)
SiO2	59.69	60.68	60.55	64.23	61.18	59.78	60.85	62.82	58.47	53.74	62.17	61.74	66.75	73.52	75.89	74.75
TiO2	0.83	0.78	0.77	0.63	0.66	0.83	0.76	0.63	0.99	1.09	0.72	0.70	0.56	0.24	0.18	0.22
Al2O3	17.64	17.46	17.20	16.92	17.57	18.00	17.14	17.34	17.72	16.74	17.18	17.59	16.87	13.82	13.31	13.43
FeO*	5.71	5.39	5.26	4.08	4.80	5.43	5.59	4.48	5.91	7.50	5.07	4.77	3.18	1.78	0.98	1.37
MnO	0.10	0.11	0.09	0.08	0.08	0.09	0.11	0.08	0.10	0.13	0.07	0.07	0.05	0.03	0.04	0.03
MgO	2.97	2.30	3.34	1.55	2.66	3.15	3.02	2.10	3.14	6.76	2.46	2.41	1.07	0.67	0.29	0.28
CaO	5.89	5.68	5.90	4.23	5.79	5.60	5.95	5.11	6.91	7.94	5.14	5.47	3.11	1.96	0.95	1.27
Na2O	4.06	4.15	4.51	4.11	4.24	3.78	4.00	4.35	3.89	3.58	3.97	3.96	4.07	3.37	3.36	3.36
K2O	2.78	3.07	2.09	3.88	2.75	3.01	2.33	2.81	2.40	2.06	2.95	2.98	4.16	4.52	4.97	5.24
P2O5	0.33	0.36	0.30	0.29	0.27	0.33	0.25	0.27	0.47	0.47	0.26	0.30	0.18	0.10	0.03	0.04
Ba	1210	1437	1123	1366	1070	1221	998	1105	1105	1039	1199	1280	1370	923	856	973
Cs	3.07	6.13	1.53	3.93	2.01	4.18	1.58	2.62	1.77	10.39	3.61	2.58	3.51	5.42	9.56	13.20
Rb	71	76	51	102	60	83	52	66	36	54	77	83	117	133	185	226
Sr	937	1107	1066	863	972	839	772	983	1597	874	849	750	598	340	124	234
Y	18.3	15.7	17.2	17.0	16.5	16.1	13.8	12.2	13.9	19.5	13.8	17.4	15.2	9.4	11.4	14.1
Zr	169	157	119	201	137	167	117	128	132	148	137	163	203	103	128	189
Hf	4.8	4.7	3.0	5.8	4.0	4.6	3.5	3.6	4.0	4.1	3.9	4.6	6.1	3.2	4.2	6.0
Nb	7.9	7.7	6.8	9.4	6.7	7.0	5.3	5.5	5.3	8.9	6.3	8.2	10.3	7.0	10.0	12.0
Th	10.1	10.5	4.1	15.9	9.9	7.4	7.7	9.5	7.6	5.0	10.1	10.2	17.1	18.6	22.7	42.2
U	3.78	3.58	1.82	5.74	4.10	2.49	3.11	3.40	2.28	1.56	3.51	3.16	6.05	6.49	7.98	12.40
La	34.6	41.3	27.8	42.6	28.5	29.4	23.0	29.6	42.4	31.7	32.6	37.6	38.1	29.0	33.5	46.7
Ce	66.0	78.2	56.2	80.9	55.0	57.5	43.1	55.7	87.4	63.6	59.6	71.1	70.3	47.9	56.2	81.2
Pr	8.2	9.7	7.0	9.6	6.5	7.0	5.2	6.5	11.0	8.0	7.1	8.4	8.0	4.9	5.8	8.4
Nd	31.2	35.9	27.7	35.5	25.4	28.1	20.1	24.7	43.6	31.6	27.4	31.6	27.9	16.2	18.6	26.4
Sm	5.6	6.3	5.3	6.2	4.5	5.4	3.7	4.3	7.3	5.9	4.9	5.6	4.6	2.6	2.9	3.9
Eu	1.33	1.56	1.30	1.35	1.17	1.34	1.01	1.08	1.90	1.57	1.28	1.32	1.04	0.58	0.41	0.56
Gd	4.45	4.81	3.89	4.49	3.73	4.06	3.18	3.04	5.41	4.85	3.78	4.70	3.57	2.03	2.04	2.53
Tb	0.62	0.58	0.51	0.59	0.53	0.57	0.48	0.43	0.69	0.66	0.51	0.65	0.52	0.29	0.31	0.42
Dy	3.34	2.92	2.85	3.20	3.02	3.20	2.55	2.33	3.08	3.57	2.67	3.31	2.71	1.51	1.70	2.32
Ho	0.65	0.55	0.57	0.59	0.60	0.60	0.50	0.44	0.53	0.69	0.51	0.66	0.52	0.31	0.34	0.45
Er	1.83	1.53	1.62	1.66	1.76	1.62	1.46	1.22	1.52	1.85	1.36	1.74	1.59	1.04	1.13	1.33
Tm	0.26	0.21	0.23	0.24	0.24	0.23	0.20	0.17	0.18	0.27	0.19	0.25	0.21	0.14	0.17	0.23
Yb	1.71	1.40	1.47	1.63	1.71	1.49	1.42	1.18	1.13	1.64	1.28	1.72	1.51	1.01	1.29	1.60
Lu	0.29	0.22	0.26	0.27	0.25	0.23	0.21	0.20	0.21	0.27	0.21	0.27	0.24	0.18	0.20	0.24
Co	19.1	18.1	19.8	11.0	14.9	17.0	18.4	14.9	15.6	32.8	17.3	14.4	8.6	4.1	1.0	2.4
Cr	46.2	26.7	88.0	22.5	40.0	56.7	71.7	41.4	30.0	262.0	50.5	55.0	17.1	8.5	bdl	bdl
Ni	33.2	26.0	63.3	19.3	22.3	31.0	25.5	26.9	25.3	122.8	26.6	25.6	10.3	9.3	6.8	bdl
Sc	10.7	10.0	8.7	7.4	10.7	12.6	13.2	8.2	8.7	17.3	11.0	9.6	6.3	3.9	3.1	bdl
V	139	134	120	94.9	123	135	136	104	146	180	114	117	77	29	8	20
Cu	48.5	54.0	31.8	40.1	63.9	71.5	36.2	32.5	27.5	44.1	33.3	33.4	21.9	7.8	3.0	21.0
Mo	2.7	2.0	2.0	3.5	2.0	4.7	3.0	3.4	bdl	3.2	3.5	3.0	3.0	4.5	4.8	5.0
Pb	16.9	18.7	17.7	21.0	17.9	15.1	14.7	17.5	11.0	10.9	17.6	21.0	22.6	24.8	30.7	32.0
Zn	74.6	73.0	84.3	63.3	64.0	73.8	61.7	59.8	87.3	84.4	77.3	79.8	48.9	24.3	28.6	24.0
Sn	2.3	1.7	1.7	2.0	1.6	1.0	1.5	2.0	1.5	1.5	1.5	1.8	1.5	2.0	1.3	1.0
W	2.0	1.0	1.0	1.4	1.0	1.7	bdl	1.3	bdl	32.0	1.3	1.0	1.7	2.0	2.5	4.0
Ta	0.64	0.60	bdl	0.63	0.55	0.51	bdl	0.65	bdl	0.66	0.60	0.55	0.69	0.78	0.93	1.30

Table 3. Average compositions of major volcanic rock units in the Bodie Hills volcanic field (*continued*)

Unit	PR	BR	DM	RS	TA	BC	BH	BP	CI	MB	SH	PP	WS	HS	BA
N=	(5)	(9)	(24)	(6)	(13)	(7)	(22)	(4)	(3)	(44)	(33)	(39)	(26)	(4)	(16)
SiO2	70.44	63.15	61.22	76.26	62.12	72.26	73.99	76.80	68.14	59.25	64.11	62.99	61.89	65.06	69.08
TiO2	0.37	0.90	0.81	0.13	0.81	0.26	0.21	0.13	0.54	0.96	0.70	0.70	0.80	0.74	0.31
Al2O3	15.58	17.22	17.40	13.48	16.99	14.91	14.04	13.06	16.46	17.49	17.20	17.37	16.60	17.37	16.54
FeO*	2.18	4.50	4.90	0.78	4.97	1.63	1.37	0.71	2.92	5.88	4.38	4.68	4.82	3.39	2.10
MnO	0.06	0.05	0.08	0.04	0.08	0.04	0.05	0.04	0.05	0.10	0.08	0.08	0.08	0.05	0.04
MgO	0.55	1.46	2.54	0.09	2.48	0.63	0.46	0.16	1.19	2.81	1.91	1.89	3.00	1.56	0.90
CaO	1.96	4.03	5.20	0.75	5.12	2.10	1.43	0.75	2.57	6.19	4.29	4.91	5.39	4.28	2.82
Na2O	3.73	4.16	3.79	3.57	3.50	3.67	3.51	2.86	3.45	3.93	3.96	3.88	3.80	3.73	4.35
K2O	5.01	4.22	3.77	4.88	3.64	4.38	4.86	5.47	4.52	2.93	3.05	3.14	3.30	3.56	3.61
P2O5	0.12	0.31	0.29	0.01	0.31	0.11	0.08	0.01	0.15	0.45	0.32	0.35	0.32	0.26	0.24
Ba	1446	1670	1362	650	1162	948	710	572	1623	1388	1404	1301	1253	1258	1595
Cs	9.92	5.03	9.92	8.13	8.24	70.6	11.2	70.9	8.33	2.97	4.73	3.27	4.15	4.78	2.52
Rb	146	137	135	167	129	223	185	278	178	76	82	85	93	111	69
Sr	333	593	660	115	684	470	252	107	699	1087	930	863	948	841	1143
Y	15.0	20.4	18.8	8.9	17.4	9.1	9.0	9.9	19.5	18.4	13.2	14.9	16.5	24.1	7.6
Zr	211	233	218	98	199	123	107	99	184	174	136	143	147	154	123
Hf	6.2	6.3	6.2	3.2	5.7	4.0	3.6	3.8	5.0	4.7	3.9	4.1	4.4	4.5	3.5
Nb	10.4	12.3	9.9	13.2	9.8	10.0	13.7	14.0	14.0	11.0	8.7	8.2	9.8	11.3	4.2
Th	17.9	16.8	19.0	22.3	20.2	19.7	24.4	23.3	16.1	9.9	8.9	9.9	12.7	13.9	4.5
U	6.14	5.41	6.20	8.18	6.35	7.23	8.63	8.98	6.60	3.16	3.09	3.38	4.64	5.21	1.89
La	41.4	46.1	41.7	29.4	39.8	29.50	31.5	30.7	41.7	45.7	34.7	35.1	37.6	39.7	21.7
Ce	74.5	84.7	78.2	47.9	72.7	50.7	50.5	51.6	73.0	84.7	63.2	64.1	69.4	81.2	38.5
Pr	8.2	10.3	9.2	4.8	8.5	5.2	5.1	5.2	8.1	10.7	7.6	7.6	8.4	10.4	4.6
Nd	27.3	38.2	34.1	14.6	32.2	16.7	16.0	16.1	28.6	42.3	28.4	29.0	32.0	42.1	16.7
Sm	4.4	6.7	6.1	2.1	5.9	2.5	2.3	2.3	4.9	7.2	4.9	5.1	5.7	7.5	2.8
Eu	0.81	1.37	1.36	0.40	1.34	0.55	0.45	0.29	1.16	1.79	1.22	1.29	1.46	1.74	0.69
Gd	3.23	5.13	4.74	1.71	4.67	1.84	1.66	1.74	4.07	5.38	3.61	4.06	4.48	6.16	2.04
Tb	0.45	0.69	0.64	0.27	0.64	0.26	0.24	0.27	0.57	0.70	0.46	0.55	0.60	0.82	0.27
Dy	2.60	3.73	3.51	1.43	3.34	1.53	1.39	1.44	3.15	3.49	2.43	2.86	3.07	4.36	1.42
Ho	0.52	0.70	0.68	0.28	0.62	0.30	0.28	0.30	0.65	0.64	0.45	0.53	0.58	0.83	0.27
Er	1.59	1.90	1.89	0.88	1.83	0.90	0.89	0.95	1.76	1.69	1.22	1.51	1.65	2.16	0.74
Tm	0.25	0.29	0.27	0.14	0.25	0.15	0.14	0.16	0.27	0.24	0.17	0.21	0.23	0.31	0.11
Yb	1.70	1.82	1.80	1.07	1.61	1.02	1.05	1.18	1.83	1.51	1.14	1.40	1.46	2.10	0.71
Lu	0.32	0.29	0.28	0.18	0.26	0.18	0.18	0.18	0.30	0.25	0.18	0.24	0.25	0.33	0.12
Co	3.1	11.3	15.2	bdl	13.8	3.4	2.7	0.8	8.0	17.8	12.1	12.6	16.9	11.0	5.0
Cr	bdl	31.3	70.8	10.0	35.5	10.8	12.4	bdl	10.0	39.8	19.5	17.7	91.5	85.0	13.5
Ni	6.5	16.7	27.6	7.8	23.7	9.0	6.9	7.0	12.0	26.6	12.4	21.9	46.3	25.8	11.5
Sc	bdl	9.4	11.8	bdl	11.5	bdl	3.6	bdl	5.0	10.1	7.2	7.5	12.3	11.3	6.0
V	28	97	120	12	117	27	20	5	63	132	93	99	128	107	35
Cu	5.0	45.1	39.0	8.0	34.8	7.3	7.9	bdl	12.0	37.2	24.6	24.8	29.2	33.8	14.9
Mo	3.3	2.9	3.5	3.7	3.0	3.3	3.1	3.8	5.0	3.2	3.2	3.0	3.1	3.7	3.0
Pb	27.6	25.1	22.9	30.0	19.5	27.8	27.3	30.8	26.3	19.1	21.3	19.6	20.5	22.3	31.8
Zn	45.4	63.0	67.6	27.5	66.9	29.8	28.7	24.0	56.3	82.0	68.1	68.7	64.0	62.3	44.2
Sn	2.8	2.4	1.9	2.0	1.8	1.8	1.7	1.8	1.3	2.0	8.4	1.6	1.7	1.3	1.3
W	2.2	1.8	2.4	2.3	1.8	3.8	2.3	2.5	2.0	2.6	1.2	1.2	1.8	1.8	1.0
Ta	0.88	0.65	0.73	0.93	0.78	0.90	1.06	1.08	0.93	0.78	0.61	0.58	0.74	0.83	bdl

Note: Major oxide data in weight percent, recalculated to 100%, volatile free, prior to average calculation. Trace element data in parts per million. bdl—below detection limit. Averages and standard deviations calculated for the number of analyses (in parentheses) available for each rock unit

Table 4. REE characteristics of volcanic rock units in the Bodie Hills volcanic field

La STD/AVE is the calculated standard deviation (STD) of the average composition (AVE) divided by the average composition

Unit	SiO_2 wt%	total REE ppm	AVE La ppm	La STD/AVE	Eu/Eu*	$(La/Yb)_N$	Ho/Ho*
Rhyolite of Big Alkali	69.08	90.7	69.8	0.23	0.859	20.5	0.660
Dacite of Hot Springs Canyon	65.06	160.1	120.9	0.11	0.894	19.5	0.702
Trachyandesite of Willow Springs	61.89	166.6	120.7	0.10	0.859	17.7	0.666
Trachydacite of Potato Peak	62.99	153.3	112.7	0.15	0.844	17.1	0.664
Dacite of Silver Hill	64.11	149.5	111.2	0.14	0.858	20.7	0.648
Trachyandesite of Mount Biedeman	59.25	205.2	145.3	0.31	0.849	21.3	0.631
Trachydacite of Cinnabar Canyon	68.14	170.0	133.8	0.06	0.781	16.9	0.742
Rhyolite of Bald Peak	76.80	100.7	90.0	0.23	0.408	18.5	0.657
Rhyolite of Bodie Hills	73.99	111.7	101.0	0.16	0.658	20.2	0.686
Rhyolite of Bodie Creek	72.26	101.8	87.4	0.28	0.750	19.3	0.689
Trachyandesite of Aurora Canyon	62.12	173.1	127.7	0.17	0.761	16.6	0.668
Rhyolite of Rock Springs Canyon	76.26	104.8	94.5	0.11	0.612	18.8	0.658
Trachyandesite of Del Monte	61.22	184.5	133.9	0.14	0.749	15.6	0.698
Trachydacite of Bridgeport Canyon	63.15	201.9	147.9	0.07	0.685	17.1	0.684
Pyroxene rhyolite	70.44	167.3	133.0	0.04	0.629	16.5	0.702
Rhyolite of east Brawley	74.75	112.4	101.0	0.33	0.509	19.2	0.687
Rhyolite of Aurora Creek	75.89	122.2	106.1	0.20	0.484	17.7	0.669
Rhyolite of Del Monte Canyon	73.52	111.6	95.3	0.12	0.738	19.2	0.706
Trachydacite intrusion	66.75	160.6	122.2	0.11	0.755	17.1	0.690
Trachyandesite of Clark Canyon	61.74	168.9	120.6	0.21	0.777	14.8	0.692
Trachyandesite of West Brawley Peak	62.17	143.2	104.5	0.20	0.873	17.9	0.681
Basaltic trachyandesite of Rancheria	53.74	155.5	102.2	0.32	0.868	13.2	0.719
Hornblende trachyandesite	58.47	205.9	136.0	0.26	0.885	25.3	0.561
Trachydacite of Rough Creek	62.82	130.9	95.1	0.22	0.879	17.0	0.707
Andesite of Lakeview Spring	60.85	105.5	73.8	0.05	0.884	11.0	0.728
Trachyandesite of Aurora	59.78	145.6	98.5	0.19	0.855	13.9	0.725
Trachyandesite of Masonic Gulch	61.18	127.5	88.5	0.12	0.873	11.8	0.743
Trachydacite of East Canyon	64.23	188.8	136.8	0.06	0.742	17.8	0.650
Trachyandesite of Sinnamon Cut	60.55	134.0	91.3	0.08	0.844	13.1	0.715
Trachyandesite of Mud Springs Canyon	60.68	185.1	132.6	0.01	0.836	20.1	0.602
Trachyandesite of Masonic	59.69	160.0	111.0	0.29	0.798	13.9	0.714

Table 5. Sr isotopic analyses of Bodie Hills volcanic field rocks

Unit abbreviations as in Table 3

Sample	Unit	Age (Ma)	$^{87}Sr/^{86}Sr_m$	2-sigma	$^{87}Rb/^{86}Sr$	$^{87}Sr/^{86}Sr_I$
203128	MA	14.13	0.705089	0.000023	0.5019	0.704988
203130	BP	9.67	0.706586	0.000014	6.0304	0.705758
203133	MB	9.27	0.705807	0.000011	0.3661	0.705759
203145	HT	11.8	0.704001	0.000014	0.0543	0.703992
203158	BR	11.08	0.705518	0.000012	0.4821	0.705442
203173	RA	11.7	0.705794	0.000009	0.1353	0.705772
203189	CC	11.31	0.705375	0.000010	0.3159	0.705324
203197	BA	6.17	0.705936	0.000004	0.1585	0.705922
203213	PP	8.93	0.705699	0.000006	0.4310	0.705644
203223	MA	14.7	0.705051	0.000004	0.0707	0.705036
203234	RC	11.67	0.704941	0.000006	0.3072	0.704890
203252	AC	11.18	0.706618	0.000011	4.8462	0.705849
203282	RC	12.87	0.705006	0.000008	0.1500	0.704979
203283	WS	8.17	0.705915	0.000012	0.2521	0.705886
203317	RS	11.0	0.706543	0.000005	5.0673	0.705751
203386	RA	11.7	0.705749	0.000013	0.1217	0.705729
203397	MS	13.87	0.705028	0.000008	0.2137	0.704986
203405	BC	10.13	0.706052	0.000010	0.2126	0.706021
203434	RA	11.7	0.705729	0.000019	0.3112	0.705677
00-BA-02	WS	8.17	0.705543	0.000008	0.3062	0.705507
00-BA-03	BH	9.69	0.706047	0.000009	1.2022	0.705882
00-BA-04	SH	9.07	0.705754	0.000005	0.4177	0.705700
00-BA-05	PP	8.93	0.705445	0.000006	0.3043	0.705406
00-BA-08	WB	11.42	0.704303	0.000009	0.1928	0.704272
00-BA-09	DC	11.16	0.705639	0.000007	1.2740	0.705437
00-BA-11	DM	10.96	0.705754	0.000010	0.8957	0.705615
00-BA-12	AC	11.18	0.706029	0.000009	3.3129	0.705503
00-BA-31	BH	9.69	0.707067	0.000009	8.5547	0.705890
00-BA-32	TA	10.45	0.705711	0.000006	0.3769	0.705655
00-BA-34	TA	10.45	0.705754	0.000006	0.9139	0.705618
00-BA-39A	WB	11.42	0.705134	0.000005	0.2003	0.705104
01-BA-22	AU	12.95	0.705160	0.000006	0.1338	0.705138
07-BA-15	BA	5.48	0.706125	0.000006	0.1296	0.706101
07-BA-38	LS	12.93	0.705107	0.000006	0.1752	0.705092
09-BA-13	MA	14.50	0.705287	0.000004	0.2298	0.705245
09-BA-19	MB	9.27	0.705824	0.000009	0.3342	0.705755
09-BA-26	SH	9.13	0.705227	0.000008	0.1624	0.705206
09-BA-35	TI	11.27	0.705611	0.000013	0.7535	0.705513
09-BA-35	TI	11.21	0.705634	0.000004	0.7535	0.705513
09SB020A	BR	11.08	0.705781	0.000008	1.0378	0.705616
10-BA-43	PP	8.93	0.705675	0.000012	0.2689	0.705633
108-10A	AU	12.58	0.705062	0.000011	0.2176	0.705034
108-11A	BC	9.89	0.705976	0.000010	0.8045	0.705832
11-BA-51	DM	10.96	0.705613	0.000010	0.7422	0.705509
MAS10-73	MG	13.47	0.704978	0.000004	0.1816	0.704950
MAS10-76 cr2	MA	14.19	0.705004	0.000003	0.1114	0.704982

Notes: m = measured, i = initial ratio calculated using measured or approximate age. 2-sigma is standard deviation of the mean from mass spectrometer run. $^{87}Rb/^{86}Sr$ calculated from trace element analyses. cr2 = second sample crush split.

Table 6. Neodymium isotopic analyses of Bodie Hills volcanic field rocks

Unit abbreviations as in Table 3

Sample	Unit	$^{143}Nd/^{144}Nd_m$	2-sigma	$^{147}Sm/^{144}Nd$	$^{143}Nd/^{144}Nd_i$	e_{Nd}^T
203128	MA	0.512542	0.000004	0.1037	0.512532	-1.71
203130	BP	0.512450	0.000011	0.0845	0.512445	-3.53
203133	MB	0.512540	0.000003	0.1044	0.512533	-1.80
203145	HT	0.512719	0.000004	0.0968	0.512712	1.72
203158	BR	0.512532	0.000007	0.1074	0.512524	-1.94
203173	RA	0.512487	0.000004	0.1068	0.512479	-2.82
203189	CC	0.512582	0.000005	0.1079	0.512574	-0.96
203197	BA	0.512464	0.000005	0.0924	0.512460	-3.31
203213	PP	0.512541	0.000015	0.1080	0.512535	-1.79
203223	MA	0.512640	0.000011	0.1293	0.512628	0.16
203234	RC	0.512634	0.000009	0.1011	0.512626	0.06
203252	AC	0.512564	0.000020	0.0903	0.512557	-1.29
203282	RC	0.512642	0.000008	0.1125	0.512633	0.21
203283	WS	0.512506	0.000014	0.0988	0.512501	-2.48
203317	RS	0.512445	0.000011	0.0854	0.512439	-3.61
203386	RA	0.512437	0.000004	0.1109	0.512429	-3.79
203397	MS	0.512598	0.000015	0.1049	0.512590	-0.65
203405	BC	0.512479	0.000020	0.1055	0.512471	-2.97
203434	RA	0.512525	0.000007	0.1135	0.512516	-2.08
00-BA-02	WS	0.512533	0.000008	0.1206	0.512527	-1.97
00-BA-03	BH	0.512418	0.000011	0.0995	0.512412	-4.17
00-BA-04	SH	0.512521	0.000010	0.1149	0.512514	-2.19
00-BA-05	PP	0.512516	0.000011	0.1201	0.512509	-2.29
00-BA-08	WB	0.512748	0.000008	0.1197	0.512739	2.26
00-BA-09	DC	0.512523	0.000008	0.1048	0.512515	-2.11
00-BA-11	DM	0.512501	0.000006	0.1188	0.512492	-2.56
00-BA-12	AC	0.512521	0.000009	0.1072	0.512513	-2.15
00-BA-31	BH	0.512437	0.000010	0.0895	0.512431	-3.79
00-BA-31dup	BH	0.512439	0.000008	0.0895	0.512433	-3.75
00-BA-32	TA	0.512488	0.000009	0.1183	0.512480	-2.82
00-BA-34	TA	0.512470	0.000009	0.1155	0.512462	-3.17
00-BA-39A	WB	0.512616	0.000009	0.1143	0.512608	-0.31
01-BA-22	AU	0.512620	0.000008	0.1292	0.512609	-0.24
07-BA-15	BA	0.512615	0.000011	0.0990	0.512611	-0.38
07-BA-38	LS	0.512474	0.000009	0.1149	0.512464	-3.06
09-BA-13	MA	0.512482	0.000005	0.1108	0.512471	-2.88
09-BA-19	MB	0.512439	0.000011	0.0960	0.512433	-3.75
09-BA-26	SH	0.512587	0.000010	0.0993	0.512581	-0.89
09-BA-35	TI	0.512520	0.000008	0.0977	0.512513	-2.16
09-BA-35	TI	0.512531	0.000005	0.0977	0.512524	-1.94
09SB020A	BR	0.512526	0.000009	0.1037	0.512518	-2.05
10-BA-43	PP	0.512529	0.000008	0.1101	0.512523	-2.03
108-10A	AU	0.512634	0.000010	0.1056	0.512625	0.07
108-11A	BC	0.512441	0.000008	0.0898	0.512435	-3.71
11-BA-51	DM	0.512527	0.000009	0.1183	0.512518	-2.06
MAS10-73	MG	0.512605	0.000008	0.1099	0.512595	-0.49
MAS10-76 cr2	MA	0.512557	0.000006	0.1082	0.512547	-1.42

Notes: m = measured, i = initial, T = time of crystallization from measured or approximate age. 2-sigma is standard deviation of the mean from mass spectrometer run. $^{143}Nd/^{144}Nd$ normalized to $^{146}Nd/^{144}Nd$ = 0.72190. $^{147}Sm/^{144}Nd$ calculated from trace element data. cr2 = second rock crushing split, dup = duplicate run on same powder split..

Table 7. Lead isotopic analyses of Bodie Hills volcanic field rocks

Unit abbreviations as in Table 3

Sample	Unit	$^{206}Pb/Pb^{204}Pb_m$	$^{207}Pb/^{204}Pb_m$	$^{208}Pb/^{204}Pb_m$	$^{238}U/^{204}Pb$	$^{235}U/^{204}Pb$	$^{232}Th/^{204}Pb$	$^{206}Pb/^{204}Pb_i$	$^{207}Pb/^{204}Pb_i$	$^{208}Pb/^{204}Pb_i$
203128	MA	19.035	15.644	38.790	17.666	0.128	48.360	18.996	15.642	38.756
203130	BP	19.072	15.654	38.867	20.226	0.147	49.840	19.041	15.652	38.843
203133	MB	19.074	15.662	38.859	9.876	0.072	29.022	19.059	15.661	38.845
203145	HT	18.955	15.619	38.622	10.578	0.077	37.542	18.937	15.618	38.601
203158	BR	19.099	15.649	38.854	13.660	0.099	40.286	19.076	15.648	38.832
203173	RA	18.945	15.634	38.755	9.752	0.071	32.584	18.928	15.633	38.738
203189	CC	19.083	15.661	38.877	11.841	0.086	39.373	19.062	15.660	38.855
203197	BA	18.993	15.657	38.822	3.861	0.028	11.162	18.989	15.657	38.818
203213	PP	19.061	15.657	38.843	11.382	0.083	33.606	19.045	15.656	38.828
203223	MA	18.996	15.648	38.763	6.338	0.046	24.678	18.981	15.647	38.746
203234	RC	19.061	15.686	38.917	13.742	0.100	39.336	19.036	15.685	38.895
203252	AC	19.079	15.672	38.903	22.155	0.161	62.754	19.040	15.670	38.868
203282	RC	18.995	15.643	38.743	11.655	0.085	31.880	18.972	15.642	38.724
203283	WS	19.062	15.659	38.850	13.685	0.099	39.635	19.045	15.658	38.834
203317	RS	19.058	15.641	38.818	20.116	0.146	57.131	19.024	15.639	38.787
203386	RA	17.317	15.481	37.661	3.010	0.022	13.361	17.312	15.481	37.654
203397	MS	19.002	15.641	38.753	11.180	0.081	32.349	18.978	15.639	38.731
203405	BC	19.023	15.686	38.938	3.634	0.026	9.554	19.017	15.686	38.933
203434	RA	19.020	15.637	38.771	30.044	0.218	83.549	18.965	15.634	38.723
00-BA-02	WS	19.047	15.647	38.800	49.965	0.362	17.544	18.985	15.644	38.793
00-BA-03	BH	19.057	15.641	38.822	65.303	0.474	20.693	18.957	15.636	38.812
00-BA-04	SH	19.058	15.644	38.803	35.902	0.260	11.784	19.008	15.641	38.797
00-BA-05	PP	19.047	15.642	38.783	36.537	0.265	12.036	18.997	15.639	38.777
00-BA-08	WB	18.991	15.626	38.686	54.782	0.397	18.741	18.895	15.621	38.676
00-BA-09	DC	19.037	15.635	38.758	51.904	0.376	17.939	18.947	15.630	38.748
00-BA-11	DM	19.104	15.647	38.848	82.323	0.597	26.804	18.963	15.640	38.833
00-BA-12	AC	19.084	15.665	38.875	45.125	0.327	14.981	19.005	15.661	38.867
00-BA-31	BH	19.085	15.662	38.898	22.572	0.164	59.073	19.051	15.660	38.869
00-BA-32	TA	19.071	15.650	38.850	15.353	0.111	74.264	19.030	15.648	38.804
00-BA-34	TA	19.074	15.638	38.814	25.771	0.187	86.828	19.032	15.636	38.769
00-BA-39A	WB	19.037	15.673	38.850	9.367	0.068	29.433	19.020	15.672	38.833
01-BA-22	AU	18.968	15.635	38.697	6.667	0.048	20.434	18.954	15.634	38.684
07-BA-15	BA	19.008	15.649	38.804	4.548	0.033	11.005	19.000	15.648	38.797
07-BA-38	LS	18.917	15.635	38.660	9.491	0.069	31.808	18.909	15.634	38.651
09-BA-13	MA	18.983	15.642	38.760	10.401	0.075	31.399	18.962	15.641	38.740
09-BA-19	MB	19.110	15.672	38.944	15.292	0.111	56.414	19.076	15.670	38.904
09-BA-26	SH	19.040	15.651	38.810	9.871	0.072	29.777	19.026	15.650	38.796
09-BA-35	TI	19.061	15.657	38.839	13.091	0.095	39.678	19.042	15.656	38.821
09-BA-35	TI	19.064	15.660	38.852	13.094	0.095	39.688	19.041	15.659	38.830
09SB020A	BR	19.113	15.656	38.878	15.024	0.109	48.325	19.087	15.654	38.851
10-BA-43	PP	19.054	15.645	38.803	10.225	0.074	32.480	19.036	15.644	38.785
108-10A	AU	19.007	15.639	38.738	12.311	0.089	33.721	18.990	15.638	38.723
108-11A	BC	19.084	15.650	38.854	21.430	0.155	65.936	19.042	15.648	38.813

11-BA-51	DM	19.097	15.644	38.833	17.347	0.126	51.673	19.070	15.642	38.808
MAS10-73	MG	19.101	15.650	38.792	21.578	0.156	51.823	19.064	15.648	38.763
MAS10-76cr2	MA	19.031	15.641	38.773	23.684	0.172	53.180	18.979	15.638	38.736

Notes: m = measured, i = initial ratios calculated using measured or approximate ages. U/Pb and Th/Pb calculated using trace element data. cr2 = second rock crush split. See text for analytical uncertainties in Pb isotope ratios.

Table 8. Summary of intensive parameter values calculated from mineral compositions

Unit	Composition	Sample	Mineral	P, kbar	T, C	Comments	fO_2
Bodie Hills	Rhyolite	00-BA-3	hornblende	2.7±0.2	725		
			sphene		741 ± 13	at 2.7 kbar, P from Al-in-hornblende	
			plagioclase-alkali feldspar		798	at 2.7 kbar, P from Al-in-hornblende	
Bodie Hills	Rhyolite	00-BA-50	plagioclase-alkali feldspar		728		
Willow Springs	Trachyandesite	00-BA-1	hornblende	4.3±0.3	800		
Willow Springs	Trachyandesite	00-BA-2	apatite		820 ± 25	1-pyroxene; apparent high T-rim vs core	
Willow Springs	Trachyandesite	08-BA-51	apatite		800 ± 20	1-pyroxene; apparent high T-rim vs core	
Mount Biedeman	Trachyandesite	09-BA-19	apatite		825 ± 25	1 pyroxene+olivine; apparent high-T cores vs rims	
			hornblende	1.0±0.1	875		
Mount Biedeman	Trachyandesite	09-BA-22	hornblende	1.0±0.1	870		
			apatite		775 ± 25	1-pyroxene	
Mount Biedeman	Trachyandesite	203381	hornblende	3.5±0.2	850	phenocrysts	
			hornblende	2.0±0.2	900	small	
			hornblende	1.2±0.1	860	wall rock	
			hornblende	3.9-4.7	845-865	Rims on pyroxene	
			apatite		800 ± 25	1-pyroxene	
Masonic	Trachyandesite	10-BA-11	hornblende	1.5±0.2	865		
			clinopyroxene-orthopyroxene		910	at 1.5 kbar from Al-in-hornblende	
Masonic	Trachyandesite	11-BA-30	clinopyroxene-orthopyroxene		900	at 1.5 kbar from Al-in-hornblende	
Masonic	Trachyandesite	09-BA-13	Oxide minerals		960 ± 30	Most consistent fits of equilibrium test	NNO + 1.2
West Brawley Peak (intrusion)	Trachyandesite	00-BA-38	Oxide minerals		717 ± 21	Most consistent fits of equilibrium test	NNO + 1.2
Aurora Canyon	Trachyandesite	00-BA-35	Oxide minerals		711 ± 17	Most consistent fits of equilibrium test	NNO + 0.2
Del Monte	Trachyandesite	00-BA-13	Oxide minerals		916 ± 10	Most consistent fits of equilibrium test	NNO + 0.2
Silver Hill	Trachydacite	00-BA-4	Oxide minerals		748 ± 24	Most consistent fits of equilibrium test	NNO + 1.5

Supplemental figures/tables

1. dist of felsic, int. and mafic rocks in the BHVF
2. geophys summary
3. alumina saturation
4. MALI
5. Mg/(Mg+Fe)
6. AFM
7. Cs vs SiO_2
8. Pb vs SiO_2
9. Rb vs SiO_2
10. Ta vs SiO_2
11. Th vs SiO_2
12. U vs SiO_2
13. $(La/Lu)_N$ vs SiO_2
14. Co vs SiO_2
15. Cr vs SiO_2
16. Ni vs SiO_2
17. Sc vs SiO_2
18. Sr vs SiO_2
19. V vs SiO_2
20. Y vs SiO_2
21. Zn vs SiO_2
22. Eu/Eu* vs SiO_2
23. Total REE vs SiO_2
24. Ba vs SiO_2
25. Zr vs SiO_2
26. Hf vs SiO_2
27. La vs SiO_2
28. Nb vs SiO_2
29. Total REE vs age
30. La vs age
31. average Eu/Eu vs SiO_2
32. Eu/Eu vs age
33. $(La/Yb)_N$ vs SiO_2
34. $(La/Yb)_N$ vs age
35. Ho/Ho* vs SiO_2
36. Ho/Ho* vs age
37. REE dispersion vs age
38. REE dispersion vs SiO_2
39. feldspar tern comp
40. hb min comps
41. bio min comps
42. pyx min comps
43. ol min comps
44. fe-ti min comps
45. SEM images: hornblende
46. SEM images: olivine
47. SEM images: pyroxene
48. SEM images: various minerals
49. Ba/Nb vs SiO_2
50. Sr/Y vs Y
51. Pb/Ce vs SiO_2
52. P_2O_5/K_2O vs SiO_2
53. P_2O_5/K_2O vs MgO
54. CaO/Al_2O_3 vs SiO_2
55. La/Sm vs SiO_2
56. Zr/Sm vs SiO_2

Supplemental Tables

1. BHVF whole rock geochem data
2. Representative mineral compositions

This is a preprint, the final version is subject to change, of the American Mineralogist (MSA)
Cite as Authors (Year) Title. American Mineralogist, in press.
(DOI will not work until issue is live.) DOI: http://dx.doi.org/10.2138/am-2016-5440

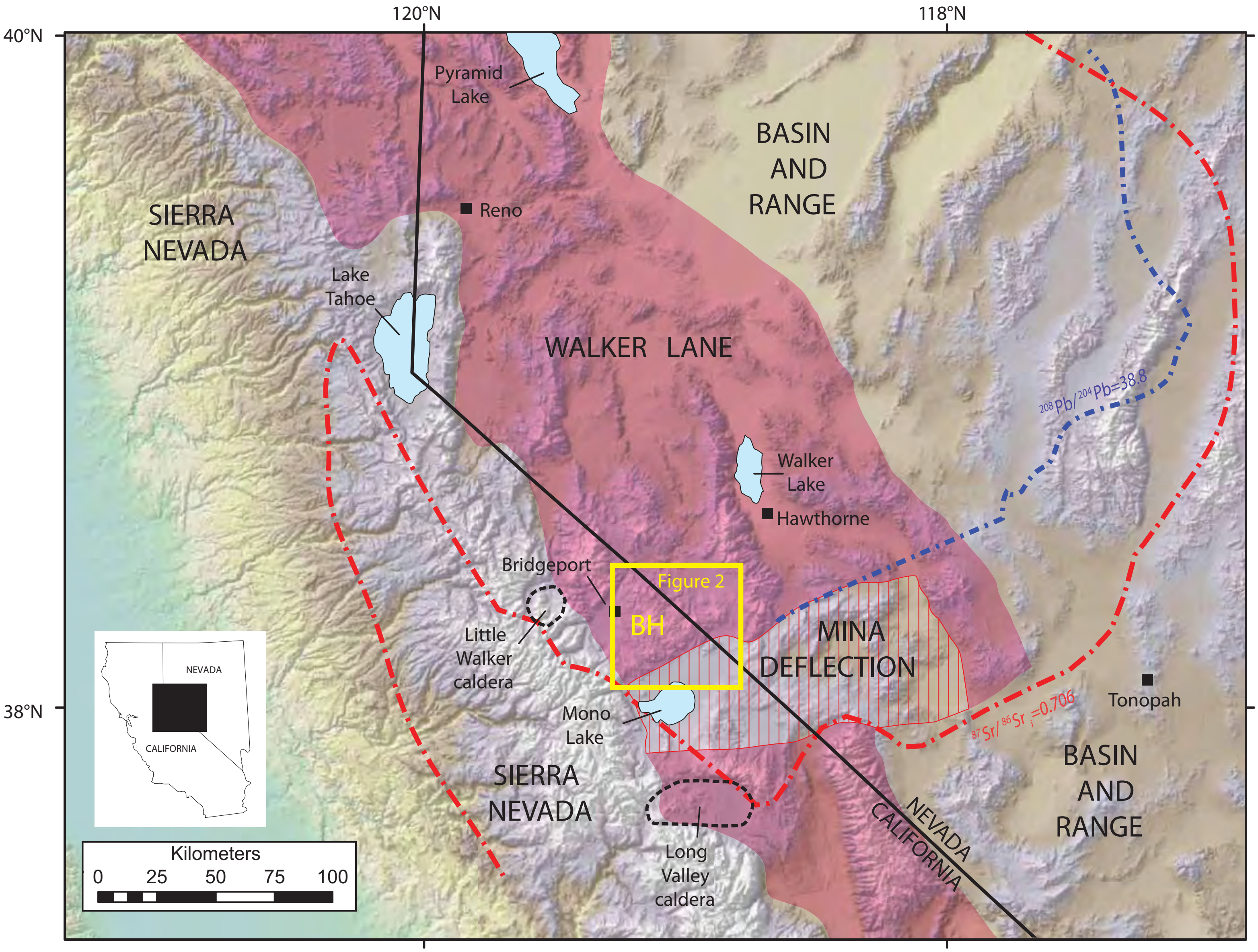

Figure 1 du Bray, John, Cousens, Hayden, and Vikre

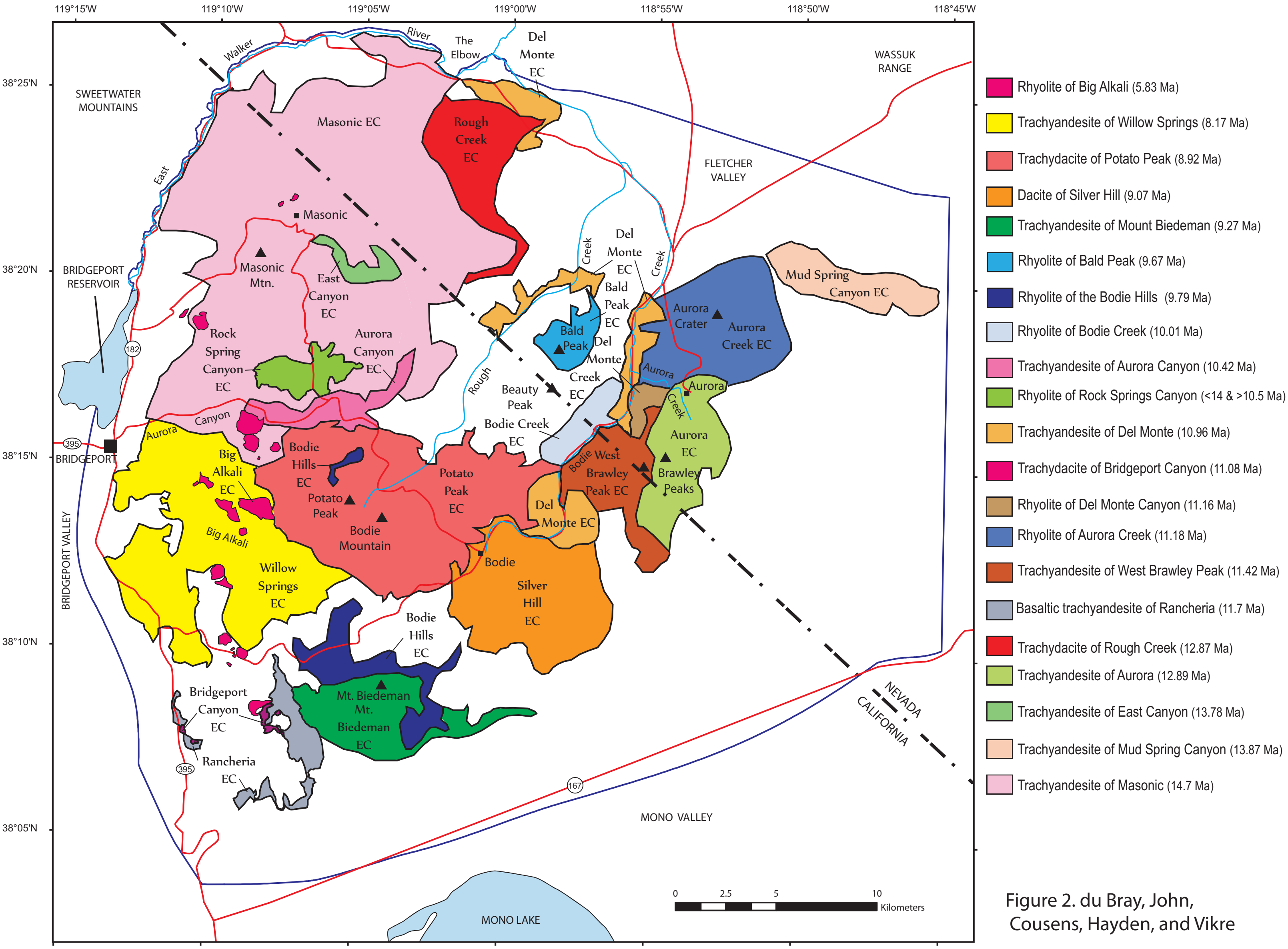

Figure 2. du Bray, John, Cousens, Hayden, and Vikre

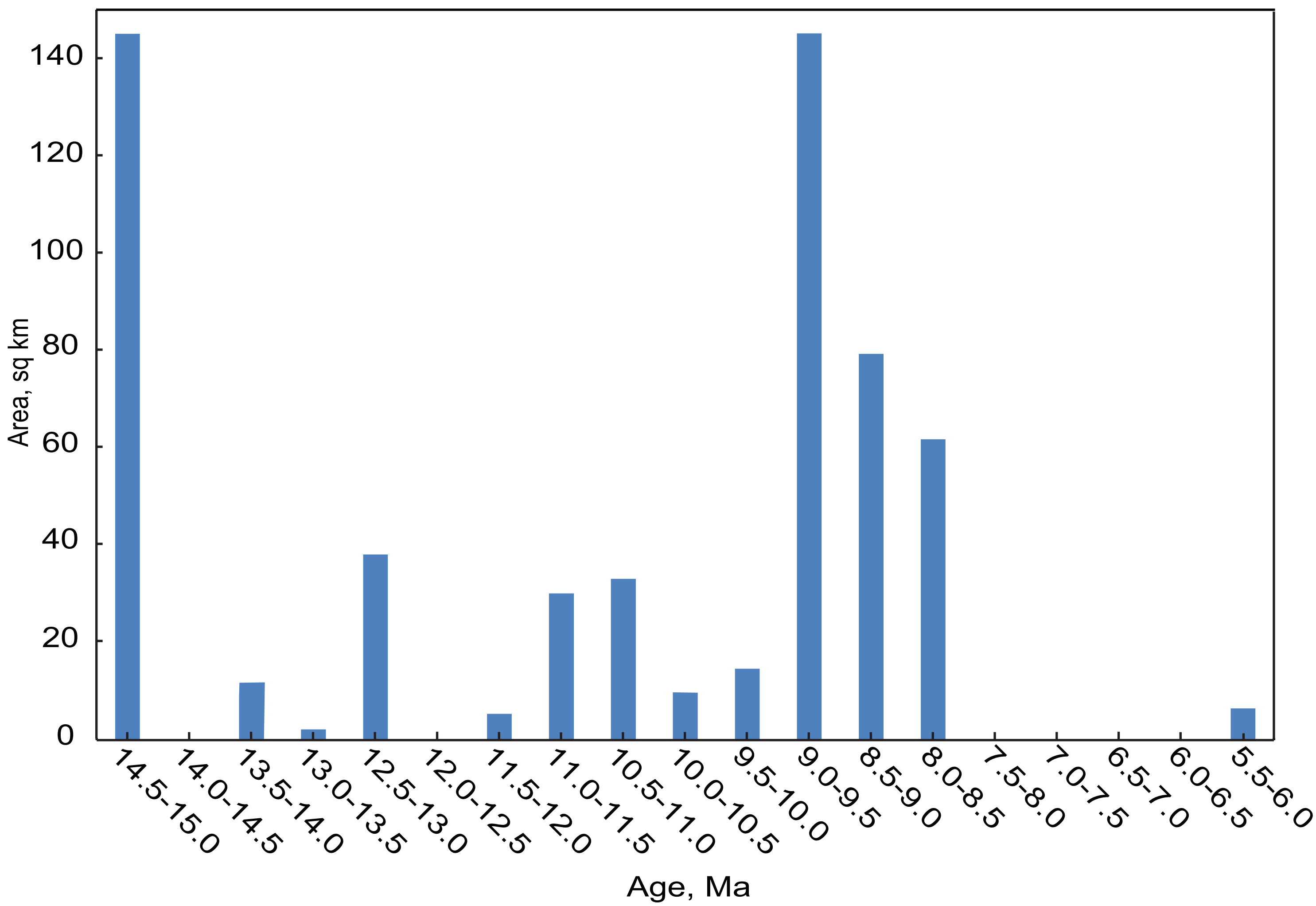

Figure 3. du Bray, John, Cousens, Hayden, and Vikre

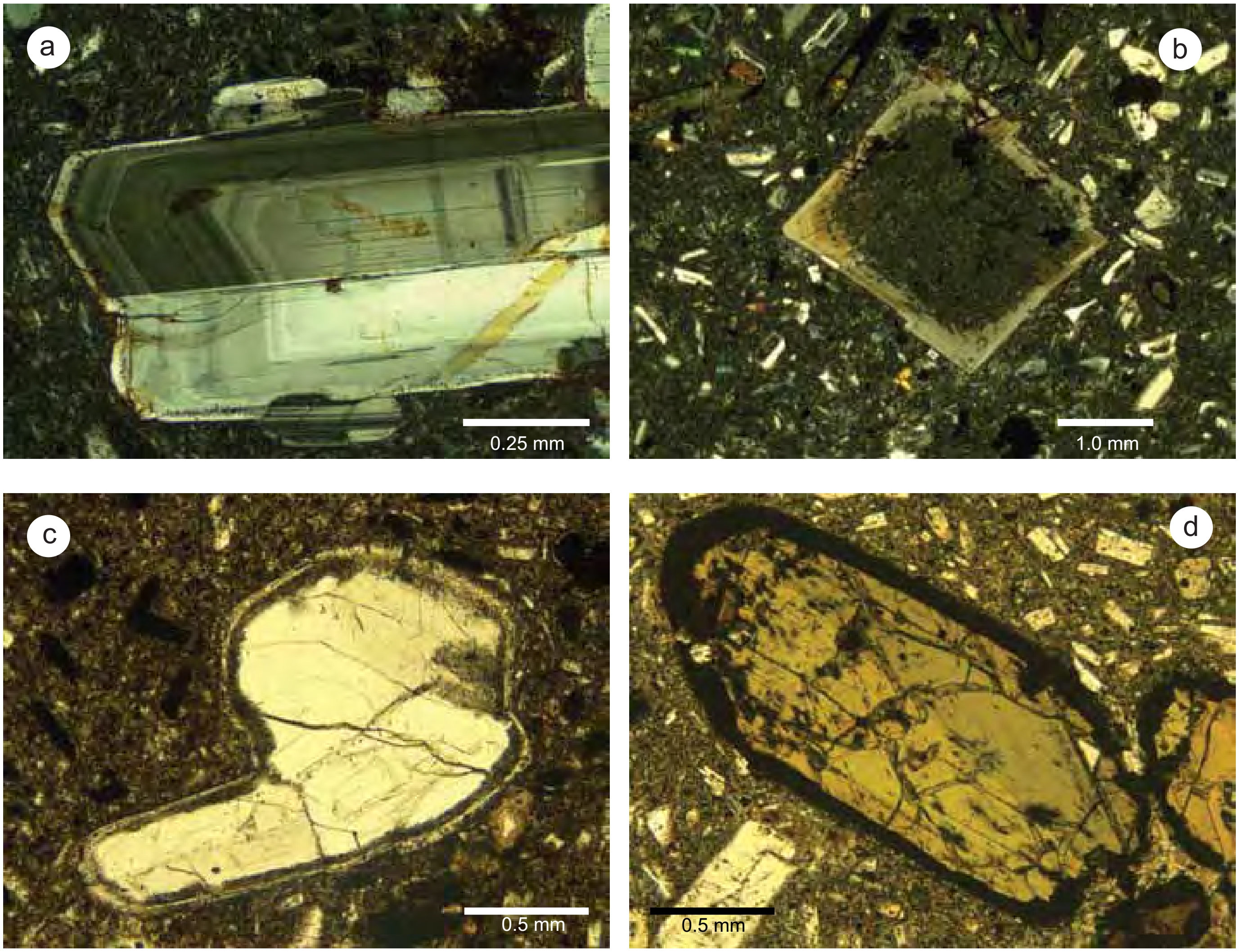

Figure 4 du Bray, John, Cousens, Hayden, and Vikre

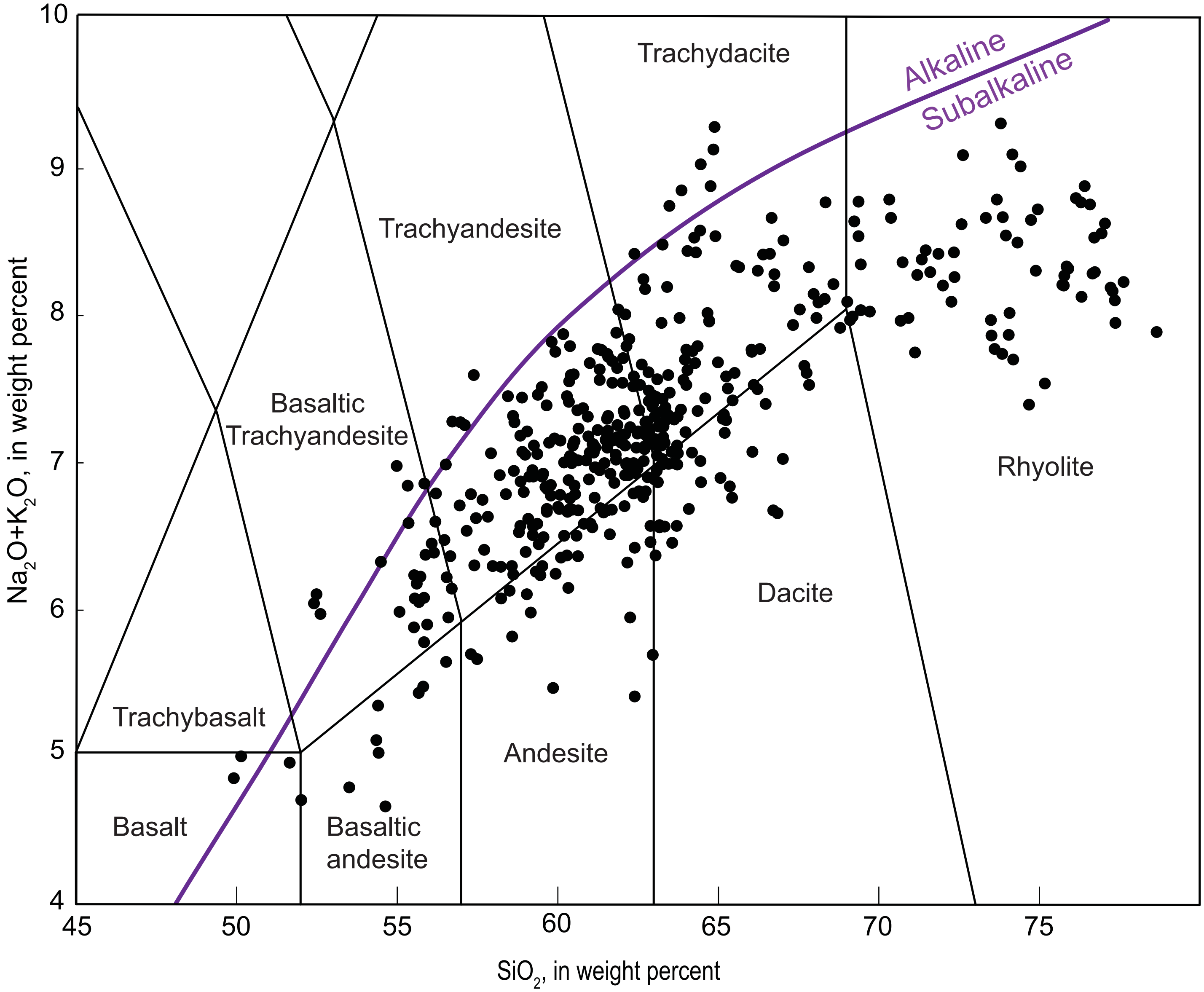

Figure 5. du Bray, John, Cousens, Hayden, and Vikre

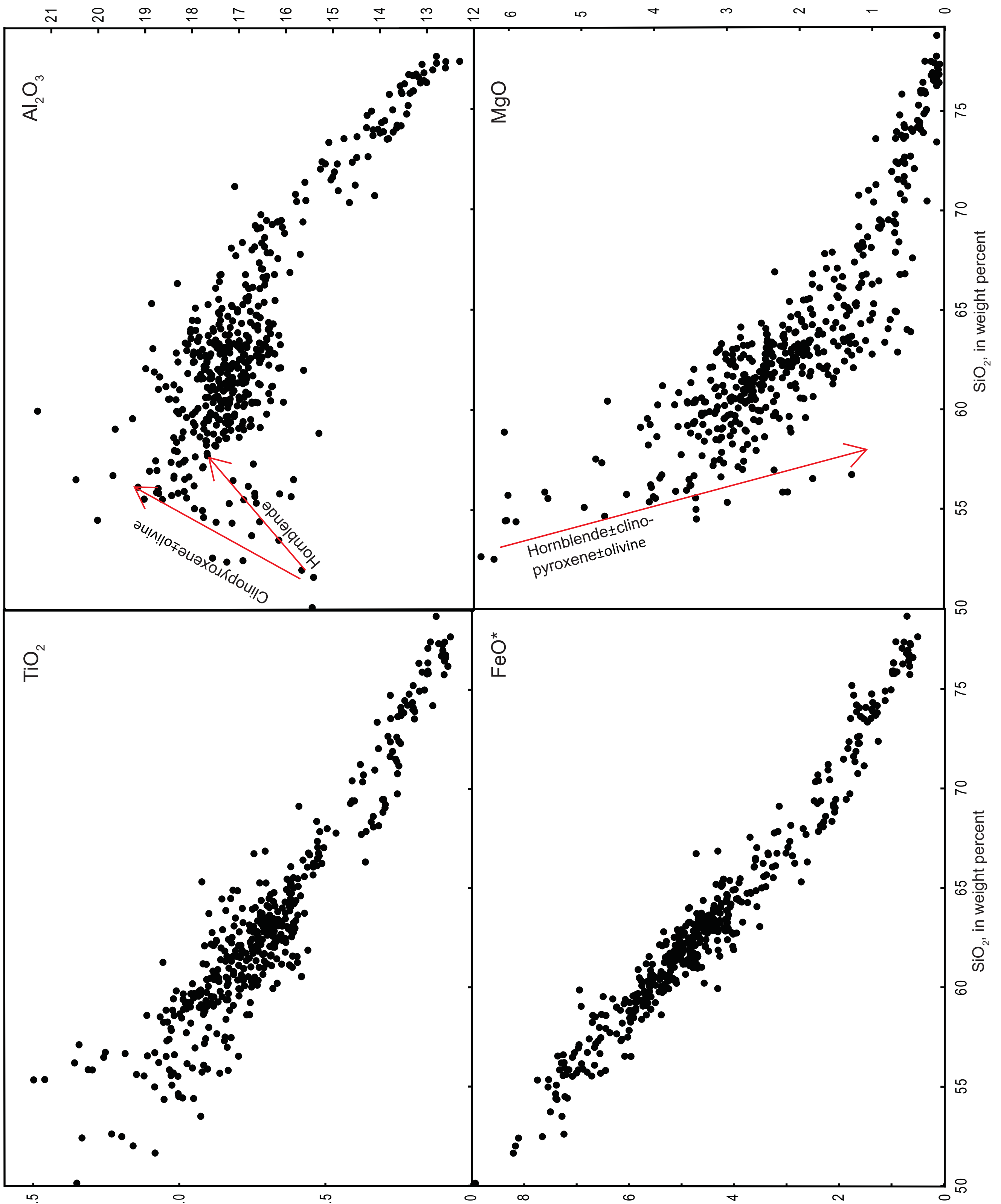

Fig. 6 (left) du Bray, John, Cousens, Hayden, and Vikre

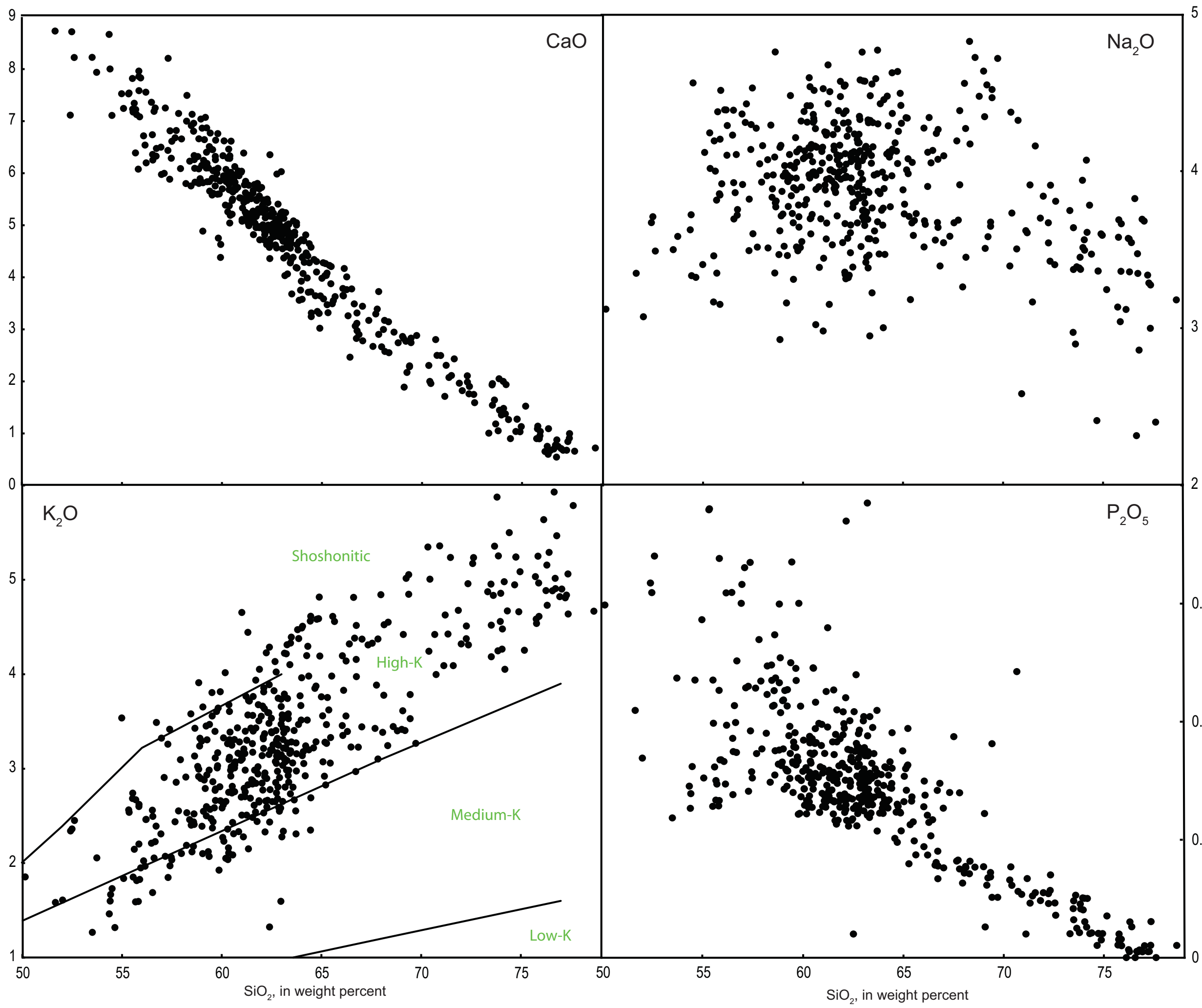

Fig. 6 (right) du Bray, John, Cousens, Hayden, and Vikre

This is a preprint, the final version is subject to change, of the American Mineralogist (MSA)
Cite as Authors (Year) Title. American Mineralogist, in press.
(DOI will not work until issue is live.) DOI: http://dx.doi.org/10.2138/am-2016-5440

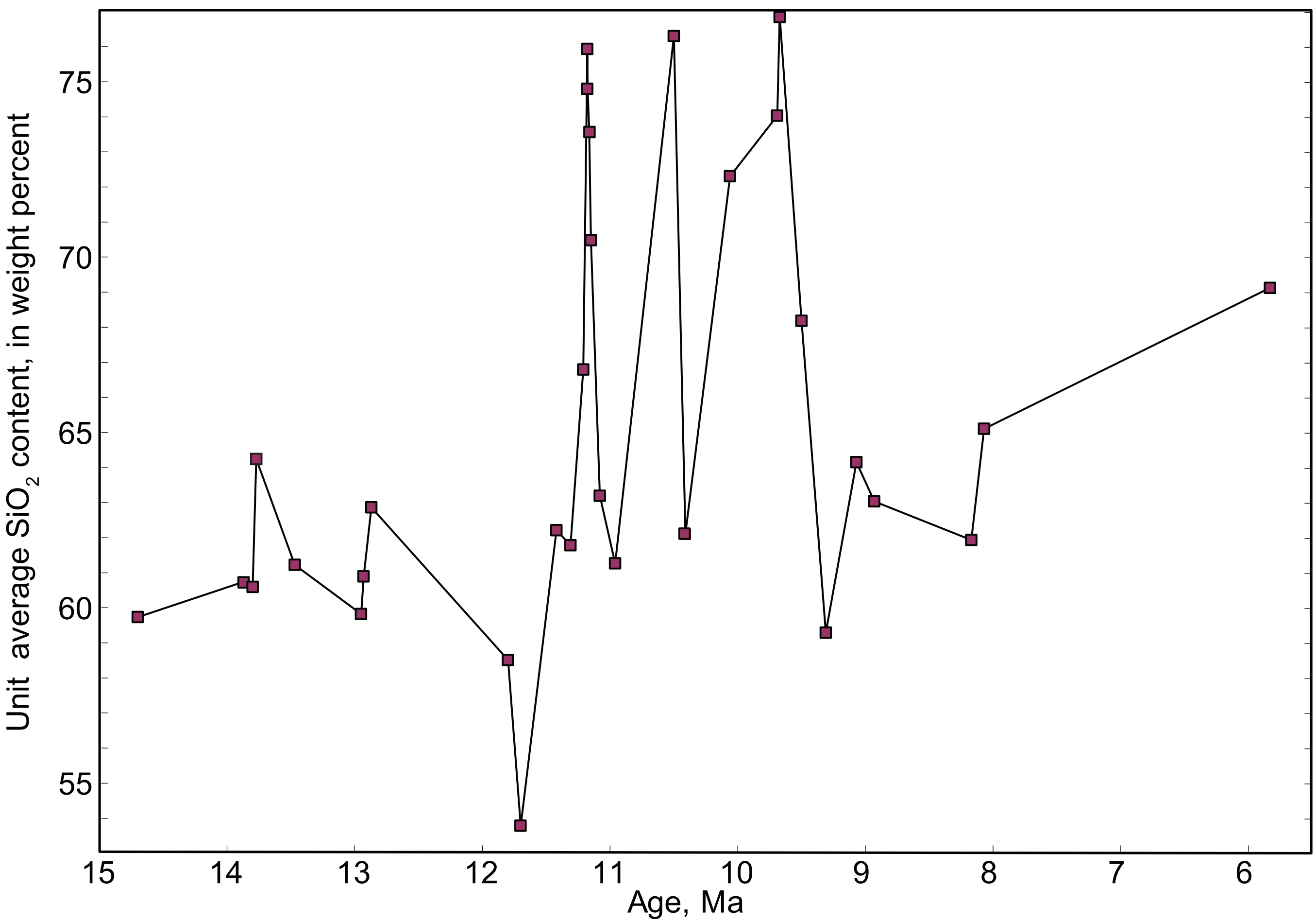

Figure 7 du Bray, John, Cousens, Hayden, and Vikre

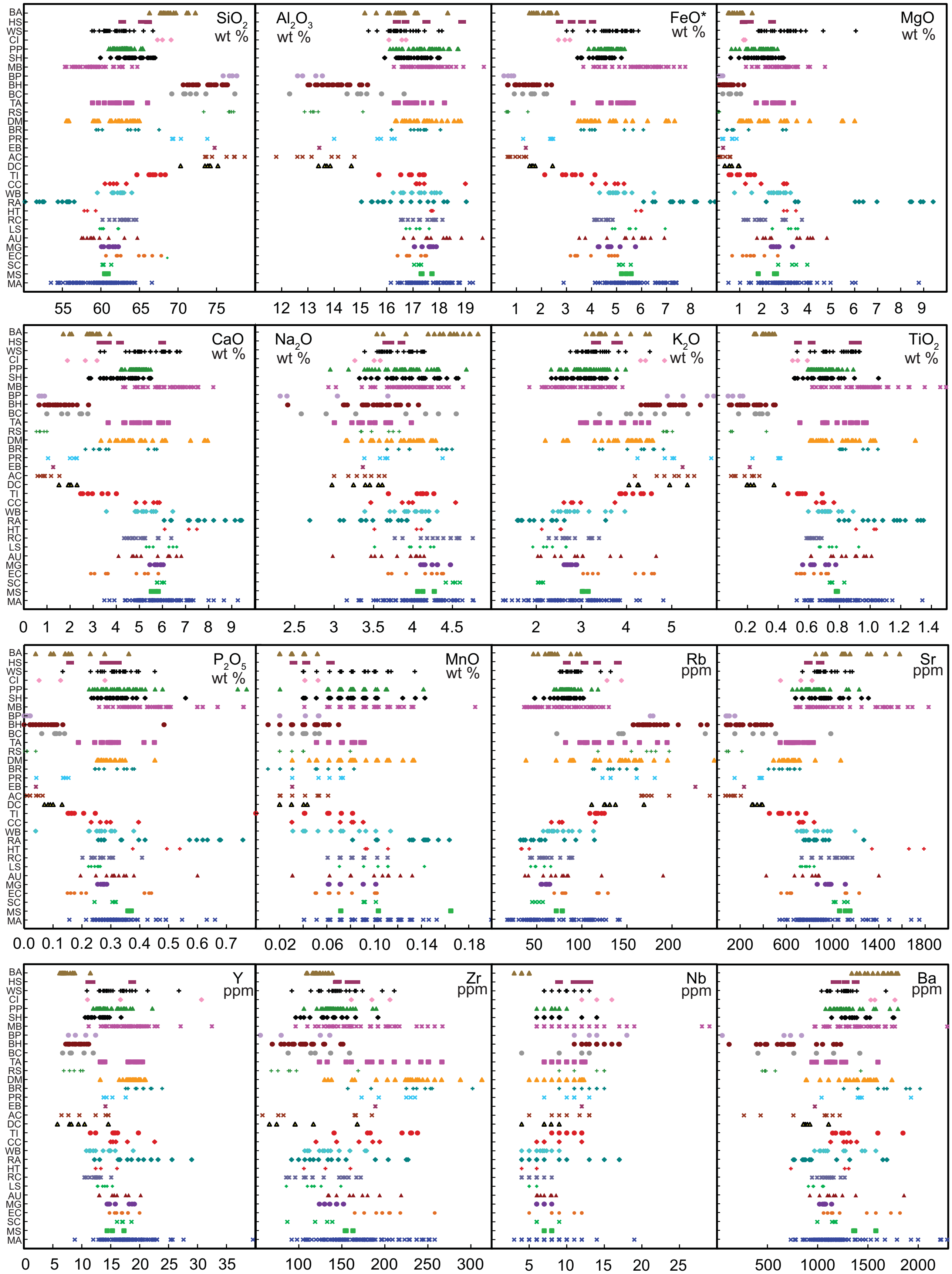

Figure 8 left du Bray, John, Cousens, Hayden, and Vikre

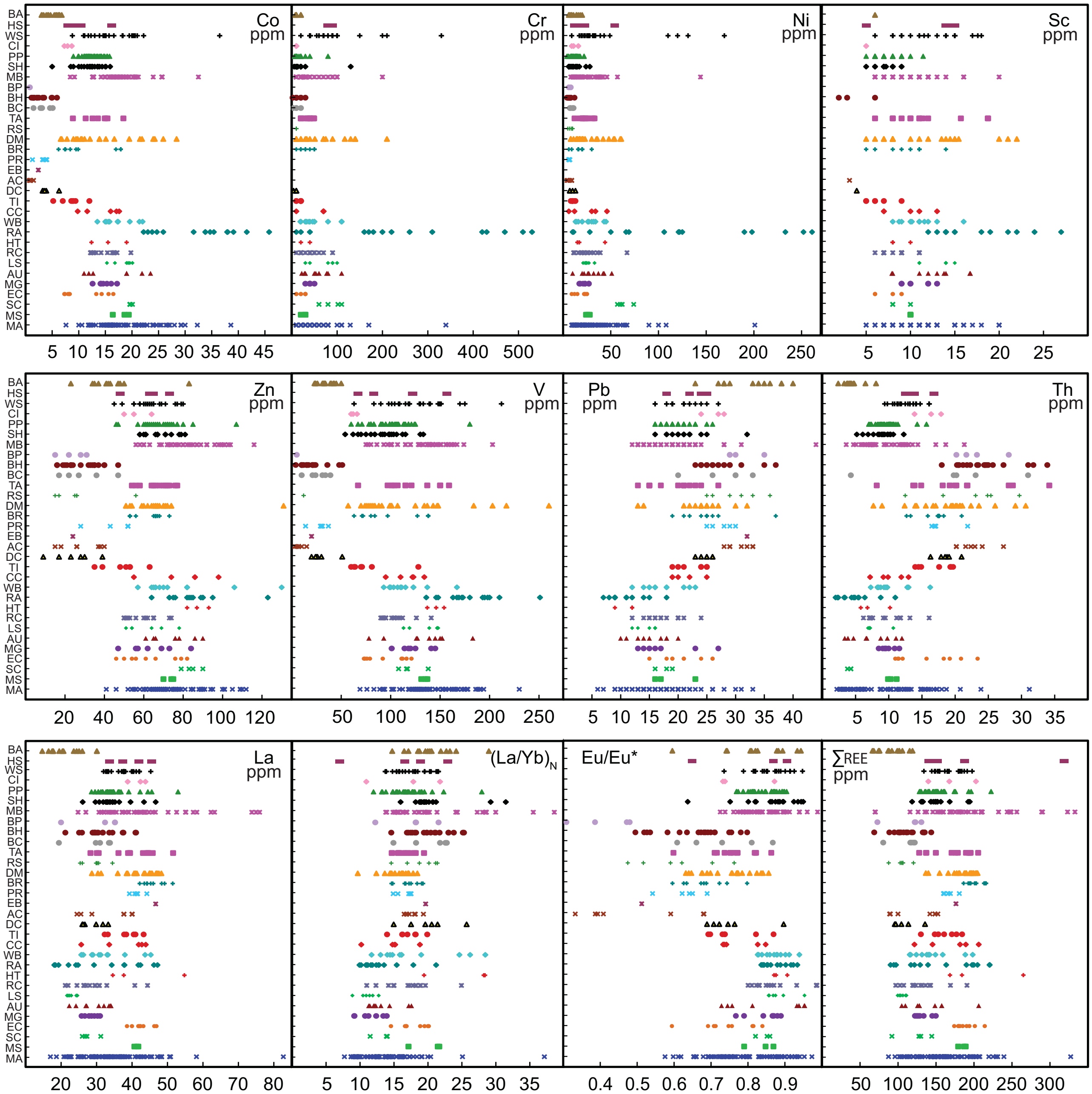

Figure 8 left du Bray, John, Cousens, Hayden, and Vikre

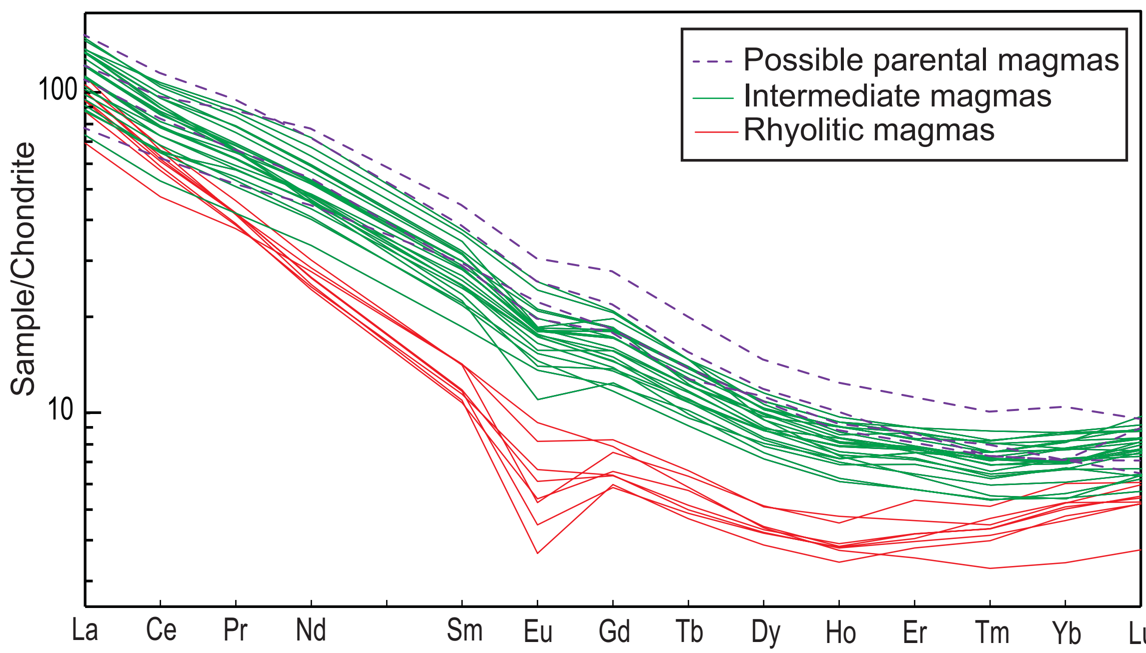

Figure 9 du Bray, John, Cousens, Hayden, and Vikre

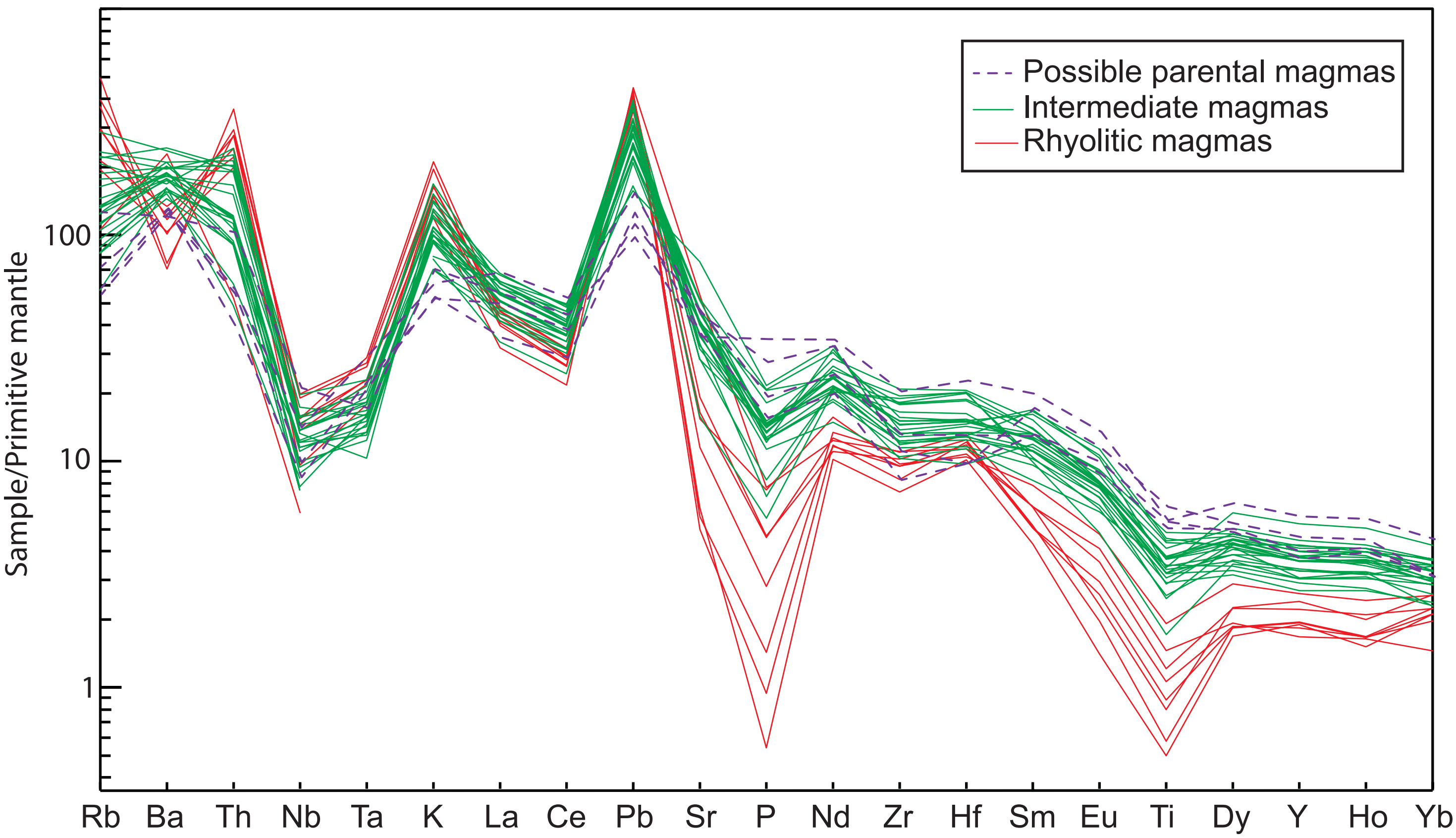

Figure 10 du Bray, John, Cousens, Hayden, and Vikre

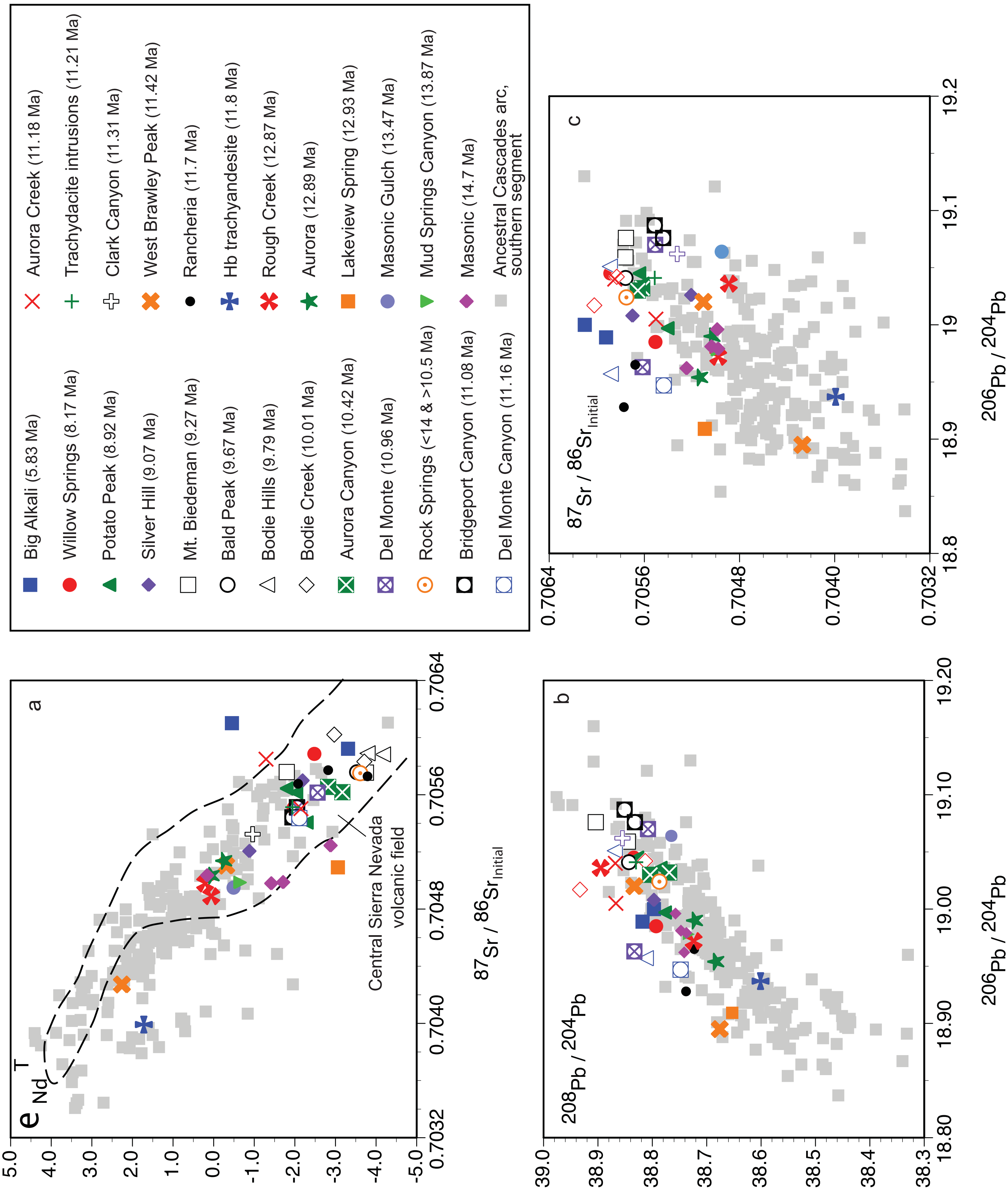

Figure 11 du Bray, John, Cousens, Hayden, and Vikre

This is a preprint, the final version is subject to change, of the American Mineralogist (MSA)
Cite as Authors (Year) Title. American Mineralogist, in press.
(DOI will not work until issue is live.) DOI: http://dx.doi.org/10.2138/am-2016-5440

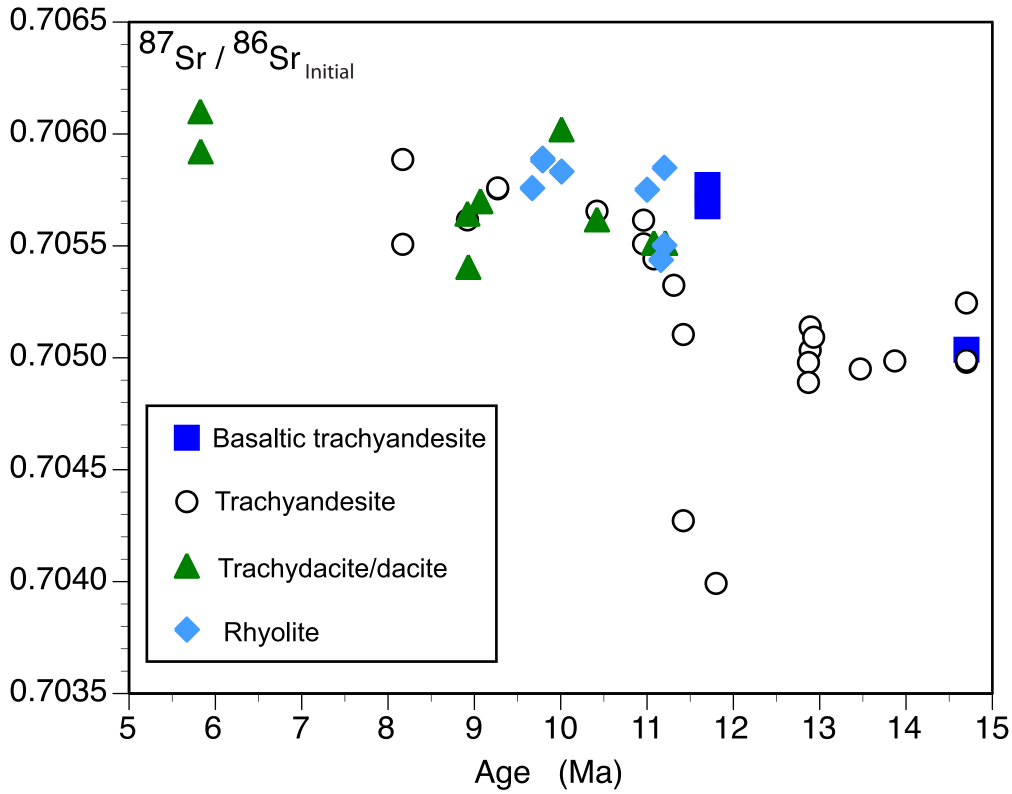

Figure 12 du Bray, John, Cousens, Hayden, and Vikre

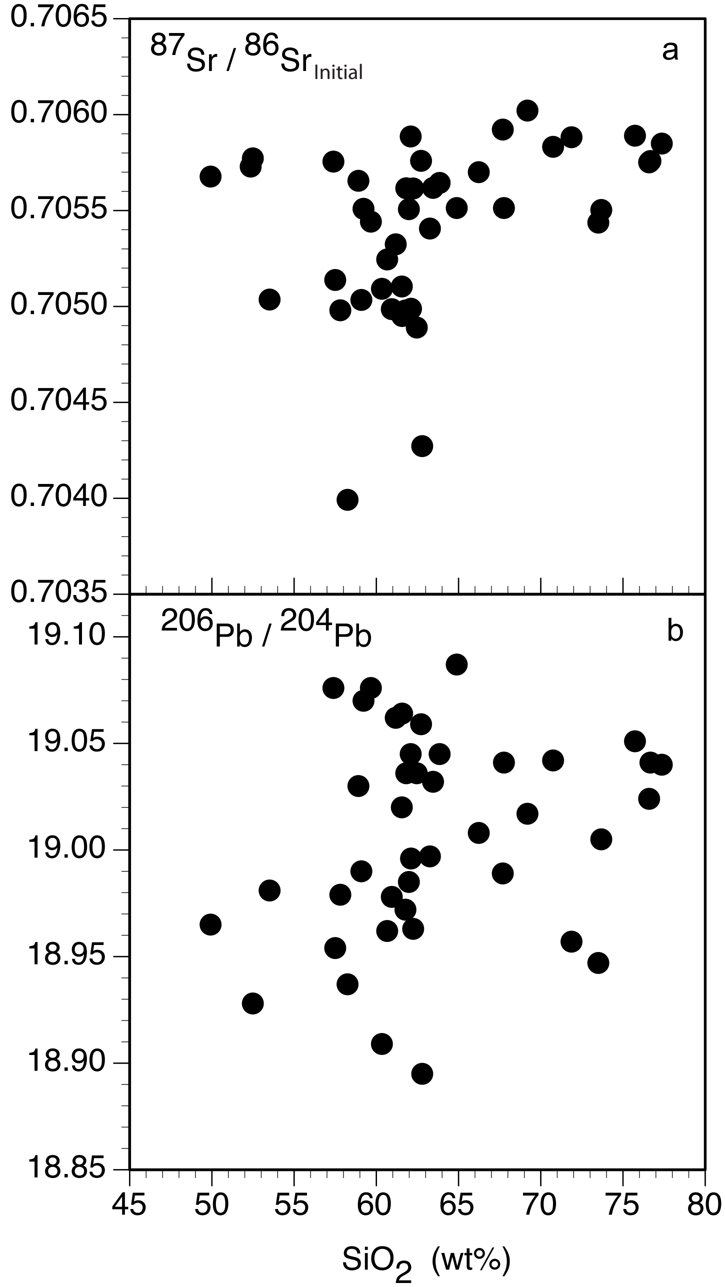

Figure 13 du Bray, John, Cousens, Hayden, and Vikre

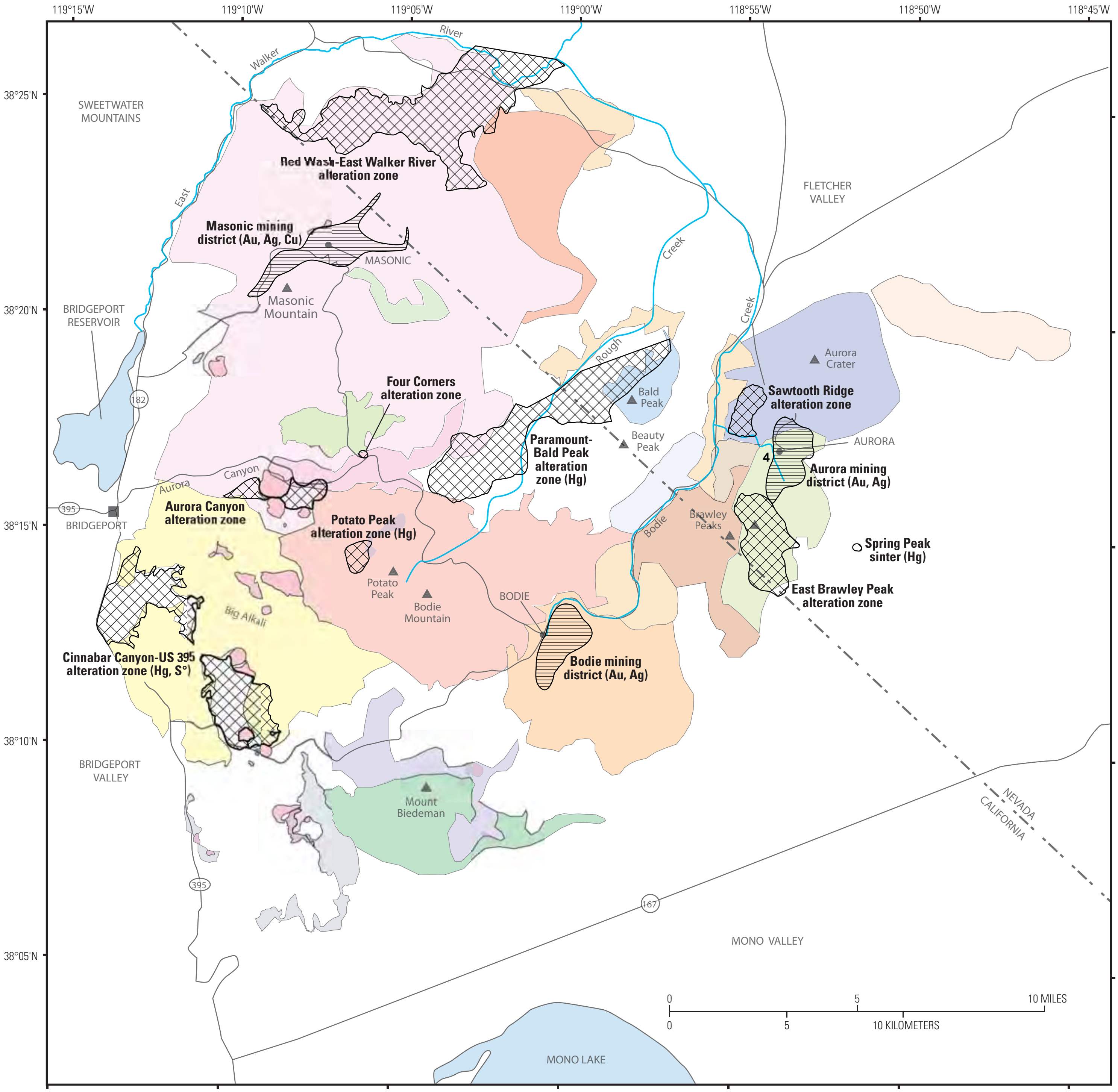

Figure 14. du Bray, John, Cousens, Hayden, and Vikre

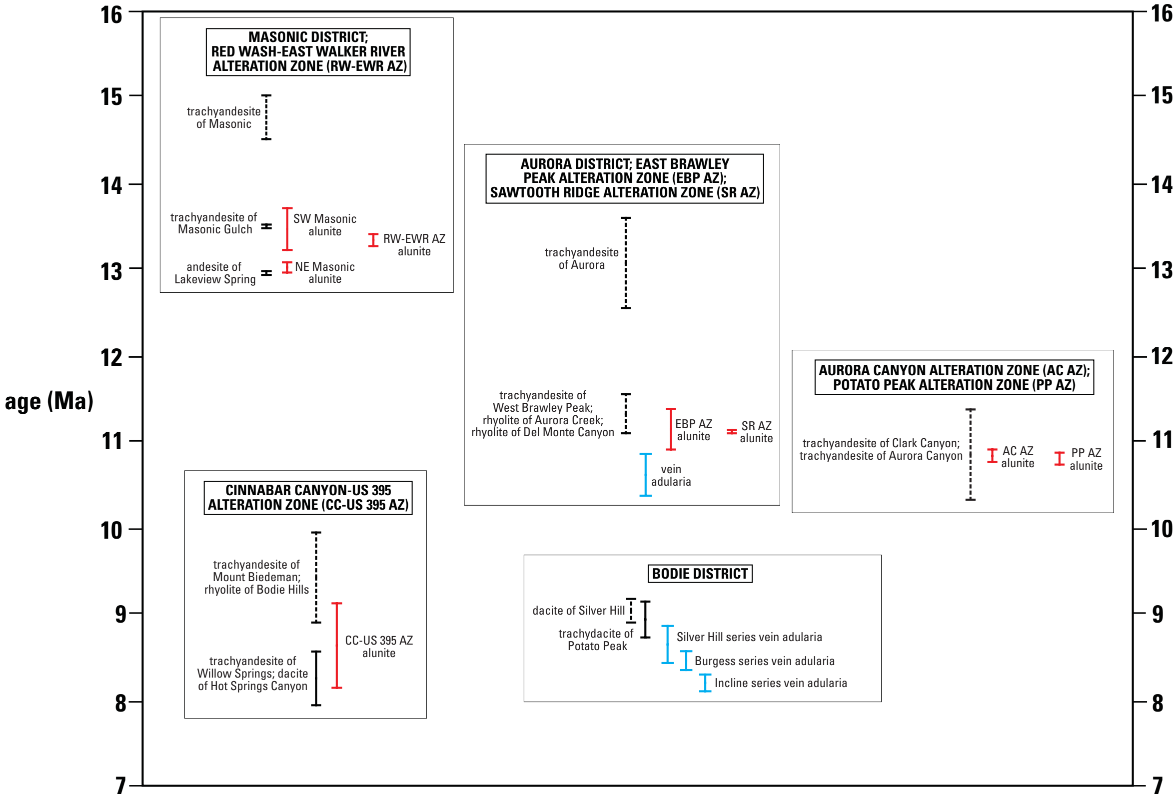

Figure 15. du Bray, John, Cousens, Hayden, and Vikre

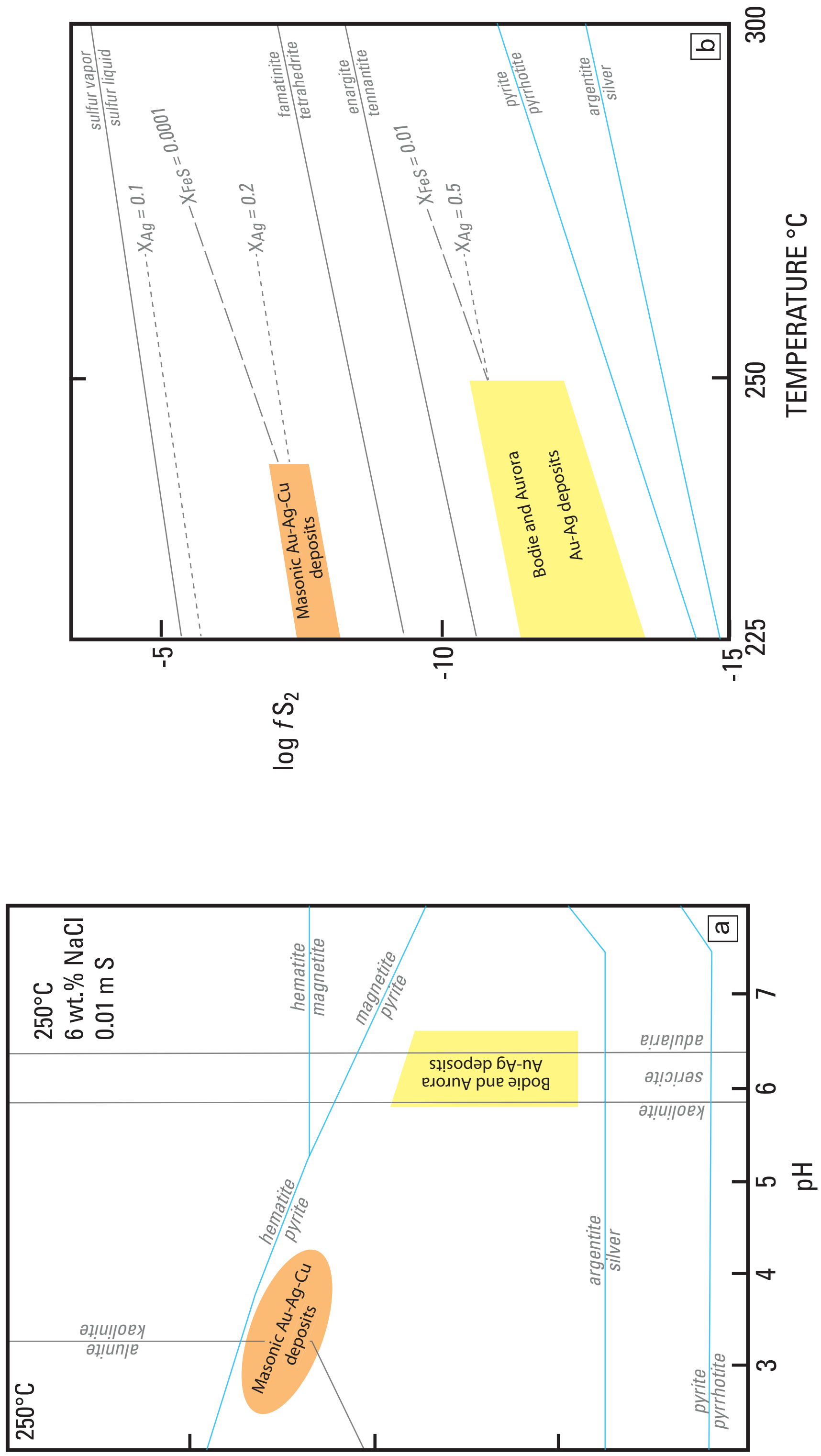

Figure 16. du Bray, John, Cousens, Hayden, and Vikre

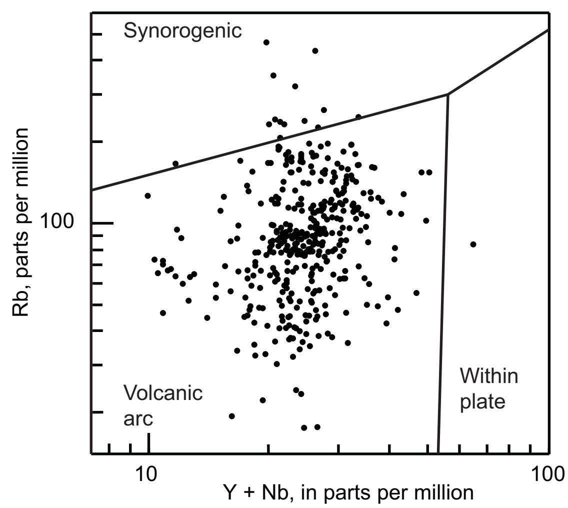

Figure 17 du Bray, John, Cousens, Hayden, and Vikre

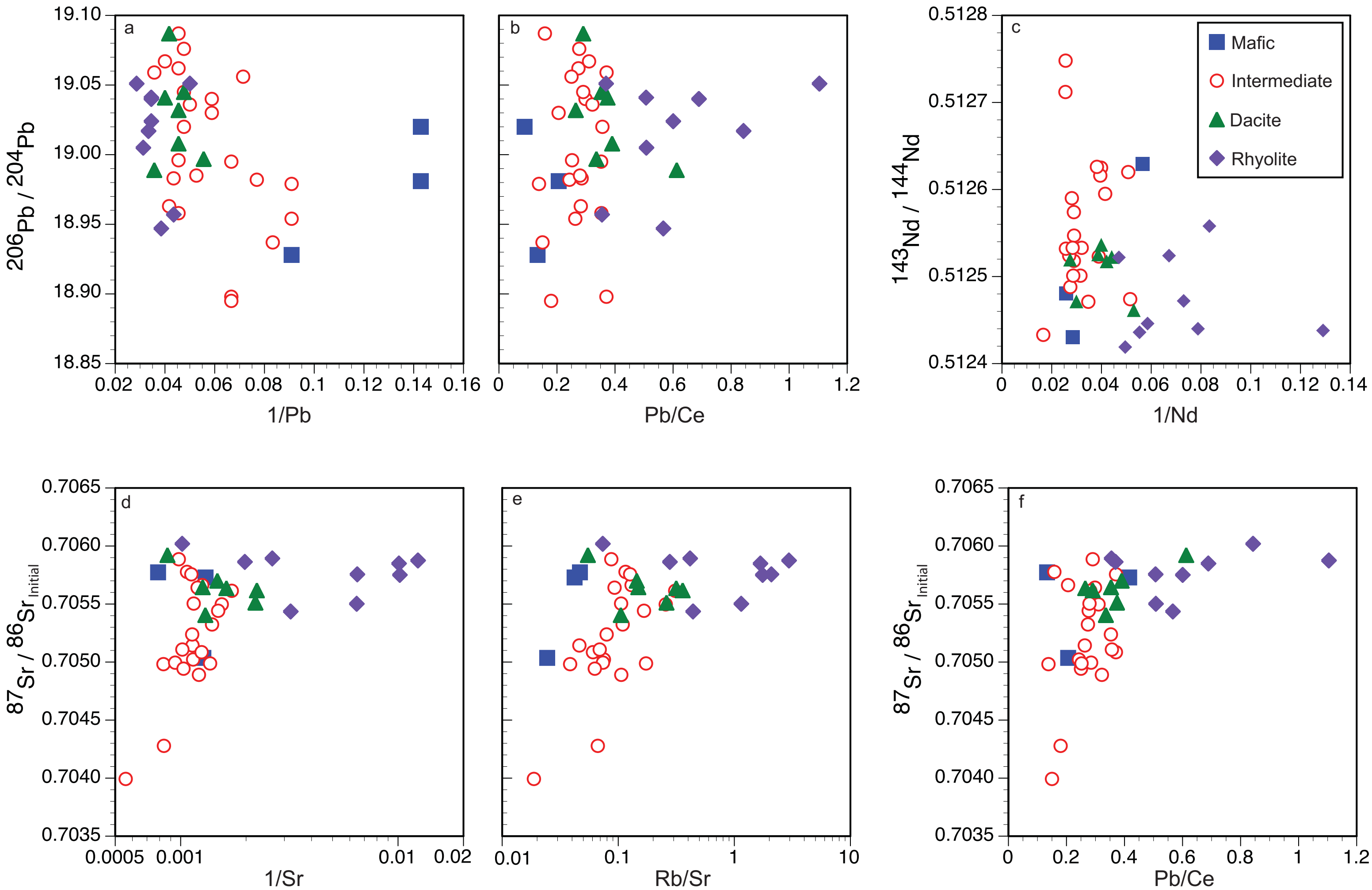

Figure 18 du Bray, John, Cousens, Hayden, and Vikre

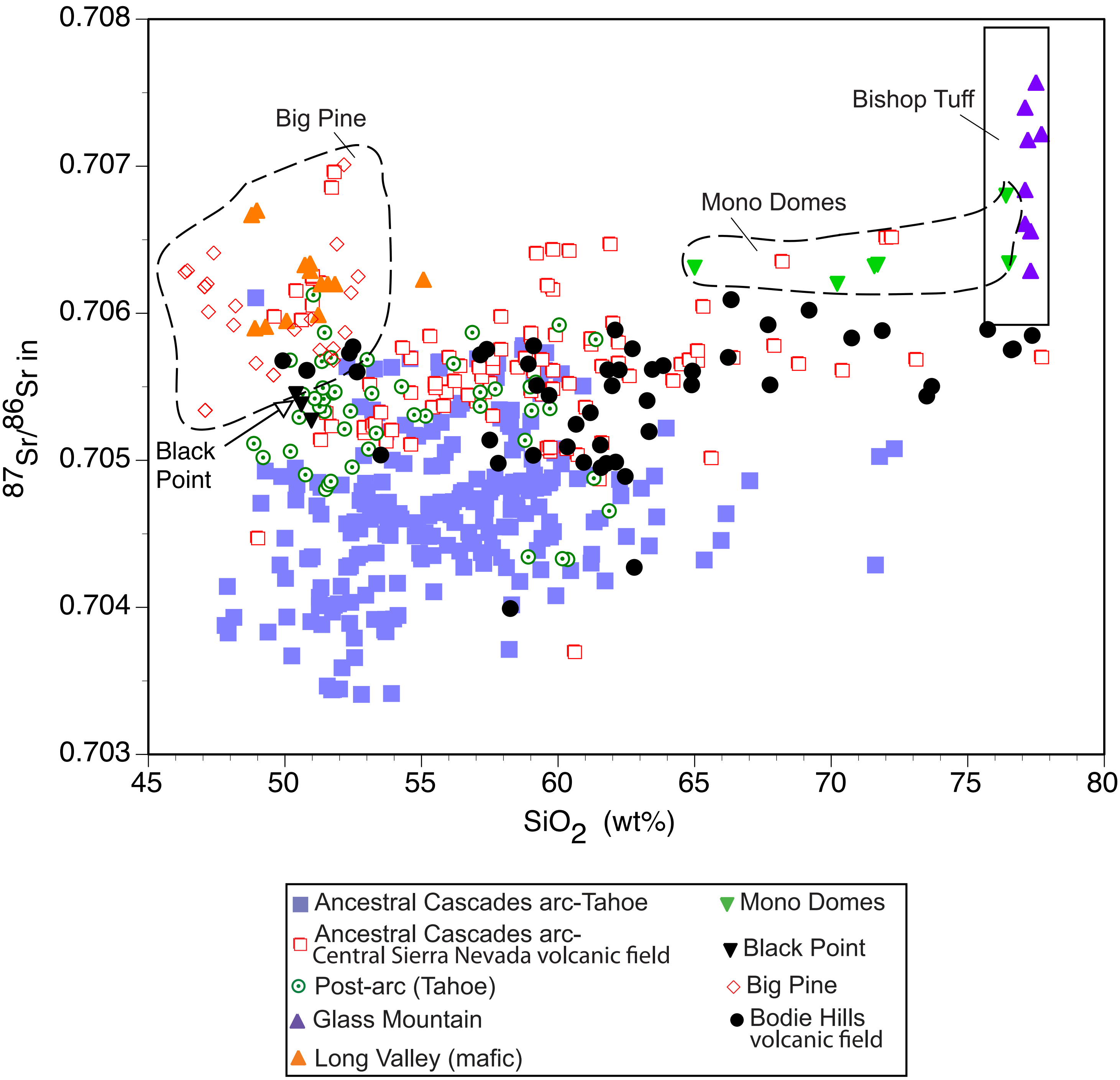

Figure 19 du Bray, John, Cousens, Hayden, and Vikre